Міністерство освіти і науки України
Національний університет «Запорізька політехніка»

НОВІ МАТЕРІАЛИ І ТЕХНОЛОГІЇ В МЕТАЛУРГІЇ ТА МАШИНОБУДУВАННІ

НАУКОВИЙ ЖУРНАЛ

ВИХОДИТЬ ЧОТИРИ РАЗИ НА РІК

№ 1’2026

Заснований у грудні 1997 року

Засновник та видавець – Національний університет «Запорізька політехніка»

Запоріжжя
НУ «Запорізька політехніка»
2026

Ministry of Education and Science of Ukraine
National University Zaporizhzhia Polytechnic

NEW MATERIALS AND TECHNOLOGIES IN METALLURGY AND MECHANICAL ENGINEERING

THE SCIENTIFIC JOURNAL

PUBLISHED FOUR TIMES PER YEAR

No 1’2026

Founded in December 1997

Founder and publisher – National University Zaporizhzhia Polytechnic

Zaporizhzhia
NU Zaporizhzhia Polytechnic
2026

p-ISSN 1607-6885
e-ISSN 2786-7358

УДК 669+621.002+621.002.3

Наказом Міністерства освіти і науки України № 1471 від 26.11.2020 р. «Про затвердження рішень Атестаційної колегії Міністерства щодо діяльності спеціалізованих вчених рад від 26 листопада 2020 року» журнал «Нові матеріали і технології в металургії та машинобудуванні» **(скорочена назва – НМТ)** включений до переліку наукових фахових видань України в катергії «Б»**, в яких можуть публікуватися результати дисертаційних робіт на здобуття наукових ступенів доктора наук і доктора філософії (кандидата наук).**

Інтернет-сторінка журналу: https://nmt.zp.edu.ua

Наукове видання включено до міжнародних (INSPEC, CrossRef) і національних («Джерело», Національна бібліотека України імені В. І. Вернадського НАН України) реферативних та наукометричних баз даних.

Опублікованим статтям присвоюється унікальний ідентифікатор цифрового об'єкта DOI.

Науковий журнал друкує оригінальні та оглядові статті науковців ВНЗ і установ України та інших країн відповідно до рубрик:

- теорія будови та структурних змін у металах, сплавах та композитах. Вплив термічної, хіміко-термічної та термомеханічної обробки на характер структури і фізико-механічні властивості матеріалів;
- конструкційні та функціональні матеріали. Механічні властивості сталей, сплавів та композитів. Технологічне забезпечення надійності та довговічності деталей енергетичних установок. Методи механічного оброблення. Технології зміцнювальних обробок. Характеристики поверхневих шарів та захисних покриттів деталей машин і виробів;
- металургійне виробництво. Теплофізика та теплоенергетика. Ресурсозберігальні технології. Порошкова металургія. Промтранспорт. Раціональне використання металів;
- механізація, автоматизація та роботизація. Вдосконалення методів дослідження та контролю якості металів. Моделювання процесів у металургії та машинобудуванні.

РЕДАКЦІЙНИЙ ШТАТ

Головний редактор :

Сергій Бєліков, доктор технічних наук, професор, Національний університет «Запорізька політехніка», Україна

Заступники головного редактора:

Валерій Наумик, доктор технічних наук, професор, Національний університет «Запорізька політехніка», Україна

Антон Матюхін, кандидат технічних наук, доцент, Національний університет «Запорізька політехніка», Україна

Редакційно-видавнича рада: Сергій Бєліков, Валерій Наумик, Наталія Савчук, Антон Матюхін, Катерина Бондарчук, Наталя Висоцька, Ганна Лещенко

Члени редколегії:

Віктор Грешта, кандидат технічних наук, професор, Національний університет «Запорізька політехніка», Україна
Вадим Шаломєєв, доктор технічних наук, професор, Національний університет «Запорізька політехніка», Україна
Михайло Бриков, доктор технічних наук, професор, Національний університет «Запорізька політехніка», Україна
Валерій Міщенко, доктор технічних наук, професор, Національний університет «Запорізька політехніка», Україна
Олексій Качан, доктор технічних наук, професор, Національний університет «Запорізька політехніка», Україна
Дмитро Павленко, доктор технічних наук, професор, Національний університет «Запорізька політехніка», Україна
Андрій Скребцов, кандидат технічних наук, доцент, Національний університет «Запорізька політехніка», Україна
Олексій Нарівський, доктор технічних наук, доцент, Національний університет «Запорізька політехніка», Україна
Гульміра Яр-Мухамедова, доктор фізико-математичних наук, член-кореспондент НАН Казахстана, Казахський національний університет ім. Аль-Фарабі, Казахстан
Любош Кашчак, доктор філософії, професор, Технічний університет Кошице, Словаччина
Пітер Аррас, доктор філософії, доцент, кампус Де Наїр, Католицький університет Льовена, Бельгія
Анна Ковалек, доктор технічних наук, професор, Ченстоховський політехнічний університет, Польща
Марчін Кнапінський, доктор технічних наук, професор, Ченстоховський політехнічний університет, Польща
Франсіско Хосе Гомес Да Сілва, доктор філософії, доцент, Політехнічний університет Порто, Португалія
Наталія Калініна, доктор технічних наук, професор, Дніпровський національний універсітерт імені Олеся Гончара, Україна
Сергій Гребенюк, доктор технічних наук, професор, Запорізький національний університет, Україна
Діана Глушкова, доктор технічних наук, професор, Харківський національний автомобільно-дорожній університет, Україна
Михайло Турчанін, доктор хімічних наук, професор, Донбаська державна машинобудівна академія, Україна
Юлія Квасницька, д-р техн. наук, старший науковий співробітник, член-кореспондент НАН України, Фізико-технологічногий інститут металів та сплавів НАН України, Україна
Віктор Грищак, доктор хімічних наук, професор, Національний технічний університет «Дніпровська політехніка», Україна
Михайло Ямшинський, доктор технічних наук, професор, Національний технічний університет України «Київський політехнічний інститут імені Ігоря Сікорського», Україна

Рукописи надісланих статей проходять додаткове незалежне рецензування з залученням провідних фахівців України та інших країн, за результатами якого редакційна колегія ухвалює рішення щодо можливості їх опублікування. Рукописи не повертаються.

Рекомендовано до видання Вченою радою Національного університету «Запорізька політехніка»,
протокол № 9 від 27 березня 2026 року.

Журнал набраний та зверстаний у редакційно-видавничому відділі Національного університету «Запорізька політехніка»

Комп'ютерний дизайн та верстання Наталія Савчук

Адреса редакції: 69011, Запоріжжя, вул. Університетська, 64, тел. (061) 769-82-96, редакційно-видавничий відділ

e-mail: rvv@zp.edu.ua

© Національний університет «Запорізька політехніка», 2026

p-ISSN 1607-6885
e-ISSN 2786-7358

UDC 669+621.002+621.002.3

By order of the Ministry of Education and Science of Ukraine No. 1471 of November 26, 2020 "On approval of decisions of the Attestation Board of the Ministry regarding the activities of specialized scientific councils of November 26, 2020", the journal "New materials and technologies in metallurgy and mechanical engineering" (abbreviated name - NMT) is included in the list of scientific professional publications of Ukraine in the category "B", in which the results of dissertations for the scientific degrees of Doctor of Science and Doctor of Philosophy (candidate of science) can be published.

Internet page of the journal: https://nmt.zp.edu.ua

The scientific publication is included in international (INSPEC, CrossRef) and national (Dzherelo, National Library of Ukraine named after V. I. Vernadsky of the National Academy of Sciences of Ukraine) abstract and scientometric databases.

Published articles are assigned a unique DOI digital object identifier.

The scientific journal publishes original articles by scientists from universities and organizations of Ukraine and other countries in accordance with the headings:

- theory of structure and structural changes in metals, alloys and composites. Influence of thermal, chemical-thermal and thermomechanical treatment on the nature of the structure and physical and mechanical properties of materials;
- structural and functional materials. Mechanical properties of steels, alloys and composites. Technological support of reliability and durability of parts of power plants. Methods of mechanical processing. Hardening technologies. Characteristics of surface layers and protective coatings of machine parts and products;
- metallurgical production. Thermal physics and heat power engineering. Resource-saving technologies. Powder metallurgy. Promtransport. Rational use of metals;
- mechanization, automation and robotization. Improvement of methods for research and quality control of metals. Modeling of processes in metallurgy and mechanical engineering.

EDITORIAL TEAM

Editor-in-chief:

Sergiy Byelikov, Doctor of Technical Sciences, Professor, National University Zaporizhzhia Polytechnic, Ukraine

Associate editor-in-chief:

Valeriy Naumyk, Doctor of Technical Sciences, Professor,

Anton Matiukhin, Candidate of Technical Sciences, Associate Professor, National University Zaporizhzhia Polytechnic, Ukraine

Editorial and Publishing Council: Sergiy Byelikov, Valeriy Naumyk, Anton Matiukhin, Nataliia Savchuk, Katerina Bondarchuk, Natalya Vysotska, Ganna Leshchenko

Members of the editorial board:

Viktor Greshta, Candidate of Technical Sciences, Professor, National University Zaporizhzhia Polytechnic, Ukraine
Vadim Shalomeev, Doctor of Technical Sciences, Professor, National University Zaporizhzhia Polytechnic, Ukraine
Mykhaylo Brykov, Doctor of Technical Sciences, Professor, National University Zaporizhzhia Polytechnic, Ukraine
Valeriy Mishchenko, Doctor of Technical Sciences, Professor, National
Oleksiy Kachan, Doctor of Technical Sciences, Professor, National University Zaporizhzhia Polytechnic, Ukraine
Dmytro Pavlenko, Doctor of Technical Sciences, Professor, National University Zaporizhzhia Polytechnic, Ukraine
Andrii Skrebtsov, Candidate of Technical Sciences, Associate Professor, National University Zaporizhzhia Polytechnic, Ukraine
Oleksii Narivs'kyi, Doctor of Technical Sciences, Associate Professor, National University Zaporizhzhia Polytechnic, Ukraine
Gulmira Yar-Mukhamedova, Doctor of Physical and Mathematical Sciences, Member NAS of Kazakhstan (Al-Farabi Kazakh National University), Kazakhstan
Ľuboš Kaščák, PhD, Professor, Technical University of Košice, Slovakia
Peter Arras, PhD, Associate Professor, Campus De Nair, Katholieke Universiteit Leuven, Belgium
Anna Kawalek, Doctor of Technical Sciences, Professor, Politechnika Częstochowska, Częstochowa, Poland
Marcin Knapiński, Doctor of Technical Sciences, Professor, Politechnika Częstochowska, Częstochowa, Poland
Francisco José Gomes Da Silva, PhD, Associate Professor, Technical University of Porto, Portugal
Nataliia Kalinina, Doctor of Technical Sciences, Professor, Oles Honchar Dnipro National University, Ukraine
Sergii Grebenyuk, Doctor of Technical Sciences, Professor, Zaporizhia National University, Ukraine
Diana Hlushkova, Doctor of Technical Sciences, Professor, Kharkiv National Automobile and Highway University, Ukraine
Vitalij Danilchenko, Doctor of Physical and Mathematical Sciences, Institute of Metal Physics named after G. V. Kurdyumov of the National Academy of Sciences of Ukraine, Ukraine
Mykhailo Turchanin, Doctor of Chemistry Sciences, Donbas State Machine-Building Academy, Ukraine
Iuliia Kvasnytska, Doctor of Technical Sciences, Senior Researcher Officer, Corresponding Member of the National Academy of Sciences of Ukraine, Physico-technological Institute of Metals and Alloys of the National Academy of Science of Ukraine, Ukraine
Victor Hryshchak, Doctor of Technical Sciences, Professor, Dnipro University of Technology, Ukraine
Mykhail Yamshinskij, Doctor of Technical Sciences, Professor, National Technical University of Ukraine “Igor Sikorsky Kyiv Polytechnic Instirtute”, Ukraine

Manuscripts of submitted articles undergo additional independent review with the involvement of leading experts from Ukraine and other countries, based on which the editorial board decides on the possibility of their publication. Manuscripts are not returned.

Recommended for publication by the Academic Council of the National University Zaporizhzhia Polytechnic,
Protocol N 9 March 27, 2026.

The journal was typed and typeset in the editorial and publishing department of the National University Zaporizhzhia Polytechnic

Computer design and layout Nataliia Savchuk

Editorial address: 69011, Zaporizhzhia, st. University, 64, tel. (061) 769-82-96, editorial and publishing department e-mail: rvv@zp.edu.ua

© National University Zaporizhzhia Polytechnic, 2026

ЗМІСТ

СТРУКТУРОУТВОРЕННЯ. ОПІР РУЙНУВАННЮ ТА ФІЗИКО-МЕХАНІЧНІ ВЛАСТИВОСТІ

КОНСТРУКЦІЙНІ І ФУНКЦІОНАЛЬНІ МАТЕРІАЛИ

ТЕХНОЛОГІЇ ОТРИМАННЯ ТА ОБРОБКИ КОНСТРУКЦІЙНИХ МАТЕРІАЛІВ

МОДЕЛЮВАННЯ ПРОЦЕСІВ В МЕТАЛУРГІЇ ТА МАШИНОБУДУВАННІ

МЕХАНІЗАЦІЯ, АВТОМАТИЗАЦІЯ ТА РОБОТИЗАЦІЯ

CONTENTS

STRUCTURE FORMATION. RESISTANCE TO DESTRUCTION AND PHYSICAL-MECHANICAL PROPERTIES

STRUCTURAL AND FUNCTIONAL MATERIALS

TECHNOLOGIES OF OBTAINING AND PROCESSING OF CONSTRUCTION MATERIALS

MODELING OF PROCESSES IN METALLURGY AND MECHANICAL ENGINEERING

MECHANIZATION, AUTOMATION AND ROBOTICS

СТРУКТУРОУТВОРЕННЯ. ОПІР РУЙНУВАННЮ ТА ФІЗИКО-МЕХАНІЧНІ ВЛАСТИВОСТІ

STRUCTURE FORMATION. RESISTANCE TO DESTRUCTION AND PHYSICAL-MECHANICAL PROPERTIES

UDC 537.621.4:620.17:53.082.7

Gennadii Snizhnoi	Doctor of Technical Sciences, Professor, Professor of the Department of Information Security and Nanoelectronics, National University Zaporizhzhia Polytechnic, Zaporizhzhia, Ukraine, *e-mail: snow@zp.edu.ua*, ORCID: 0000-0003-1452-0544
Volodymyr Sazhnev	Candidate of Technical Sciences, Associate Professor of the Department of Machines and Foundry Technology, National University Zaporizhzhia Polytechnic, Zaporizhzhia, Ukraine, *e-mail: sajhnev@zp.edu.ua*, ORCID: 0000-0002-2095-4958
Leonid Cherepyns’ky	Candidate of Technical Sciences, Senior Research of the Department of Machines and Foundry Technology, National University Zaporizhzhia Polytechnic, Zaporizhzhia, Ukraine, *e-mail: leonid.cherepinskiy@gmail.com*, ORCID: 0009-0004-3642-0573
Kristina Snizhna	Student of the Faculty of Construction, Architecture and Design, National University Zaporizhzhia Polytechnic, Zaporizhzhia, Ukraine, *e-mail: snowshade66@gmail.com*, ORCID: 0009-0005-1230-0283

SELECTION OF MODIFIERS FOR HIGH-MANGANESE STEEL DEPENDING ON THE OPERATING CONDITIONS OF MINING AND PROCESSING EQUIPMENT COMPONENTS

Purpose. *To establish the optimal modifier for increasing the strength and ductility properties of high-manganese Hadfield steel, as well as wear resistance during dry and wet grinding in an alkaline environment.*

Research methods. *Impact and abrasive wear resistance tests during wet and dry grinding were carried out in a ball mill. Tensile tests were carried out on a URM-50 machine. Determination of the impact strength of samples with a U-shaped notch was carried out on a pendulum impactor MK-30A according to DSTU ISO 148-1:2022. Brinell hardness was determined according to DSTU ISO 6506-1:2007.*

Results. *Based on the results of experimental studies, it was found that the optimal way to increase the physical and mechanical properties and wear resistance of high-manganese steel during dry grinding is a complex modification with titanium and vanadium with preliminary deoxidation with aluminum. The optimal technological factor that increases the wear resistance of high-manganese steel parts during wet grinding in an alkaline environment is the modification of the melt with 0.05 ... 0.15% Nb with preliminary deoxidation with aluminum.*

Scientific novelty. *In steel modified with aluminum, film nitrides of aluminum were found, around which, apparently, corrosion destruction occurs. When modifying Nb within 0.06–0.12 %, film nitrides are practically absent. The bulk of the inclusions were complex nitrides of aluminum and niobium, as well as carbonitrides of niobium. The effect of niobium on wear resistance is positive and during wet grinding has a pronounced extreme character with an optimum at a content of 0.12% Nb.*

Practical value. *An optimal method for improving the physical and mechanical properties and wear resistance of high-manganese steel during dry grinding has been identified: complex modification with titanium and vanadium followed by aluminum deoxidation. The optimal process factor for increasing the wear resistance of high-manganese steel components during wet grinding in an alkaline environment is niobium modification of the melt. The proposed recommendations will reduce the material intensity of mining and processing equipment, improve production, and increase the reliability and durability of high-manganese steel components.*

Key words: *Hadfield steel, modification, boron, niobium, impact toughness, wear resistance, alkaline environment.*

DOI 10.15588/1607-3274-2026-1-1

Introduction

The main range of castings made of wear-resistant high-manganese steel at mining and processing enterprises consists of quickly wearing replaceable parts for crushing and grinding equipment (Fig. 1) and excavators (Fig. 2). The working parts of this equipment include crushing plates, cones, bowls, hammers, sidewalls of the crusher working zones, the main structural elements of the mill drums, which form the grinding chamber surfaces, front walls, bucket teeth, rocker arms, bottom hinges, and links. These components come into contact with the material being ground or the pulp during operation. To ensure structural strength and reliability, they are entirely manufactured or lined with Hadfield steel (110G13L).

During operation, the above-mentioned parts are subjected to tensile, compressive, bending, shear loads, and are subjected to abrasive wear. It is possible to combine two or more types of destructive action on the same part.

The armor of jaw and cone crushers during operation is subjected to very high loads and wears out to a considerable depth, and in some places even the entire thickness of the part. The presence in the castings of even minor casting defects, unsatisfactory structure or low values of the mechanical properties of the steel under such loads leads to premature failure of the armor due to cracks (Fig. 3).

Mill liners operating under very low impact loads are primarily subject to abrasive wear (Fig. 4*a*).

The front wall and teeth of an excavator bucket are subject to abrasive wear under significant impact loads. Due to the rigid shape of these components, they are highly susceptible to work hardening and therefore resist impacts well. The abrasive wear of the front wall and teeth of an excavator bucket is similar (Fig. 4*b*).


a *b*

Figure 1. Details of crushing and grinding equipment made of 110G13L steel:
a – cone crusher armor; *b* – ball mill lining


a *b*

Figure 2. Excavator parts made of 110G13L steel:
a – front wall of the excavator bucket; *b* – excavator bucket tooth


a *b*

Figure 3. Parts of a cone crusher made of 110G13L steel that have failed:
a – worn out armor of the cone crusher; *b* – crack in the armor of the cone crusher

DOI 10.15588/1607-3274-2026-1-1

Figure 4. Worn parts of a ball mill and an excavator made of 110G13L steel:
a – worn lining of the ball mill drum; *b* – worn front wall of an excavator bucket with teeth

Thus, abrasive wear of replaceable parts in mining and processing equipment is the predominant factor causing failure during operation. However, abrasive wear occurs under various operating conditions, including both parts operating without significant impacts and pressures, and parts subject to strong impacts and high pressures. Abrasive wear without impacts and pressures requires high-hardness steel, while impact wear requires high-impact steel.

Analysis of research and publications

To ensure a reduction in the material consumption of mining and processing equipment, improve production, increase its reliability and durability, researchers are constantly proposing various technological measures to increase the stability of mining and processing equipment parts. Improving the operational properties of high-manganese steel is achieved by optimizing the chemical composition of steels for specific groups of castings, heat treatment, modification [1–4].

A significant part of the research aimed at reducing the wear of high-manganese steels is associated with changing the dispersion of the crystallizing phases by introducing small additives of individual elements, compounds into the liquid steel, i.e. modification. The most widespread modifiers are titanium, vanadium, cerium, calcium, zirconium, niobium, tantalum, hafnium, boron [5–7].

At the same time, the effect of modification on the operational stability of high-manganese steels operating in the conditions of mining and dry grinding of ores and minerals has been studied quite fully. But in the preparatory processes for ore enrichment, for example, when grinding in ball mills, wet grinding is used. The mechanisms of wear, and accordingly the wear resistance, are different in wet and dry grinding due to the influence of the corrosive environment and differ significantly [8].

The presence of dissolved and gaseous oxygen, chlorides, sulfides, carbonates and other substances in the pulp that can enter into chemical reactions with the exposed metal surface of the mill linings significantly accelerates its destruction compared to dry grinding. And in the practice of manufacturing castings of linings, grates, “lifters”, wedges, etc., which are operated in wet grinding conditions in alkaline environments with pH 9...12, this is not given importance.

Thus, traditional technological measures aimed at increasing resistance, in wet grinding in some cases do not lead to the expected result.

The purpose of the work

The aim of this investigation is to identify optimal modifiers for high-manganese steel to improve its physical and mechanical properties and wear resistance. It also aims to develop recommendations for selecting Hadfield steel modifiers based on the operating conditions of mining and processing equipment components (pressure, alkaline environment).

Research material and methodology

Impact and abrasive wear resistance tests during wet and dry grinding were carried out in a semi-industrial ball mill. ∅ 680×700 mm at n = 34 rpm for 100 h for each type of grinding. Cast metal samples (9×9×25 mm) were used for the tests. Tensile tests were carried out on a URM-50 machine. To determine the impact strength, samples with a U-shaped notch were tested on a pendulum impactor MK-30A according to DSTU ISO 148-1:2022. Brinell hardness was determined according to DSTU ISO 6506-1:2007. Relative wear resistance was determined as the ratio of the sample's mass loss to the standard's mass loss. The standard was Hadfield steel (1.1C-13Mn), deoxidized with 0.04 wt.% aluminum and containing no other modifiers. In dry grinding, 50 kg of nepheline ore and 14 balls ∅ 100 mm were loaded into the mill. The ore was replaced every 10 hours. In wet grinding, the test was carried out similarly. An aqueous solution of sodium and potassium carbonates (pH 12) was used as a corrosive medium. The pulp was replaced every 10 hours.

Impact research of the influence of traditional modifiers: calcium, rare earth metals (REM), titanium, vanadium were performed at their optimal concentrations, confirmed by many studies [9, 10]. Studies of the influence of boron and niobium, which are used to modify high-manganese steels less often, and data on optimal additives and their influence on the complex of properties are contradictory, were carried out at several different concentrations of modifiers. For the tests, Hadfield steel (1.1C-13Mn or 110G13L) was melted in an induction crucible furnace IST-0.16 with a main lining using the

DOI 10.15588/1607-3274-2026-1-1

method of portioned metal selection, which eliminates the influence of extraneous factors [11]. The content of the modifier elements in the corresponding portions of steel is given in Table 1.

Table 1 – Content of modifying elements in Hadfield steel (1.1C-13Mn), wt.%.

№ melting	Al	Ti	Ca	REM	V	B	Nb
1	0.04	–	–	–	–	–	–
2	0.04	0.2	–	–	–	–	–
3	0.04	–	0.1	–	–	–	–
4	0.04	–	–	0.15	–	–	–
5	0.04	–	–	–	0.2	–	–
6	0.04	0.2	–	–	0.2	-	–
7	0.04	–	–	–	–	0.001	–
8	0.04	–	–	–	–	0.006	–
9	0.04	–	–	–	–	0.012	–
10	0.04	–	–	–	–	–	0.06
11	0.04	–	–	–	–	–	0.12
12	0.04	–	–	–	–	–	0.18
13	0.04	–	–	–	–	–	0.24

Research results

The results of tests of the influence of traditional modifiers (No. 1–6, Table 1) on the mechanical properties and relative wear resistance during wet and dry grinding of Hadfield steel are shown in Fig. 5, 6. The change in strength and plastic properties occurs in the following sequence of modifying elements: increase tensile strength $\sigma_в$: Al→ Al+REM→ Al+V→ Al+Ti→ Al+Ca→ Al+Ti+V (Fig. 5 a), increase relative elongation δ: Al+REM→ Al→ Al+Ti→ Al+V→ Al+Ti+V→ Al+Ca (Fig. 5*b*), increase relative narrowing ψ: Al→ Al+REM→ Al+Ti→ Al+V→ Al+Ca→ Al+Ti+V (Fig. 5 c), increase impact toughness KCU: Al+REM→ Al→ Al+Ca→ Al+V→ Al+Ti→ Al+Ti+V (Fig. 5*d*). It should be noted that the modification of Hadfield steel with Al+Ti+V and Al+Ca complexes causes the highest values of relative elongation (δ) 34.1% and 34.9%, respectively. Thus, the optimal modifier is the Al+Ti+V complex, which leads to the best result in increasing the plastic properties of Hadfield steel.

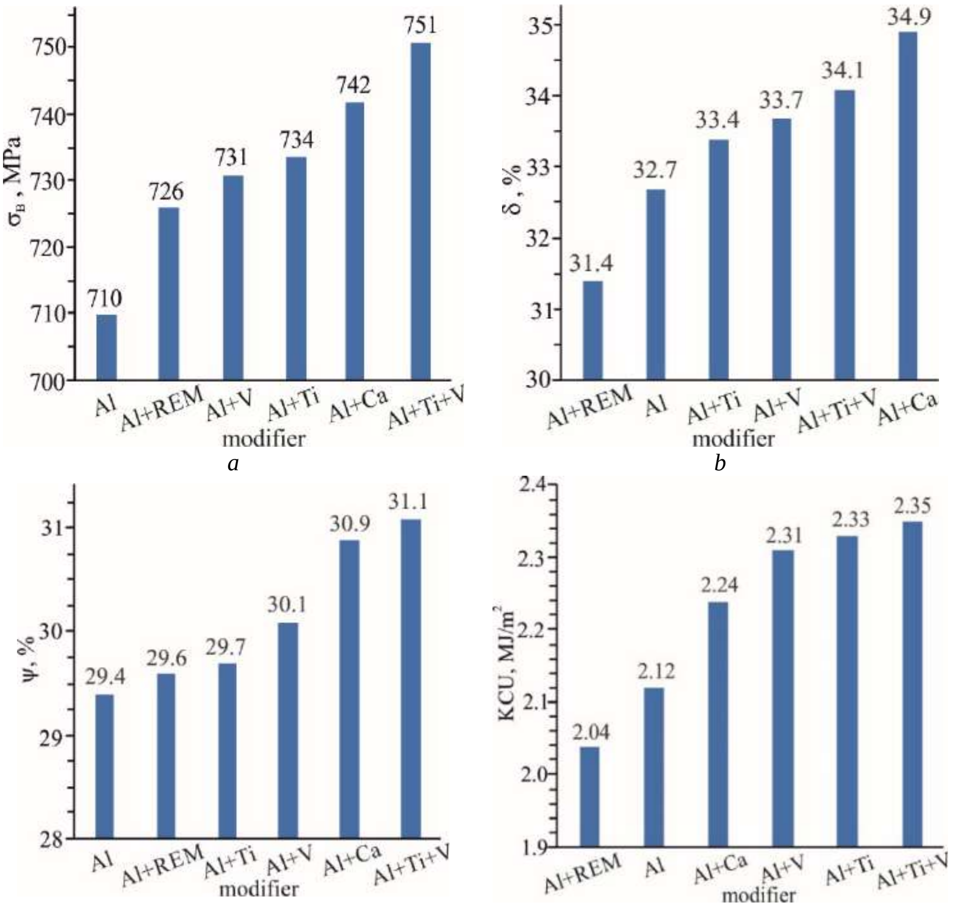

a *b*

c *d*

Figure 5. Strength and plastic properties of Hadfield steel (1.1C-13Mn) depending on the content of traditional modifiers: *a* – tensile strength $\sigma_в$; *b* – relative elongation δ; *c* – relative narrowing ψ; *d* – impact toughness KCU

DOI 10.15588/1607-3274-2026-1-1

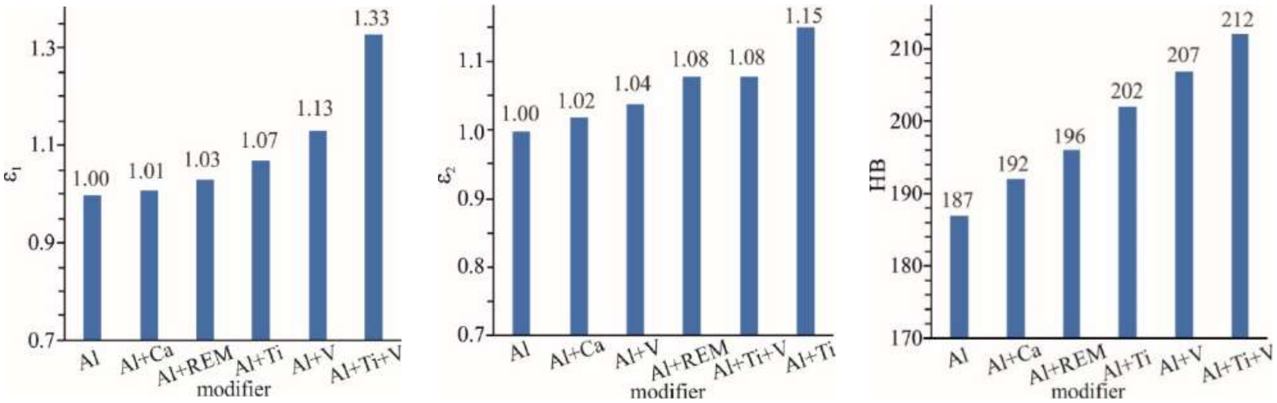

a *b* *c*

Figure 6. Wear resistance and hardness of Hadfield steel (1.1C-13Mn) depending on the content of traditional modifiers:
a – wear resistance of dry grinding ε_1; *b* – wear resistance of wet grinding ε_2; *c* – hardness HB

The increase in wear resistance and hardness occurs in the following sequence of modifying elements: dry grinding wear resistance ε_1 : Al → Al+Ca → Al+REM→ Al+Ti → Al+V → Al+Ti+V (Fig. 6 a), increase wet grinding wear resistance ε_2: Al→ Al+Ca → Al+V →Al+REM→ Al+Ti+V → Al+Ti (Fig. 6*b*), increase HB hardness: Al→ Al+Ca → Al+REM → Al+Ti→ Al+V → Al+Ti+V (Fig. 6 c). It should be noted that the modification of Hadfield steel with the Al+Ti+V complex causes the highest values of dry grinding wear resistance $\varepsilon_1 = 1.33$, and the modification of Al+Ti – the highest values of wet grinding wear resistance $\varepsilon_2 = 1.15$. Thus, depending on the operating conditions of the equipment (dry or wet grinding), it is recommended to melt parts from Hadfield steel, which contains the Al+Ti+V or Al+Ti complex.

The test results showed that the most effective increase in mechanical properties and impact-abrasive wear resistance during dry grinding was provided by titanium and compatible titanium and vanadium additives. A significant increase in mechanical properties was also obtained when modified with calcium. REM additives led to a decrease in mechanical properties, except for the tensile strength. In order to identify the role of each element, metallographic studies of samples of Hadfield steels containing various modifiers were performed (Fig. 7).

Metallographic studies of steels modified with titanium, calcium, REM and vanadium showed that the nature and form of non-metallic inclusions are directly related to the content of the modifying element. In steel deoxidized with aluminum, globular inclusions of aluminomanganese silicates were found (Fig. 7*b*). Additions of calcium and REM led to the grinding and reduction of the total number of globular inclusions (Fig. 7*c*, *d*). Modification with titanium and vanadium led to the formation of nitrides and carbonitrides (Fig. 7*e*, *f*).

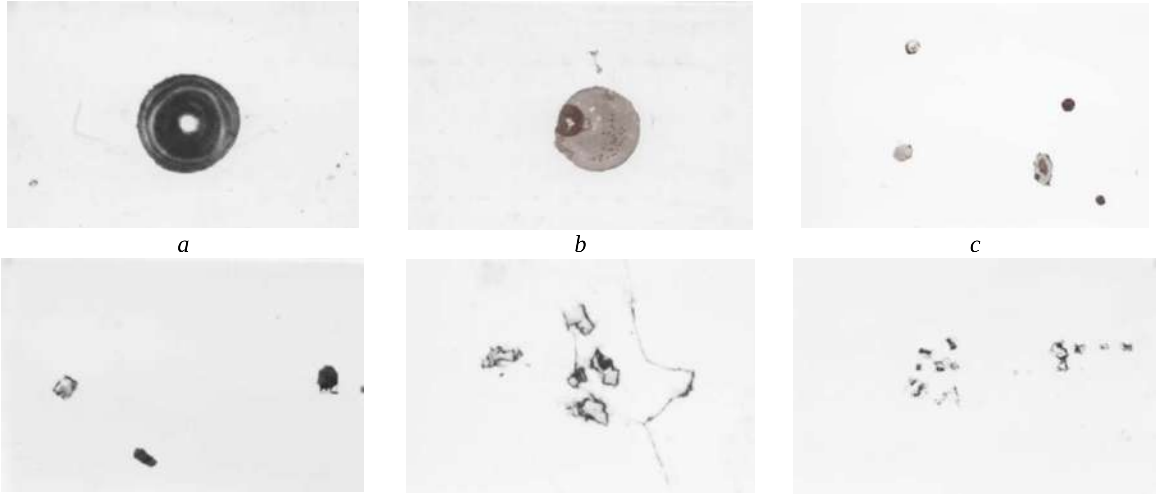

a *b* *c*

d *e* *f*

Figure 7. Non-metallic inclusions in modified steel 110G13L (× 575):
a – manganese silicate; *b* – aluminomanganese silicate in steel deoxidized with aluminum; *c* – complex oxysulfide in steel modified with silicate calcium; *d* – complex oxides in steel with rare earth elements; *e* – titanium nitrides; *f* – vanadium carbonitrides

DOI 10.15588/1607-3274-2026-1-1

Microfractographic studies have established that the properties of high-manganese steel are most influenced by finely dispersed nitride inclusions. In fractures of steel deoxidized with aluminum, film-like aluminum nitrides were found, around which a brittle fracture zone developed (Fig. 8*a*). In steel modified with titanium, the bulk of nitride inclusions consisted of titanium nitrides of regular cubic shape (Fig. 8*b*). When modified with vanadium, vanadium nitrides were found in the steel (Fig. 8*c*). When combined with titanium and vanadium modification, complex inclusions were obtained, which were identified as aluminum, titanium, and vanadium nitrides (Fig. 8*d*).

During wet grinding in an alkaline environment, the impact-abrasive wear resistance decreased sharply compared to dry grinding. The decrease in wear resistance during modification with calcium, REM and vanadium can be explained by the supersaturation of grain boundaries with harmful phases and chemical compounds that initiate corrosion destruction.

The results of tests of the influence of increasing boron and niobium additives on the mechanical properties and relative wear resistance during wet and dry grinding of Hadfield steel (1.1C-13Mn) are shown in Fig. 9 and 10.

The influence of increasing boron and niobium additives on the physical and mechanical properties of high-manganese steel is the same: the strength characteristics increased (Fig. 9*a*), and the plastic characteristics (Fig. 9*b*, *c*) and impact toughness (Fig. 9*d*) monotonically decreased. However, the effects of boron and niobium on the wear resistance of Hadfield steel are significantly different.

No noticeable effect of increasing boron additions on wear resistance was found (Fig. 10). Some decrease in wear resistance is probably due to the brittle effect of grains of eutectic carboboride structures, which are allocated along grain boundaries and which reduce the operational properties of high-manganese steel.

The effect of niobium on wear resistance is positive and during wet grinding has a pronounced extreme character with an optimum at a content of 0.12 % Nb. Further increase in the niobium content monotonically reduced wear resistance. The obtained results are in good agreement with the obtained data of microfractographic studies.

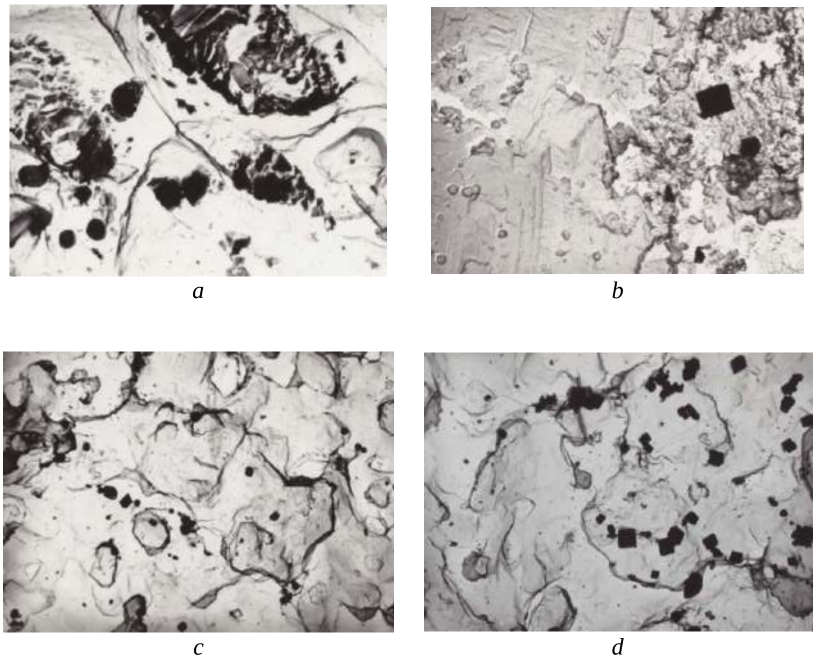
a *b*
c *d*

Figure 8. Nitride inclusions in 110G13L steel (× 10000):
a – film aluminum nitrides; *b* – titanium nitrides; *c* – vanadium nitrides; *d* – aluminum, titanium and vanadium nitrides

DOI 10.15588/1607-3274-2026-1-1

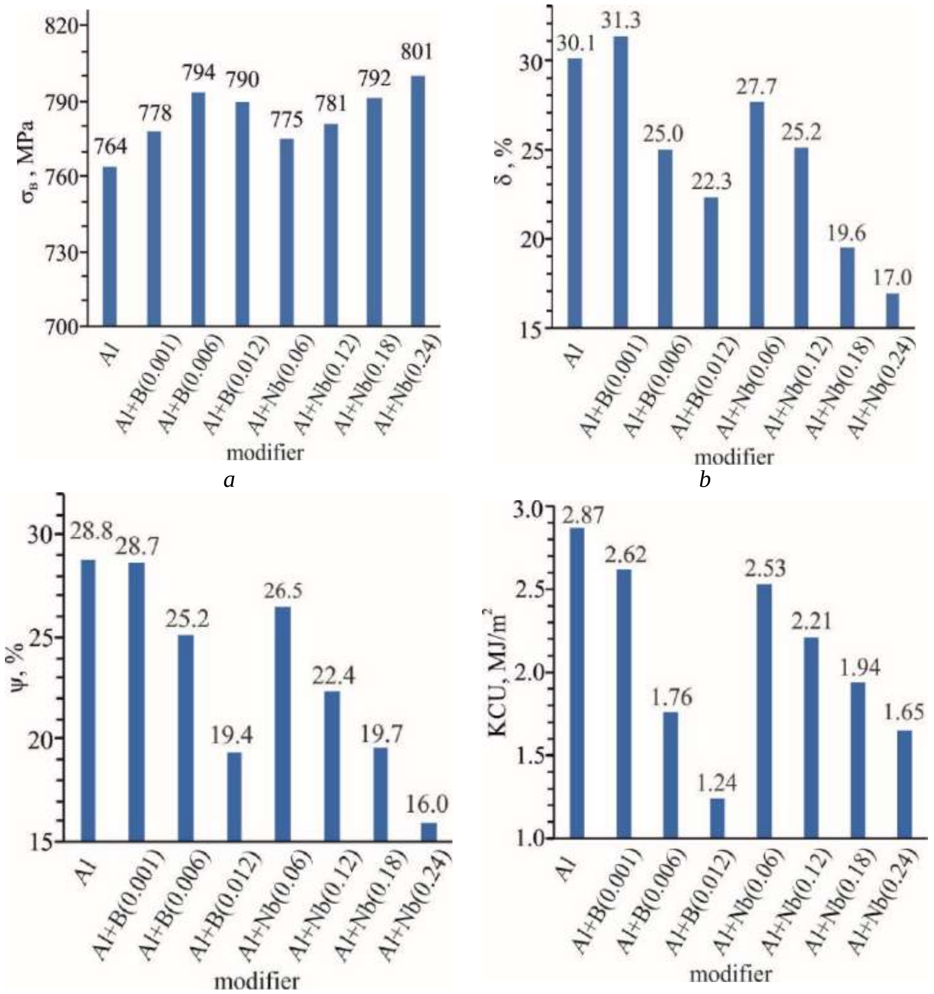

a *b*

c *d*

Figure 9. Plastic properties of Hadfield steel (1.1C-13Mn) depending on the content of increasing boron and niobium additives: a – tensile strength $\sigma_в$; b – relative elongation δ; c – relative narrowing ψ; d – impact toughness KCU

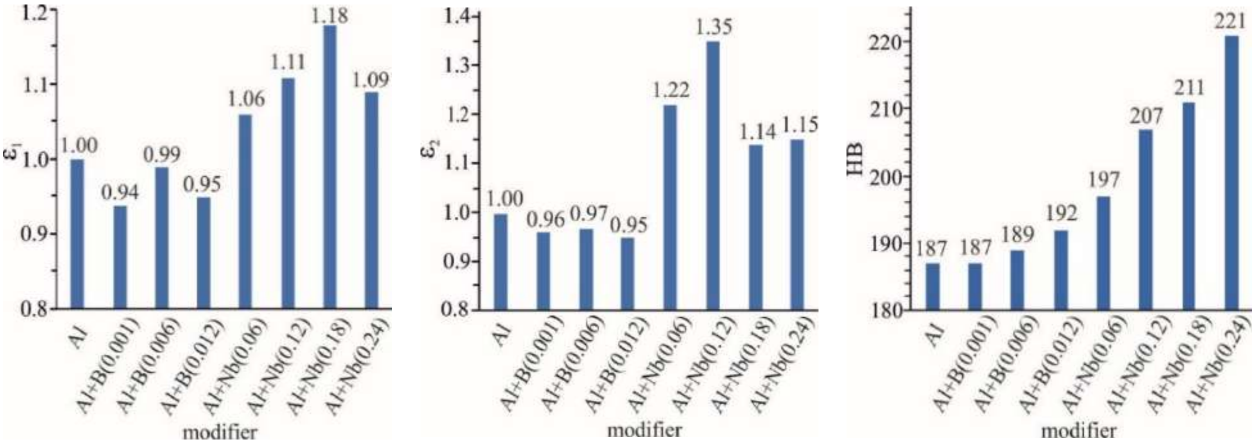

a *b* *c*

Figure 10. Wear resistance and hardness of Hadfield steel depending on the content of increasing boron and niobium additives: *a* – wear resistance of dry grinding ε_1; *b* – wear resistance of wet grinding ε_2; *c* – hardness HB

Discussion

In Hadfield steel modified with aluminum, film aluminum nitrides were found, around which, apparently, corrosion destruction occurs. No significant effect of boron additives on the wear resistance of 110G13L steel was observed. The effect of tempering temperature on the microstructure, mechanical properties, and wear resistance of manganese-boron steel was studied in [11]. When tempered at 150 °C, this steel exhibits the best combination of strength, impact toughness, and wear resistance. Therefore, to achieve significant results from boron modification, additional research on the heat treatment of 110G13L steel is necessary.

When modifying Nb within 0.06-0.12 %, film nitrides are practically absent. The bulk of the inclusions were complex nitrides of aluminum and niobium, as well as niobium carbonitrides. The metal had a homogeneous austenitic finely dispersed structure. Modification with niobium contributes to the conversion of film inclusions into bulk inclusions, which are released in liquid steel and act as modifiers of the second kind. The effect of phosphide eutectic is also weakened. At a niobium content > 0.18 %, the steel is contaminated with coarse complexes of niobium carbonitrides, which are released along grain boundaries and reduce wear resistance in corrosive environments.

Conclusions

1. It has been established that the optimal way to increase the physical and mechanical properties and wear resistance of high-manganese steel during dry grinding is complex modification with titanium and vanadium with preliminary deoxidation with aluminum.
2. It has been established that the optimal technological factor that increases the wear resistance of parts made of high-manganese steel during wet grinding in an alkaline environment is the modification of the melt with 0.05 ... 0.15% Nb with preliminary deoxidation with aluminum.

Reference

1. Ol'shanetskii, V. E., Snezhnoi, G. V., Sazhnev, V. N. (2016). Structural and magnetic stability of austenite in chromium-nickel and manganese steels with cold deformation. Metal science and heat treatment, 58, 5-6, 311-317. https://doi.org/10.1007/s11041-016-0009-5

2. Snizhnoi, H., Sazhnev, V., Snizhnoi, V., Mukhachev, A. (2024). Details of mining beneficiation equipment made of medium manganese wear-resistant steel. IOP Con-ference Series: Earth and Environmental Science, 1348, art. no. 012027. https://doi.org/10.1088/1755-1315/1348/1/012027

3. Sabzi, M., Farzam, M. (2019). Hadfield manganese austenitic steel: a review of manufacturing processes and properties. J. Mater. Res. Express, 6, art. no. 1065C2. https://doi.org/10.1088/2053-1591/ab3ee3

4. Dong, Y., Tao, Z., Sun, C., Wu, H., Gao, X., Du L. (2022). On the continuous cooling transformation of deformed austenite and relationship to properties in medium-Mn steel. J. Mater. Sci., 57, 22042-22052. https://doi.org/10.1007/s10853-022-07859-5

5. Bhattacharya, A., Biswal, S., Barik, R., Mahato, B., Ghosh M., Mitra, R., Chakrabarti, D. (2024). Comparative interplay of C and Mn on austenite stabilization and low temperature impact toughness of low C medium Mn steels. Materials Characterization, 208, art. no. 113658. https://doi.org/10.1016/j.matchar.2024.113658

6. Wang, R., Zhang, W., Zhang, F., Fu, H., Huang, Q., Wu, H., Li, Z., Shan, Q. (2023). The effect of RRA treatment on mechanical properties and wear behavior in vanadium micro-alloyed Hadfield's steel J. Materials Research and Technology, 24, 9884-9896, https://doi.org/10.1016/j.jmrt.2023.05.156

7. Wang, Y., Chen, S., Deng, X., Zhang, X., Luo, Z., Liu T. (2026). Comparative analysis of oxidation mechanisms in V-containing and V-free high-manganese austenitic heat-resistant steels at 1173 K. High Temperature Corrosion of mater., 103, art. no. 5. https://doi.org/10.1007/s11085-025-10361-3

8. Varela, L., Tressia, G., Masoumi, M., Bortoleto, E., Regattieri, C., Sinatora, A. (2021). Roller crushers in iron mining, how does the degradation of Hadfield steel components occur? Engineering Failure Analysis, 122, art. no. 105295. https://doi.org/10.1016/j.engfailanal.2021.105295

9. Sazhnev, V. M., Snizhnoi, H.V. (2023). The influ-ence of technological parameters on the physical, mechan-ical and operational properties of wear-resistant austenitic high-mannan steel. Metallofizika i Noveishie Tekhnologii, 45, 4, 503–522. https://doi.org/10.15407/mfint.45.04.0503

10. Mousavi Anijdan, S.H., Sabzi, M., Najafi, H., Jafari, M., Eivani, A.R., Park, N., Jafarian, H.R. (2021). The influence of aluminum on microstructure, mechanical properties and wear performance of Fe – 14 % Mn – 1.05% C manganese steel. J. of Materials Research and Technology, 15, 4768–4780. https://doi.org/10.1016/j.jmrt.2021.10.054

11. Sazhnev, V.M., Snizhnoi, H.V. (2024). Improving the properties of high-manganese steels by heat treatment methods. Metallofizika i Noveishie Tekhnologii, 46, 11, 1111–1124. https://doi.org/10.15407/mfint.46.11.1111

Received 12.02.2026
Accepted 27.02.2026
Published 31.03.2026

DOI 10.15588/1607-3274-2026-1-1

ВИБІР МОДИФІКАТОРІВ ВИСОКОМАРГАНЦЕВОЇ СТАЛІ В ЗАЛЕЖНОСТІ ВІД УМОВ ЕКСПЛУАТАЦІЇ ДЕТАЛЕЙ ГІРНИЧО-ЗБАГАЧУВАЛЬНОГО ОБЛАДНАННЯ

Геннадій Сніжной	д-р техн. наук, професор, професор кафедри інформаційної безпеки та наноелектроніки, Національний університет «Запорізька політехніка», Запоріжжя, Україна, *e-mail: snow@zp.edu.ua,* ORCID: 0000-0003-1452-0544**;**
Володимир Сажнєв	канд. техн. наук, доцент, доцент кафедри машин та технології ливарного виробництва, Національний університет «Запорізька політехніка», Запоріжжя, Україна, *e-mail: sajhnev@zp.edu.ua,* ORCID: 0000-0002-2095-4958
Леонід Черепинський	канд. техн. наук, старший науковий співробітник кафедри машин та технології ливарного виробництва, Національний університет «Запорізька політехніка», Запоріжжя, Україна, *e-mail: leonid.cherepinskiy@gmail.com,* ORCID: 0009-0004-3642-0573
Крістіна Сніжна	студентка факультету будівництва, архітектури та дизайну, Національний університет «Запорізька політехніка», Запоріжжя, Україна, *e-mail: snowshade66@gmail.com,* ORCID: 0009-0005-1230-0283

Мета роботи. *Встановити оптимальний модифікатор підвищення міцнісних та пластичних властивостей високомарганцевої сталі Гадфільда, а також і зносостійкості при сухому та мокрому помелі в лужному середовищі.*

Методи дослідження. *Випробування на ударно-абразивну зносостійкість при мокрому і сухому помелі проводили в кульовому млині. Випробування на розрив проводили на машині УРМ-50. Визначення ударної в'язкості зразків з U-подібним надрізом проводили на маятниковому копрі МК-30А згідно ДСТУ ISO 148-1:2022. Твердість за Брінеллем визначали згідно ДСТУ ISO 6506-1:2007.*

Отримані результати. *Виходячи з результатів експериментальних досліджень, встановлено, що оптимальним способом підвищення фізико-механічних властивостей і зносостійкості високомарганцевої сталі при сухому подрібненні є комплексне модифікування титаном і ванадієм з попереднім розкисленням алюмінієм. Оптимальним технологічним фактором, який підвищує зносостійкість деталей з високомарганцевої сталі при мокрому помелі в лужному середовищі, є модифікування розплаву 0.05 ... 0.15% Nb з попереднім розкисленням алюмінієм.*

Наукова новизна. *У сталі, модифікованої алюмінієм, виявлено плівкові нітриди алюмінію, навколо яких, очевидно, відбувається корозійна руйнація. При модифікуванні Nb у межах 0.06–0.12% плівкові нітриди практично відсутні. Основну масу включень склали комплексні нітриди алюмінію та ніобію, а також карбонітриди ніобію. Вплив ніобію на зносостійкість позитивно і при мокрому помелі має яскраво виражений екстремальний характер з оптимумом при вмісті 0.12 % Nb.*

Практична цінність. *Визначено оптимальний спосіб підвищення фізико-механічних властивостей та зносостійкості високомарганцевої сталі при сухому подрібненні, а саме комплексна модифікація титаном та ванадієм з попереднім розкисленням алюмінієм.Оптимальним технологічним фактором, що підвищує зносостійкість деталей високомарганцевої сталі при мокрому помелі в лужному середовищі, є модифікація розплаву ніобієм. Запропоновані рекомендації дозволять знизити матеріаломісткість гірничо-збагачувального обладнання, удосконалити виробництво, підвищити надійність та довговічність деталей із високомарганцевої сталі.*

Ключові слова: *сталь Гадфільда, модифікація, бор, ніобій, ударна в'язкість, зносостійкість, лужне середовище.*

Список літератури

1. Ol'shanetskii V. E. Structural and magnetic stability of austenite in chromium-nickel and manganese steels with cold deformation / Ol'shanetskii V. E., Snezhnoi G. V., Sazhnev V. N. // Metal science and heat treat-ment. – 2016. – Vol. 58, 5–6. – P. 311–317. https://doi.org/10.1007/s11041-016-0009-5

2. Snizhnoi H. Details of mining beneficiation equipment made of medium manganese wear-resistant steel / Sazhnev V., Snizhnoi H., Mukhachev V. / IOP Conference Series: Earth and Environmental Science. – 2024. – 1348, art. no. 012027. DOI: https://doi.org/10.1088/1755-1315/1348/1/012027

DOI 10.15588/1607-3274-2026-1-1

3. Sabzi M. Hadfield manganese austenitic steel: a review of manufacturing processes and properties / Sabzi M., Farzam M. // J. Mater. Res. Express. – 2019. – Vol. 6, art. no. 1065C2. https://doi.org/10.1088/2053-1591/ab3ee3

4. On the continuous cooling transformation of deformed austenite and relationship to properties in medium-Mn steel / Dong Y., Tao Z., Sun C. et al. // J. Mater. Sci. – 2022. – Vol. 57. – P. 22042-22052. https://doi.org/10.1007/s10853-022-07859-5

5. Comparative interplay of C and Mn on austenite stabilization and low temperature impact toughness of low C medium Mn steels / Bhattacharya A., Biswal S., Barik R. et al. // Materials Characterization. – 2024. – 208, art. no. 113658. https://doi.org/10.1016/j.matchar.2024.113658

6. The effect of RRA treatment on mechanical properties and wear behavior in vanadium micro-alloyed Hadfield's steel / Wang R., Zhang W., Zhang F. et al. // J. Materials Research and Technology. – 2023. – Vol. 24 – P. 9884-9896, https://doi.org/10.1016/j.jmrt.2023.05.156

7. Comparative analysis of oxidation mechanisms in V-containing and V-free high-manganese austenitic heat-resistant steels at 1173 K / Wang Y., Chen S., Deng X. et al. // High Temperature Corrosion of mater. – 2026. – Vol. 103, art. no. 5. https://doi.org/10.1007/s11085-025-10361-3

8. Roller crushers in iron mining, how does the degradation of Hadfield steel components occur? / Varela L., Tressia G., Masoumi M. et al. // Engineering Failure Analysis. – 2021. – Vol. 122, art. no. 105295. https://doi.org/10.1016/j.engfailanal.2021.105295

9. Сажнєв В. М. Вплив технологічних параметрів на фізико-механічні і експлуатаційні властивості зносостійкої аустенітної високоманганової криці / Сажнєв В. М., Сніжной Г. В. // Металофізика та новітні технології. – 2023. – Т. 45. – № 4. – С. 503–522. https://doi.org/10.15407/mfint.45.04.0503

10. The influence of aluminum on microstructure, mechanical properties and wear performance of Fe – 14 % Mn – 1.05 % C manganese steel / Mousavi Anijdan S. H., Sabzi M., Najafi H. et al. // J. of Materials Research and Technology. – 2021. – Vol. 15. – P. 4768–4780. https://doi.org/10.1016/j.jmrt.2021.10.054

11. Сажнєв В. М. Підвищення властивостей високомарганцевих сталей методами термічної обробки / В. М. Сажнєв, Г. В. Сніжной // Металофізика та новітні технології. – 2024. – Т. 46. – № 11. – С. 1111–1124. https://doi.org/10.15407/mfint.46.11.1111

DOI 10.15588/1607-3274-2026-1-1

p-ISSN 1607-6885 Нові матеріали і технології в металургії та машинобудуванні. 2026/1
e-ISSN 2786-7358 New materials and technologies in metallurgy and mechanical engineering. 2026/1

КОНСТРУКЦІЙНІ І ФУНКЦІОНАЛЬНІ МАТЕРІАЛИ

STRUCTURAL AND FUNCTIONAL MATERIALS

UDC 669.715:669.018.25:620.186

Serhii Puchek — Postgraduate student of the Department of Transport Technologies, National University Zaporizhzhia Polytechnic, Zaporizhzhia, Ukraine, *e-mail: puchek777@gmail.com*, ORCID: 0009-0007-8077-6106

Sergiy Byelikov — Doctor of Technical Sciences, Professor of the Department of Transport Technologies, National University Zaporizhzhia Polytechnic, Zaporizhzhia, Ukraine, *e-mail: belikov@zp.edu.ua*, ORCID: 0000-0002-9510-8190

ASSESSMENT OF THE STRUCTURE AND PROPERTIES OF THE HEAT-RESISTANT NICKEL ALLOY ZHS32-VI AS A MATERIAL FOR THE MANUFACTURING OF GAS TURBINE ENGINE BLADES

Purpose. *To study the macro- and microstructural state of pilot heat-resistant alloy ZhS32-VI casts for the production of critical gas turbine engine components and to evaluate their mechanical properties and heat resistance.*

Research methods. *Structural stability parameters were assessed using the well-known PHACOMP and New PHACOMP calculation methods. Macro- and microstructural analysis and phase composition studies were performed using optical metallography. Mechanical properties at room temperature were determined in accordance with ISO 6892-84 and ST SEV 471-88, while creep-rupture strength tests were conducted in accordance with DSTU ISO 204:2019.*

Results. *The structure and properties of ZhS32-VI alloy specimens produced in a ULMAC FM 1-2-100 vacuum furnace using equiaxed crystallization were studied. The microstructure of the specimens before heat treatment corresponded to the as-cast state of the alloy, and after heat treatment, it met the technical specifications and conformed to the approved microstructure scale. Mechanical properties and heat resistance meet the requirements of technical documentation for critical heat-resistant castings.*

Scientific novelty. *New data on the structure and phase composition of the heat-resistant alloy ZhS32-VI alloy from pilot heats were obtained. Calculation and analytical evaluation method confirmed a high level of structural stability.*

Practical value. *The obtained results provide an opportunity to expand the application of the ZhS32-VI heat-resistant nickel alloy for the production of critical castings.*

Key words: *heat-resistant alloy, macro- and microstructure, mechanical properties, heat resistance, homogenization.*

Introduction

Cast blades are the most critical components of a gas turbine engine, converting the kinetic energy of hot gases into propulsive power for the rotor shaft and power units [1].

Gas turbine engine blades operate under harsh conditions, subject to the simultaneous effects of centrifugal force from their own mass and transverse aerodynamic forces generated by the gas flow in the turbine in an aggressive environment at high temperatures reaching 0.8 T_m [2].

As research results [3] indicate, during operation of rotor blades, there is a constant combined effect of tensile forces, dynamic and static vibration loads. The total (equivalent) loads in the first-stage blades are approximately 120 MPa. Furthermore, the load is also distributed unevenly across the rotor blade profile, with maximum equivalent values at the midsection. A temperature gradient also exists across the blade height and cross-section [4]. These operating conditions determine a set of requirements for materials used in the manufacture of gas turbine blades. High short-term and long-term strength, ductility, fatigue resistance, and structural and properties stability throughout the entire service life are essential. The requirement for the ability to repeatedly restore the structure and properties is economically justified [5].

Achieving the required performance indicators for gas turbine engines is ensured by the use of heat-resistant nickel alloys, or “superalloys” as defined by foreign authors [1, 6–8], for the manufacture of critical gas turbine engine components, primarily nozzle and rotor blades.

For modern gas turbine engines, high-strength nickel alloys are the optimal material for rotor and nozzle blades [2, 9, 10]. An example of such an alloy is the heat-resistant nickel alloy ZhS32-VI [11].

DOI 10.15588/1607-3274-2026-1-2

Material and Methodology

Experimental melts of the heat-resistant nickel alloy ZhS32-VI were conducted at Motor Sich JSC’s industrial production facilities using a modern FM-1-2-100 vacuum melting unit from ULVAC (Japan). Cast alloy blanks were produced by pouring liquid metal into 80mm-diameter metal molds. The initial melts' blanks had an equiaxed grain structure.

To test the alloy for compliance with the mechanical properties and long-term strength requirements of TU 1-92-177, specimens were produced using investment casting in UNVK-8P and UNVK-9A vacuum melting units. The cast specimens had a directional or single-crystal structure. Fresh charge materials (nickel, chromium, molybdenum, tungsten, rhenium, and tantalum) were used in the production of ZhS32-VI heat-resistant alloys using high-temperature melt processing.

The resulting cast samples were heat-treated by homogenization in a protective atmosphere (in a dynamic vacuum) at a temperature of 1270±10 °C, held for 1 hour and 15 minutes, and cooled at a rate equivalent to air cooling.

The chemical composition of the experimental alloys was determined using a spectral analyzer on an ARL-4460 quantometer.

The macrostructure of the samples was revealed by chemical etching in a reagent containing 25 % HNO_3, 25 % HF, and 50 % water. The microstructure was evaluated on microsections before and after etching in Marble reagent (4 g $CuSO_4$, 20 mg HCl, 20 mg water) using a Carl Zeiss optical microscope at magnifications of ×20, ×500, and ×1000.

The short-term and long-term mechanical properties of the samples (tensile strength, high-temperature strength, relative elongation, and narrowing) were determined after heat treatment using the standard mode.

Mechanical properties at room temperature were determined in accordance with ISO 6892-84 and ST SEV 471-88, and long-term strength tests in accordance with DSTU ISO 204:2019 were performed on a DST-500 test rig at a temperature of 1000 °C and a load of 280 MPa until complete failure.

The parameters of structural stability were calculated using the well-known calculation methods PHACOMP [14, 16] and New PHACOMP [17, 18]. Using computer modeling of thermodynamic processes CALPHAD in the JMatPro program [13, 14, 16, 19] the ΔE method was used to evaluate the balance of the chemical composition. In accordance with the calculation and analytical model (CAM) developed at the Zaporizhzhia Polytechnic National University [12, 14, 16, 20, 21], important temperature parameters, the values of the short-term and long-term strength limits at different temperatures and different alloying levels were determined.

Research Results and Discussion

All tested melts of the ZhS32-VI alloy meet the requirements of the technical documentation (Table 1).

The cross-sectional macrostructure of 80 mm diameter test melt blank fragments, produced in a ULVAC FM-1-2-100 vacuum furnace using equiaxed crystallization prior to heat treatment, is shown in Figure 1.

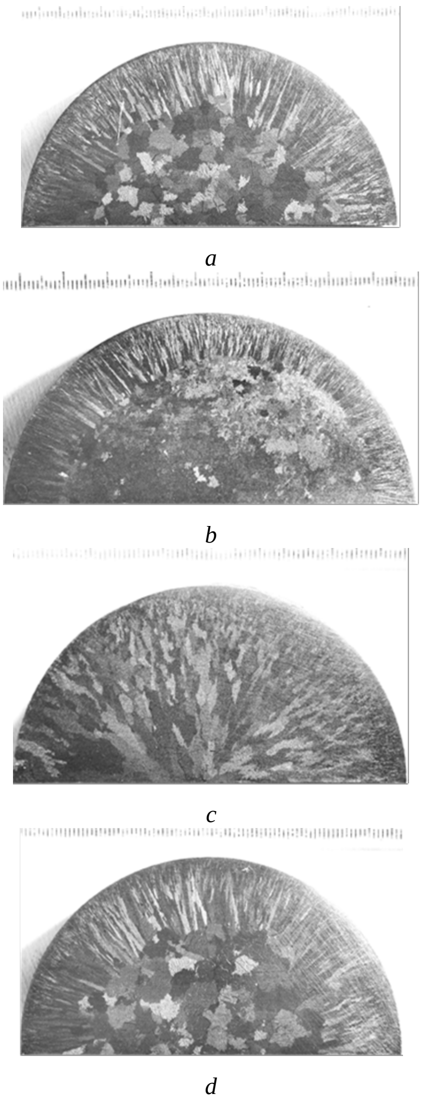

Figure 1. Macrostructure in the cross-section of the middle part of 80 mm diameter rod blanks made of ZhS32-VI alloy, produced on a ULVAC FM-1-2-100 unit before heat treatment:

a – Heat 1, *b* – Heat 2, *c* – Heat 3, *d* – Heat 4

DOI 10.15588/1607-3274-2026-1-2

Table 1 – Chemical composition of the metal of experimental melts of heat-resistant nickel alloy ZhS32-VI

Fuse	Content of elements, % by weight															
	C	Cr	Co	W	Mo	Al	Nb	Ta	Re	Fe	Si	S	P	B	O_2	N_2	Ni
1	0,127	4,90	9,00	8,78	1,13	5,82	1,59	3,96	3,82	0,06	0,12	0,005	0,005	0,020	0,00039	0,00052	base
2	0,143	4,92	9,03	8,65	1,12	5,93	1,69	4,07	3,80	0,06	0,11	0,005	0,005	0,015	0,00045	0,00060	base
3	0,140	5,00	9,26	8,80	1,17	6,03	1,74	4,05	3,93	0,06	0,11	0,005	0,005	0,014	0,00040	0,00060	base
4	0,130	4,64	9,11	8,87	1,17	5,80	1,60	3,83	3,65	0,06	0,02	0,005	0,005	0,015	0,00043	0,00053	base
Norms ТУ 1-92-177-91	0,12-0,17	4,5-5,3	9,0-9,5	8,1-8,9	0,9-1,3	5,7-6,2	1,4-1,8	3,7-4,4	3,6-4,3	≤ 0,5	≤ 0,2	≤ 0,005	≤ 0,010	≤ 0,02	≤ 0,002	≤ 0,002	base

The following crystallization zones are observed in the structure of the blanks:

- zone of fine subcortical crystals;
- zone of columnar crystals;
- zone of equiaxed crystals.

The results of the macrostructure parameter measurements are presented in Table 2.

Table 2 – Macrostructure parameters of 80 mm diameter blanks made of ZhS32-VI alloy

Melt number	Size of crystallization zones, mm			Macrograin size in the equiaxed crystal zone, mm
	Zone of fine subcortical crystals	Columnar crystal zone	Zone of equiaxed crystals	
1	1…2	18…20	40…44	2…6
2	1…2	8…13	54…64	0.75…2
3	1…2	~ 40	-	-
4	1…2	16…18	44…48	2…7

Figure 2 shows the macrostructure of fragments of blanks Ø 80 mm (melts 1–4), obtained in a vacuum furnace FM-1-2-100 from ULVAC using the equiaxed crystallization method after standard heat treatment (homogenization at a temperature of 1270±100 °C – 1 hour 15 minutes).

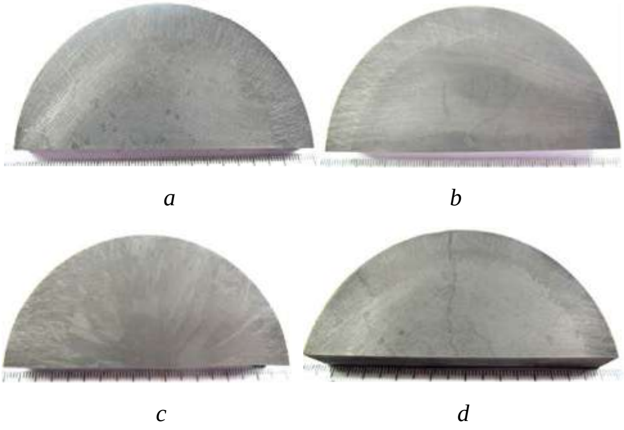

Figure 2. Macrostructure in the cross-section of the middle part of 80 mm diameter rod blanks made of ZhS32-VI alloy, produced on a ULVAC FM-1-2-100 unit after heat treatment:
a – Melt 1, *b* – Melt 2, *c* – Melt 3, *d* – Melt 4

Microstructure of a rod blank before heat treatment

Inspection of unetched microsections cut from the peripheral and central zones of the middle portion of blank fragments from melts 1–4 revealed no metal contamination in the form of coarse slag inclusions or clusters. The size of oxide inclusions does not exceed 0.023 mm (Figure 3).

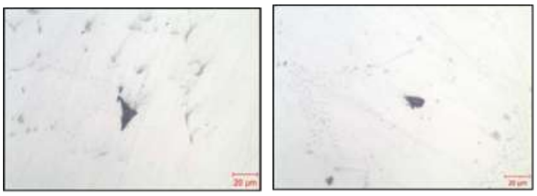

a – edge *b* – center

Melt 1

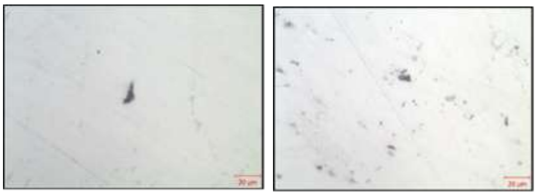

c – edge *d* – center

Melt 2

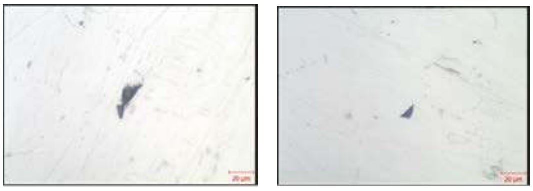

e – edge *f* – center

Melt 3

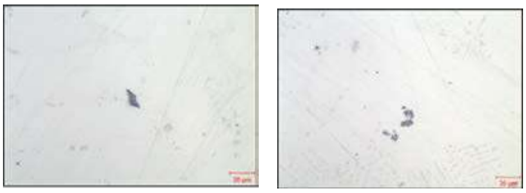

g – edge *h* – center

Melt 4

Figure 3. Oxide inclusions in the material of blanks made of ZhS32-VI alloy, obtained on the FM-1-2-100 installation from ULVAC, ×500

Globular carbides range in size from 1 to 12 μm, while lamellar carbides range from 5 to 27 μm (see Table 3). Shrinkage microporosity is present in the central

DOI 10.15588/1607-3274-2026-1-2

zone of the fragments of the analyzed blanks (the maximum micropore size is ~0.06 mm) (Figure 4, see Table 3).

The blank from heat 1 contains isolated, rare films (Figure 5). No films were detected in the remaining fragments of the received blanks.

Figure 6 shows the carbide distribution in the central zone of the blanks received for analysis.

The microstructure of the studied blanks is identical and, prior to heat treatment, consists of a γ-solid solution with the presence of an intermetallic γ´ phase, a eutectic (γ-γ´) phase, carbides, and carbonitrides (Fig. 7–10).

The parameters of the structural components in the blanks of melts 1–4 made of the ZhS32-VI alloy (before heat treatment) are presented in Table 3.

Furthermore, it should be noted that skeletal precipitates of carboboride eutectic, located near particles of the eutectic (γ-γ´) phase (Figure 11), were detected in the structure of all the studied melts.

Table 3 – Parameters of structural components in a blank ∅ 80 mm made of ZhS32-VI alloy before heat treatment

Melt number	Place of measurement	Dimensions of structural components, μm				
		carbides		eutectic type(γ-γ´)	Micro-pores	Distance between the axes of 2nd order dendrites
		globular type MC	plate type M_6C			
1	edge	2…7	5…12	5…15	up to 20	15…25
	center	2…7	5…27	5…60	up to 45	35…50
2	edge	2…12	5…25	5…15	up to 20	12…25
	center	2…12	5…27	5…50	up to 60	30…50
3	edge	2…10	5…10	5…27	up to 10	10…25
	center	2…12	5…20	5…50	up to 10	30…50
4	edge	1…5	5…10	5…15	up to 15	12…25
	center	1…8	5…17	5…50	up to 25	30…50

a – melt 1, × 200 *b* – melt 2, × 200

c – melt 3, × 200 *d* – melt 4, × 200

Figure 4. Microporosity in the material of blanks made of the alloy ZhS32-VI, obtained on the FM-1-2-100 installation of the company “ULVAC”

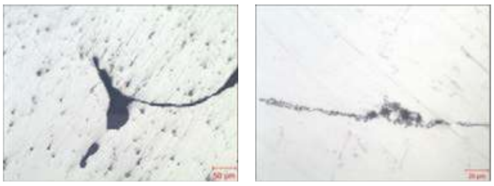

a – edge, ×200 melt 1 *b* – center, ×500

Figure 5. Films in the material of the workpiece made of the alloy ZhS32-VI, obtained on the FM-1-2-100 installation of the company “ULVAC”

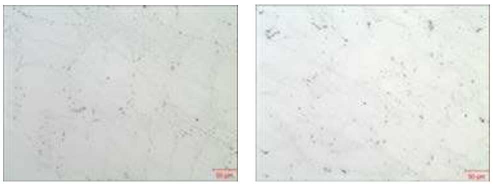

a – melt 1 *b* – melt 2

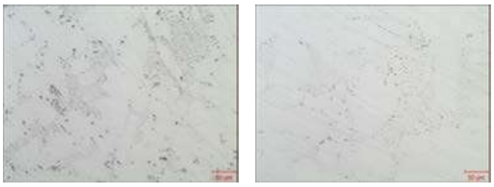

c – melt 3 *d* – melt 4

Figure 6. Distribution of carbides in the material of blanks made of the alloy ZhS32-VI, obtained on the FM-1-2-100 installation from ULVAC, × 200

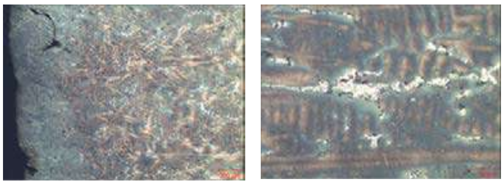

a – ×50 edge *b* – ×200

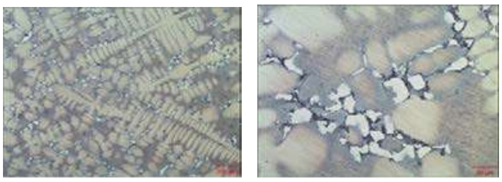

c – ×50 center *d* – ×200

Figure 7. Microstructure of the middle part of the ∅ 80 mm billet made of ZhS32-VI alloy (heat 1) – before heat treatment: *a*, *b* – peripheral zone; *c*, *d* – central zone

To determine the mechanical and heat-resistant properties of ZHS32-VI alloy bar blanks produced from fresh components in a ULVAC FM-1-2-100 vacuum furnace, samples (∅15 mm; L = 135 mm) were cast using high-speed directional solidification (HSDS).

The microstructure of the HSDS samples before heat treatment is identical and consists of a γ-solid solution with the presence of an intermetallic γ´ phase, a eutectic (γ-γ´) phase, carbides, and carbonitrides. Skeletal carboboride

DOI 10.15588/1607-3274-2026-1-2

eutectic precipitates were detected near the eutectic (γ-γ′) phase in the structure of all studied samples (as well as in the material of the studied blanks).

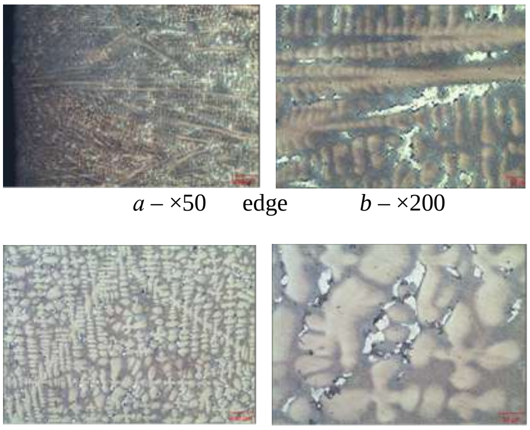

a – ×50 edge *b* – ×200

c – ×50 center *d* – ×200

Figure 8. Microstructure of the middle part of the ∅ 80 mm blank made of the ZhS32-VI alloy (heat 2) – before heat treatment: *a*, *b* – peripheral zone; *c*, *d* – central zone

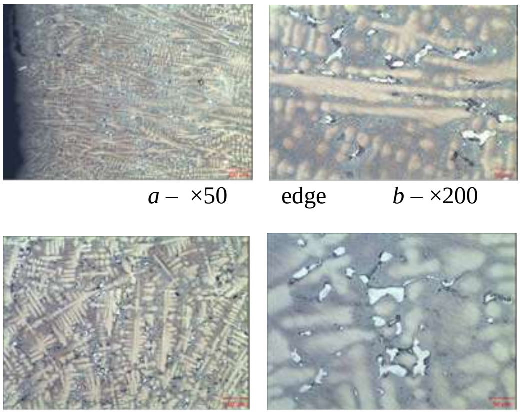

a – ×50 edge *b* – ×200

c – ×50 center *d* – ×200

Figure 9. Microstructure of the middle part of the 80 mm diameter blank made of ZhS32-VI alloy (heat 3) – before heat treatment: *a*, *b* – peripheral zone; *c*, *d* – central zone

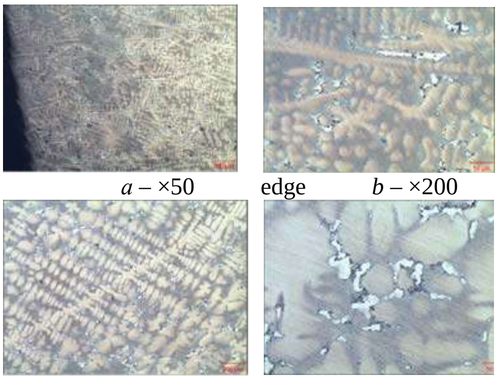

a – ×50 edge *b* – ×200

c – ×50 center *d* – ×200

Figure 10. Microstructure of the middle part of a Ø80 mm billet made of ZhS32-VI alloy (heat 4) – before heat treatment: *a*, *b* – peripheral zone; *c*, *d* – central zone

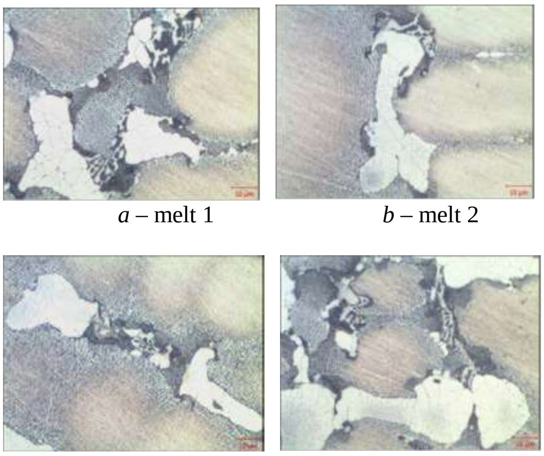

a – melt 1 *b* – melt 2

c – melt 3 *d* – melt 4

Figure 11. Carboboride eutectic in the material of ZhS32-VI alloy blanks produced on a ULVAC FM-1-2-100 unit, × 1000

The microstructure of blanks from heats 1, 2, and 3, heat-treated using the standard mode, revealed structures characteristic of the overheated state of ZhS32-VI alloy (Figure 12*a*, *b*, *c*).

The microstructure of the blank from heat 4 after heat treatment is satisfactory for a normally heat-treated ZhS32-VI alloy and corresponds to the approved microstructure scale; there is no overheating (Figure 12d).

No topologically close-packed phase (TCP) was detected in the studied fragments of the rod blanks (either before or after heat treatment using the standard mode).

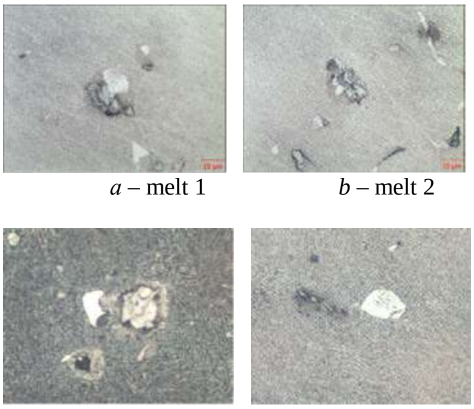

a – melt 1 *b* – melt 2

c – melt 3 *d* – melt 4

Figure 12. Microstructure of ZHS32-VI alloy blanks heat-treated using a standard process, produced in a ULVAC FM-1-2-100 furnace, × 1000

The microstructure of samples cast from melts 1–3, heat-treated using the standard mode, revealed structures characteristic of the overheated state of the ZhS32-VI alloy (Figure 13*a*, *b*, *c*).

The microstructure of samples cast from melt 4, after standard heat treatment, is satisfactory for the normally heat-treated state of the ZhS32-VI alloy and corresponds to the approved microstructure scale; there is no overheating (Figure 13*d*).

The mechanical and heat-resistant properties were determined according to TU1-92-177-91, 18T-TU-158, and 18T-TU-187 on non-heat-treated samples. Additionally, samples heat-treated using the standard regime (homogenization at 1270±10 °C for 1 hour and 15 minutes) were tested.

The results of the mechanical and high temperature strength tests are presented in Table 4. The crystallographic orientation (CGO) on the studied single-crystal samples did not exceed 0.9 angular degrees.

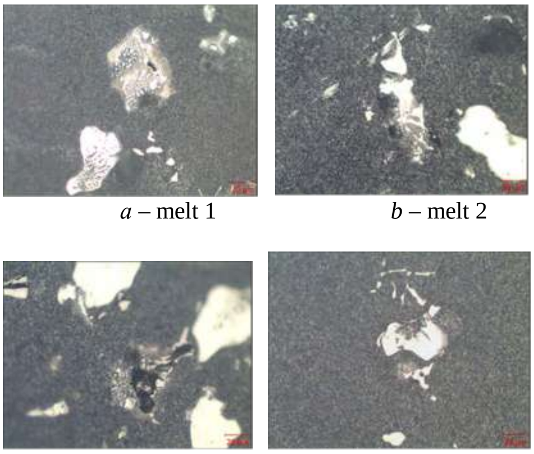
a – melt 1
b – melt 2
c – melt 3
d – melt 4

Figure 13. Microstructure of samples of alloy ZhS32-VI heat-treated in a standard mode, ×500

Table 4 – Mechanical and heat-resistant properties of alloy ZhS32-VI

Condition of the material	Melt	Mechanical properties at t = 20 °C		Time to failure (at Tst. 1000 °C σ= 280MPa),τ_r, hours
		$\sigma_в$, МПа	δ, %	
Without heat treatment	1	1167	8,4	52^{20}
	2	1093	6,4	42^{10}
	3	1089	10,0	65^{30}
	4	1125	10,0	64^{00}
After heat treatment	1	1178	6,8	89^{30}
	2	1155	6,4	88^{30}
	3	1174	11,2	88^{35}
	4	1158	8,0	88^{00}
Standards TU1-92-177-91; 18T-TU-158 and 18T-TU-187		≥ 850,0	≥ 6,0	≥ 40,0

The calculation and analytical assessment of the structural and phase stability of the alloy ZhS32-VI carried out using the integrated CAM method [11, 12, 14, 16, 20, 21] confirmed the high level of structural stability in terms of the alloy's tendency to form TPC (Π_{TPC}≈0.3373…0.3489<Π_{CRIT}=0.5), as well as in terms of the alloying system imbalance parameter (ΔE≈-0.0047…-0.2401<ΔE_{erit}=±0.4), which allows us to consider the alloy ZhS32-VI as sufficiently balanced at the lower level of alloying element content.

The calculated value of short-term strength σ_B at room temperature, determined according to the method [14, 16], yielded a value in the range of 1053.59...1125.08 MPa, which corresponds to the values, obtained on test samples (1089...1167 MPa, Table 4).

Conclusions

A study of the macro- and microstructure of a series of experimental heat-resistant nickel alloy ZhS32-VI melts revealed the satisfactory condition of all samples and their compliance with technical documentation requirements. The microstructure of the studied samples is identical and, prior to heat treatment, consists of a γ-solid solution with the presence of an intermetallic γ´ phase, a eutectic (γ-γ´) phase, carbides, and carbonitrides. Skeletal precipitates of carboboride eutectic located near particles of the eutectic (γ-γ´) phase were detected in the structure of all the melts.

The mechanical and heat-resistant properties of the metal in all melts exceeded the standard values, and the calculation and analytical evaluation method confirmed a high level of structural stability and a sufficient balance in the content of alloying elements, as evidenced by the absence of TPC phases in the structure.

References

1. Sims, C. T., Stoloff, N. S., & Hagel, W. C. (1987). Superalloys II: High-temperature materials for aerospace and industrial power (2nd ed.). John Wiley and Sons.
2. Miller, H. E., & Chambers, W. L. (1987). Constructions of gas turbines and superalloys. In C. T. Sims, N. S. Stoloff, & W. C. Hagel (Eds.), Superalloys II: High-temperature materials for aerospace and industrial power (2nd ed., 27–56). John Wiley and Sons.
3. Haiduk, S. V., & Kononov, V. V. (2017). Forecasting of structural stability parameters for cast heat-resistant nickel alloys. Herald of Aeroenginebuilding, (1), 139–148. https://doi.org/10.15588/1727-0219-2017-1-24
4. Chyhryn, V. S. (2017). Konstruktsiya i prochnost' aviatsionnykh dvigateley [Design and strength of aircraft engines]. KhAI.
5. Velikanova, N. P., Velikanov, P. G., & Kiselev, A. S**.** (2011). Influence of operational operating time on short-term mechanical properties of heat-resistant alloys for turbine parts of aviation gas turbine engines. Herald of Aeroenginebuilding, (2), 239–243.
6. Sims, C. T., & Hagel, W. C. (Eds.). (1972). The Superalloys. John Wiley and Sons.
7. Birosca, S., & Kolisnychenko, S. (Eds.). (2020). Superalloys II. Trans Tech Publications Ltd.
8. Reed, R. C. (2006). The superalloys: Fundamentals and applications. Cambridge University Press.

DOI 10.15588/1607-3274-2026-1-2

9. Bohuslaiev, V. A., Muravchenko, V. F., Zhemanyuk, P. D., et al. (2017). Tekhnologicheskoye obespecheniye ekspluatatsionnykh kharakteristik detaley GTD. Lopatki kompressora i ventilyatora [Technological support of operational characteristics of GTE parts. Compressor and fan blades] (Part 2). Motor Sich.

10. Myalnitsa, H. P., Verkhovliuk, A. M., Narivskyi, A. V., et al. (2023). Materialy i tekhnolohii dlia lopatok vitchyznyanykh promyslovykh hazovykh turbinnykh dvyhuniv [Materials and technologies for blades of domestic industrial gas turbine engines] (V. V. Verotska, Ed.). Naukova Dumka.

11. Andriienko, A. G., Haiduk, S. V., & Kononov, V. V. (2010). Evaluation of the influence of the tantalum to rhenium ratio on the structural stability and mechanical properties of the heat-resistant nickel alloy ZhS-32. Herald of Aeroenginebuilding, (1), 128–132.

12. Haiduk, S. V. (2015). Complex calculation and analytical methodology for the design of cast heat-resistant nickel alloys. New Materials and Technologies in Metallurgy and Mechanical Engineering, (2), 92–103.

13. Saunders, N., Fahrmann, M., & Small, C. J. (2000). The application of CALPHAD calculations to Ni-based superalloys. In K. A. Green, T. M. Pollock, & R. D. Kissinger (Eds.), Superalloys 2000, 803–811, TMS.

14. Haiduk, S. V., & Bielikov, S. B. (2017). Naukovi osnovy proektuvannya lyvarnykh zharomitsnykh nikelʹovykh splaviv z neobkhidnym kompleksom sluzhbovykh vlastyvostey [Scientific foundations of designing cast heat-resistant nickel alloys with the required complex of service properties]. ZNTU.

15. Haiduk, S. V., & Kononov, V. V. (2016). Calculation of the phase composition of a cast weldable heat-resistant corrosion-resistant nickel alloy using the CALPHAD method. Herald of Aeroenginebuilding, (1), 107–112.

16. Haiduk, S. V. (2018). Rozvytok i zastosuvannya naukovykh pryntsypiv lehuvalnya dlya rozrobky zharomitsnykh nikelʹovykh splaviv z harantovanymy vlastyvostyamy [Development and application of scientific principles of alloying for the development of heat-resistant nickel alloys with guaranteed properties] (Doctoral dissertation). ZNTU, Zaporizhzhia.

17. Morinaga, M., Yukawa, N., Adachi, H., & Ezaki, H. (1984). New PHACOMP and its applications to alloy design. In M. Gell et al. (Eds.), Superalloys 1984, 523–532, AIME.

18. Yukawa, N., Morinaga, M., Ezaki, H., & Murata, Y**.** (1986). Alloy design of superalloys by the d-electrons concept. In High temperature alloys for gas turbines and other applications: Proceedings of Conference, Liege, 935–944, CRM.

19. Haiduk, S. V., & Kononov, V. V. (2014). Evaluation of the influence of tantalum on critical temperatures in a cast weldable heat-resistant nickel alloy using calculation and experimental methods. New Materials and Technologies in Metallurgy and Mechanical Engineering, (2), 34–40.

20. Haiduk, S. V., Kononov, V. V., & Kurenkova, V. V. (2017). Application of a complex calculation-analytical technique for multi-criteria optimization of the compositions of cast heat-resistant nickel alloys. Modern Electrometallurgy, (1), 44–51.

21. Olshanetskii, V. Y., Glotka, A. A., & Kononov, V. V. (2021). Influence of the alloying system and dimensional mismatch of γ- and γ'- phase lattices on the strength characteristics of single-crystal heat-resistant nickel alloys. New Materials and Technologies in Metallurgy and Mechanical Engineering, (2), 6–10. https://doi.org/10.15588/1607-6885-2021-3-01

Received 29.01.2026
Accepted 11.02.2026
Published 31.03.2026

ОЦІНКА СТРУКТУРИ ТА ВЛАСТИВОСТЕЙ ЖАРОМІЦНОГО НІКЕЛЕВОГО СПЛАВУ ЖС32-ВІ ЯК МАТЕРІАЛУ ДЛЯ ВИГОТОВЛЕННЯ ЛОПАТОК ГАЗОТУРБІННИХ ДВИГУНІВ

Сергій Пучек — аспірант кафедри транспортних технологій Національного університету «Запорізька політехніка», м. Запоріжжя, Україна, *e-mail: puchek777@gmail.com*, ORCID: 0009-0007-8077-6106

Сергій Бєліков — д-р техн. наук, професор, професор кафедри транспортних технологій Національного університету «Запорізька політехніка», м. Запоріжжя, Україна, *e-mail: belikov@zp.edu.ua*, ORCID: 0000-0002-9510-8190

Мета роботи. *Вивчити макро- та мікроструктурний стан дослідних плавок жароміцного сплаву ЖС32-ВІ для виробництва відповідальних деталей газотурбінного двигуна, оцінити механічні властивості та жароміцність.*

Методи дослідження. *Параметри структурної стабільності оцінювали за відомими розрахунковими методиками PHACOMP та New PHACOMP. Макро- та мікроструктурний аналіз і дослідження фазового складу проводили методом оптичної металографії. Механічні властивості при кімнатній температурі визначали відповідно до вимог ISO 6892-84, СТ СЕВ 471-88, а випробування на тривалу міцність – відповідно до вимог ДСТУ ISO 204:2019.*

Отримані результати. *Проведено дослідження структури та властивостей зразків сплаву ЖС32-ВІ, отриманих у вакуумній печі FM 1-2-100 фірми “ULMAC” методом рівноосної кристалізації. Мікроструктура*

DOI 10.15588/1607-3274-2026-1-2

зразків до термічної обробки відповідає литому стану сплаву, а після термообробки – задовольняє технічним умовам та відповідає затвердженій шкалі мікроструктур. Механічні властивості та жароміцність відповідають вимогам технічної документації до відповідального жароміцного лиття.

Наукова новизна. *Отримано нові дані про структуру та фазовий склад жароміцного сплаву ЖС32-ВІ дослідних плавок. Метод розрахунку та аналітичної оцінки підтвердив високий рівень структурної стійкості.*

Практична цінність. *Отримані результати дають можливість розширити застосування жароміцного нікелевого сплаву ЖС32-ВІ для виготовлення виливків відповідального призначення.*

Ключові слова: *жароміцний сплав, макро- та мікроструктура, механічні властивості, жароміцність, гомогенізація.*

Список літератури

1. Sims Ch. T. Superalloys II: High-Temperature Materials for Aerospace and Industrial Power (2nd edition) [Текст] / Ch. T. Sims, N. S. Stoloff, W.C. Hagel - New York: John Wiley and Sons, 1987. – 615 p.

2. Miller H.E. Constructions of gas turbines and Superalloys / H. E. Miller, W.L, Chambers: in Superalloys II: High-Temperature Materials for Aerospace and Industrial Power (2nd edition) / Ch. T. Sims, N. S. Stoloff, W.C. Hagel – New York: John Wiley and Sons, 1987. – P. 27–56.

3. Гайдук С. В. Прогнозирование параметров структурной стабильности литейных жаропрочных никелевых сплавов / Гайдук С.В., Кононов В. В. // Вестник двигателестроения. – 2017. – № 1. – С. 139–148. https://doi.org.1558/1727-0219-2017-1-24

4. Чигрин В. С. Конструкция и прочность авиационных двигателей / Чигрин В. С. – Харьков : ХАИ, 2017. – 420 с.

5. Великанова Н. П. Влияние эксплуатационной наработки на кратковременные механические свойства жаропрочных сплавов для деталей турбин авиационных ГТД / Н. П. Великанова, П. Г. Великанов, А. С. Киселев // Вестник двигателестроения. – № 2. – 2011. – С. 239–243.

6. Sims Ch. T. The Superalloys / Ed. by C. T. Sims, W.C. Hagel – New York: John Wiley and Sons, 1972. – 614 p.

7. Superalloys II / Ed. by S. Birosca, S. Kolisnychenko. – Trans Tech Publications Ltd., Switzerland, 2020. – 520 p.

8. Reed R.C. The Superalloys. Fundamentals and Applications / R.C. Reed. – Cambridge, University Press. – 2006. – 372 p.

9. Технологическое обеспечение эксплуатационных характеристик деталей ГТД. Лопатки компрессора и вентилятора : монография. Часть 2: монография [Текст] / В. А. Богуслаев, Муравченко В. Ф., Жеманюк П.Д. и др. – Запорожье, 2017. – 493 с.

10. Матеріали і технології для лопаток вітчизняних промислових газових турбінних двигунів / Г.П. Мяльніца, А.М. Верховлюк, А.В. Нарівський та ін.: ред. В.В. Вероцька: НАН України, Фіз.-технол. Ін-т металів та сплавів: проект “Наукова книга”. – К. : Наукова думка, 2023. – 177 с.

11. Андриенко А. Г. Оценка влияния соотношения тантала к рению на структурную стабильность и механические свойства жаропрочного никелевого сплава ЖС-32 / А. Г. Андриенко, С. В. Гайдук, В. В. Кононов // Весник двигателестроения. – 2010. – №1. – С. 128–132.

12. Гайдук С. В. Комплексная расчетно-аналитическая методика для проектирования литейных жаропрочных никелевых сплавов / Гайдук С. В. // Новые материалы и технологии в металлургии и машиностроении. – 2015. –№2. – С. 92–103.

13. Saunders N. The Application of CALPHAD Calculations to Ni-Based Superalloys / N. Saunders, M. Fahrmann, C. J. Small // In “Superalloys 2000” eds. K.A. Green, T.M. Pollock, and R.D. Kissinger. – TMS. – Warrendale. – 2000. – P. 803–811.

14. Гайдук С. В. Наукові основи проектування ливарних жароміцних нікелевих сплавів з необхідним комплексом службових властивостей / С. В. Гайдук, С. Б. Бєліков. – Запоріжжя : ЗНТУ, 2017. – 80 с.

15. Гайдук С. В. Расчет фазового состава литейного свариваемого жаропрочного коррозионностойкого никелевого сплава методом CALPHAD / Гайдук С. В., Кононов В. В. // Вестник двигателестроения. – 2016. – № 1. – С. 107–112.

16. Гайдук С. В. Розвиток і застосування наукових принципів легування для розробки жароміцних нікелевих сплавів з гарантованими властивостями : дис. ... доктора техн. наук : 05.02.01 / Гайдук С. В. – Запоріжжя, ЗНТУ, 2018. – 404 с.

17. New PHACOMP and Its Applications to Alloy Design / M. Morinara, N. Yukawa, H. Adachi and H. Ezaki // Superalloys 1984 (eds M. Gelletal) AIME, 1984. – P. 523–532.

18. Yukawa N. Alloy design of superalloys by the d-electrons concept / N. Yukawa, M. Morinara, H. Ezaki, Y. Murata // Hight temperature alloys for gas turbines and other applications: Proceedings of Conference, Liege. Dordrecht : CRM, 1986. – P. 935–944.

19. С. Гайдук, В. Кононов. Оценка влияния тантала на критические температуры в литейном свариваемом жаропрочном никелевом сплаве с применением расчетных и экспериментальных методик. / Новые материалы и технологии в металлургии и машиностроении. – 2014. – № 2–6. – С. 34–40.

20. Гайдук С. В. Применение комплексной расчетно-аналитической методики для многокритериальной оптимизации составов литейных жаропрочных никелевых сплавов / С. В. Гайдук, В. В. Кононов, В. В. Куренкова // Современная электрометаллургия. – 2017. – № 1. – С. 44–51.

21. Ольшанецький В. Ю. Вплив системи легування та розмірної невідповідності решіток γ- і γ'- фаз на характеристики міцності монокристалічних жароміцних нікелевих сплавів / Ольшанецький В. Ю, О. А. Глотка, В. В. Кононов // Нові матеріали і технології в металургії та машинобудуванні. – 2021. – № 2. – С. 6–10. https://doi.org/10.15588/1607-6885-2021-3-01

DOI 10.15588/1607-3274-2026-1-2

UDC 621.316.13

Andrii Skrebtsov	Candidate of Technical Sciences, Associate Professor of the Department of Theoretical and Applied Mechanics, National University Zaporizhzhia Polytechnic, Zaporizhzhia, Ukraine, *e-mail: nic_tz@ukr.net,* ORCID: 0000-0002-4669-9625
Andrii Kononenko	Postgraduate Student of the Department of Mechanics of the National University Zaporizhzhia Polytechnic, Zaporizhzhia, Ukraine, *e-mail: andrju3952@gmail.com,* ORCID: 0009-0005-4268-0854
Julia Kononenko	Senior Lecturer of the Department of Physical Materials Science of National University Zaporizhzhia Polytechnic, Zaporizhzhia, Ukraine, *e-mail: juliakon7335@gmail.com,* ORCID: 0000-0002-0676-4015
Svetlana Kruzhnova	Senior lecturer of the Department of Theoretical and Applied Mechanics, National University Zaporizhzhia Polytechnic, Zaporizhzhia, Ukraine, *e-male: krulana2017@gmail.com*, ORCID: 0000-0002-7554-0322
Olga Omelchenko	Senior lecturer of the Department of Theoretical and Applied Mechanics, National University Zaporizhzhia Polytechnic, Zaporizhzhia, Ukraine, *e-male: omelchenko15@ukr.net,* ORCID: 0000-0001-8925-4178
Oleksiy Omelchenko	Postgraduate Student of the Department of machinery and foundry technology of the National University Zaporizhzhia Polytechnic, Zaporizhzhia, Ukraine, *e-mail*: *Kartzpua@gmail.com,* ORCID: 0009-0009-1693-395X

INFLUENCE OF STRUCTURAL FACTOR OF POWDER MATERIAL ON ELEMENTS STRENGTH

Purpose. *To investigate the influence of porosity and chemical composition on the strength of titanium structural components made from the unalloyed titanium alloy VT1-0, manufactured by powder metallurgy. The work aims to refine the methodology for calculating such components while taking into account the specific features of their structure, since the presence of pores contradicts the traditional hypothesis of material continuity.*

Research methods. *For the experiment, thermomechanical titanium powder PT5 was used. After pressing (700 MPa) and vacuum sintering (1250 °C, 180 min), the VT1-0 alloy was obtained. A comparative analysis of the structure and mechanical properties of the sintered material and its cast counterpart was carried out.*

Results. *The key structural distinction is the porosity of the sintered alloy, which is 13 %, with pores located mainly along grain boundaries. In terms of chem-ical composition, powder-based VT1-0 has twice the oxygen content (0.20 wt%) compared to the cast alloy (0.10 wt%). It is known that oxygen significantly increases the strength of titanium alloys; however, the ultimate strength of the sintered VT1-0 alloy was 330.5 MPa, which is 45.5 MPa lower than that of its cast counterpart (376.0 MPa). This is due to the presence of pores in the metal structure. Eliminating these pores will increase strength compared to a cast material of similar chemical composition and reduce its dispersion to that of a cast alloy.*

Scientific novelty. *The main conclusion of the study is that the reduction of the effective metal cross-section bearing the load (due to 13 % porosity) outweighs the strengthening effect of the higher oxygen and other substance's content. The presence of pores also leads to a significant increase in the scatter of strength and in some cases microhardness values. If we make a correction for the effective cross-sectional area minus the pores, the actual strength of the powder sample would be higher due to the increased oxygen and other substance's content.*

Practical value. *It was proved that the actual negative effect of porosity on strength is significantly outweighed by the strengthening effect resulting from microalloying with impurities during sintering. Given the high dispersion of the strength index, this effect can be explained by the fact that the influence of porosity on the ultimate strength is multidimensional and depends on factors such as pore shape and size, the presence of sharp corners in them and their volume fraction.*

Key words*: powder metallurgy, additive alloys, pores, material strength hypotheses, mechanical properties, strength, stress.*

DOI 10.15588/1607-3274-2026-1-3

Introduction

The development and implementation of powder metallurgy in the production of structural components requires refining the methods used to calculate the strength of these elements, taking into account the specific features of their structure. In the mechanics of materials, the assumption of material continuity states that a material must be solid and uninterrupted – meaning it should not contain cavities, cracks, or pores of various origins, as these act as stress concentrators. Materials produced from powders inherently contain pores of different shapes and sizes. One such material is the structural, non-alloyed titanium VT1-0, obtained via powder technology (PT).

For the sintered VT1-0 titanium alloy, its strength characteristics correspond to those of cast titanium of the same grade. However, some discrepancies in properties are observed. Specifically, the average ultimate strength of VT1-0 for bar-rolled products is 425 MPa, whereas for cast ingots this value is only 350 MPa. This discrepancy arises from differences in the structure of the billets, which, despite identical chemical composition, are influenced by technological parameters and the manufacturing method.

Analysis of research and publications

Titanium alloys are critically important materials for high-tech industries such as aerospace, automotive, and medical sectors due to their unique combination of high specific strength, corrosion resistance, and biocompatibility [1]. Traditional metallurgy for producing titanium castings is extremely expensive and energy-intensive, which motivates the development of alternative, cost-effective manufacturing methods. Powder metallurgy (PM), including its various forms (pressing and sintering) as well as additive manufacturing, offers pathways for producing near-net-shape components that significantly reduce material waste and machining costs. [1, 2] However, the widespread adoption of PM-titanium is limited by the need to ensure mechanical properties comparable to those of cast analogues. A similar challenge arises in additive manufacturing, where powders are also used. The main factors influencing the final material properties are residual porosity, impurity control, and thermomechanical processing technologies. [2, 3, 5].

Porosity is the most significant defect in powder-derived materials because pores act as stress concentrators, leading to premature failure. Studies on TiNbZrTa alloys, which are promising for biomedical applications, have shown that samples produced with minimal porosity exhibit significantly higher hardness compared to their porous counterparts [4]. This demonstrates the direct negative effect of porosity on static characteristics. Other studies [3, 5] have focused on controlling the final microstructure of the alloy to achieve the required performance characteristics.

Thus, there are two main approaches to reducing porosity: optimization of the sintering process and secondary processing. In [6], the authors investigated the influence of hot-pressing parameters on titanium with a bimodal microstructure, confirming that controlled adjustment of temperature and pressure is an effective means of managing the final porosity and mechanical behavior. The authors of [3] also established the importance of sintering temperature, using inductive hot pressing to produce titanium composites.

Complete elimination of porosity is not always necessary – for example, to ensure osteointegration in implants [7, 5]. In [7], it was shown that surface engineering through nitriding and burnishing significantly improves the wear resistance of a highly porous titanium alloy by closing surface pores and forming a nitride layer, without altering the properties of the underlying core.

As noted above, porosity regulation is a critical issue for titanium alloys. It can be addressed at the synthesis stage, but there are also methods and technologies that allow porosity reduction after the billet has been produced. Thermomechanical treatment is highly effective for titanium alloys. In [8], a sintered titanium alloy containing 5% iron and produced via powder metallurgy with a porosity of 10% was studied. The samples failed in a brittle manner, but hot rolling complicated the fracture process due to a sharp reduction in porosity. It was also reported that this treatment increased the tensile strength of the alloy to 960 MPa. These results indicate that porosity has a significant influence on alloy strength, and that additional thermomechanical processing can compensate for the limitations of the basic powder metallurgy process by effectively eliminating pores.

The effect of porosity becomes especially critical under cyclic loading. In [9], it was shown that for Ti-6Al-4V produced via Binder Jetting – a form of PM – residual internal porosity remains the primary cause of low fatigue life, even at relatively high densities (up to 95%). The authors demonstrated that to achieve reliability comparable to cast Ti-6Al-4V, hot isostatic pressing (HIP) is a necessary secondary operation. HIP effectively closes internal pores, raising the density to 99.8% and restoring fatigue strength [9].

In additive manufacturing, for example Electron Beam Melting (EBM), the microstructure and mechanical properties of the resulting material are influenced by technological factors such as build geometry and powder reuse. This highlights that quality-control challenges found in traditional PM remain relevant in advanced AM technologies as well, requiring careful parameter regulation [10].

Titanium powders typically contain an elevated oxygen content, which significantly increases material strength. However, excessive oxygen leads to brittleness and a drastic decrease in ductility. Therefore, controlling the material properties requires precise regulation of oxygen content in

DOI 10.15588/1607-3274-2026-1-3

titanium. Studies [2, 11] present a new sintering-deoxygenation process for Ti-6Al-4V powder that enables reduction of oxygen content, which is critically important for ensuring adequate ductility and reliability of the final material.

Titanium powders contain an elevated oxygen content, which significantly increases the material's strength. However, an excess of oxygen leads to brittleness and a substantial reduction in ductility. Therefore, controlling the material's properties is possible only through precise regulation of the oxygen content in titanium. Studies [2, 11] describe a new sintering – deoxygenation process for Ti-6Al-4V powder that allows reducing the oxygen content – critically important for ensuring the required ductility and reliability of the final material.

As in [8], the authors of [2, 7, 11] have shown that strength can be increased – while maintaining a controlled reduction in ductility – through the presence of "harmful" impurities in titanium (iron, oxygen, nitrogen). Thus, there is a clear relationship between porosity, impurity content (oxygen, nitrogen, iron), and the resulting mechanical properties.

Purpose

This scientific and practical work is devoted to a comprehensive analysis of the mechanical properties of structural elements made of technically pure unalloyed titanium alloy of the VT1-0 brand by the powder metallurgy method. Special emphasis is placed on the relationship between the level of residual porosity, chemical composition and actual strength of products made of such materials. The relevance of the work is due to the need for a fundamental review and improvement of existing methods of engineering calculation of structural components of mechanical engineering made of powders, since the specific microstructure of such materials, saturated with internal pores, directly contradicts the classical hypothesis of material continuity, which is the basis for the fundamental academic course of materials resistance. The study considers how the morphology of pores and the concentration of impurities affect the distribution of internal defects, which allows us to offer certain clarifications for predicting the reliability and durability of titanium parts in real operating conditions, ensuring the optimal balance between the weight of the structure and its ability to withstand critical loads. The aim of the work is to prove the need to improve the methods of calculating the strength of structural elements made of powder titanium alloy VT1-0 through a comprehensive analysis of the influence of porosity and chemical composition.

Material and research methods

To produce the sintered titanium alloy, thermomechanical titanium powder PT5 (Technical Specifications (of Ukraine) 14-10-026-98) (Table 1) was used as the base material, without fractional sieving (fraction −0.50/+0.16), i.e., in the as-supplied condition.

Table 1 – Chemical composition (impurities) of PT5 powder, wt% [12]

Fe	Cl	C	Si	N	O	H	Ti
0,08	0,06	0,03	0,04	0,03	0,20	0,01	base

After sintering the thermomechanical titanium powder PT5, the unalloyed titanium alloy VT1-0 was obtained. The requirements of the state standard for this alloy with respect to impurities are summarized in Table 2.

Table 2 – Chemical composition (impurities) of VT1-0, wt% [12].

Fe	C	Si	N	O	H	Ti
up to 0,25	up to 0,07	up to 0,1	up to 0,04	up to 0,2	up to 0,01	base

Compaction of the titanium samples was carried out on a DB2432A hydraulic press with a working pressure of 700 MPa. Sintering was performed in a laboratory vacuum electric furnace model SNVE-1.3.1/16 according to the following technological scheme: heating at a rate of V_{heat} = 20 C/min, followed by an isothermal hold of 180 minutes at a temperature of 1250 °C ± 10 °C in a protective atmosphere—vacuum at 13.3 Pa. After the hold, the samples were cooled together with the furnace, also under vacuum. The chemical composition of the experimental titanium alloys was determined using the spectral method with a SPECTROMAX spectrometer (manufactured by SPECTRO) in accordance with standard procedures from GOST 19863.1-91 to GOST 19863.12-91. The content of gaseous impurities – nitrogen, oxygen, and hydrogen – was measured separately according to industry standard OST 190013, using an ON900 gas analyzer (manufactured by ELTRA) at SE "ZTMK" as part of joint research work. Samples for metallographic examination were prepared using the standard procedure involving sequential grinding and polishing. Etching of the prepared sections was carried out in a special reagent containing 10 ml HF, 25 ml HNO_3, and 65 ml glycerin. Microstructural analysis was performed using a NEOPHOT-32 inverted reflected-light microscope manufactured by Carl Zeiss. Quantitative evaluation of porosity (volume fraction of pores) was conducted using the Rozival line method on an MIM-8M optical microscope.

Microhardness measurements were performed in accordance with the standard procedure DSTU 3827:2004 on a PMT-3 microhardness tester at a load of 0.49 N. Final microhardness values for different structural constituents were determined as the average of five measurements, based on the diagonal dimensions of the indentations. Mechanical testing was conducted according to the standard methodology.

DOI 10.15588/1607-3274-2026-1-3

Research results and their discussion

To evaluate the structure, metallographic analysis was performed on both the cast and the sintered VT1-0 titanium alloy produced from PT5 powder. Analysis of the microstructure of VT1-0 in the cast condition revealed the presence of β-transformed grains with a size of 150–200 µm. These grains consist of packets of parallel α-plates with a thickness of 4–10 µm, whose linear dimensions are comparable to the size of the primary β-grains (Fig. 1*a*).

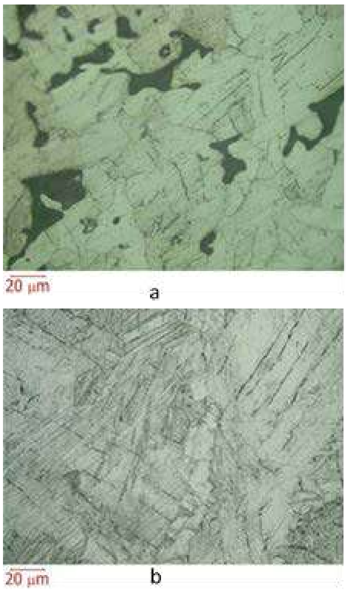

Figure 1. Microstructure of VT1-0 titanium alloy [12]:
a – cast VT1-0; *b* – powder-based VT1-0 (PT5)

The structure of the sintered powder titanium alloy produced from PT5 powder (see Fig. 1, b) consisted of α-phase grains and pores of various geometric shapes and sizes. The pores were located both within the grain volume and along grain boundaries, with the latter being the predominant location. The average size of the elongated α-grains did not exceed 100 µm.

Analysis of the structure (see Fig. 1*b*) shows that the sintered VT1-0 titanium alloy produced from PT5 powder contained pores of complex configuration, unevenly distributed throughout the volume of the workpiece. The pore area fraction on the polished section was 13 %, which resulted in a low material density, and their average size did not exceed 60 µm. Thus, the only difference between the alloys under investigation is their porosity.

Analysis of the microhardness measurements of the alloy grains showed that the values for the sintered titanium alloy are 50 MPa higher than those for the cast alloy (Table 3). At the same time, dispersion analysis indicated that the microhardness values do not exhibit the same spread relative to their mean. The microhardness dispersion of the sintered alloy is 5 units higher than the corresponding value for the cast titanium alloy.

Table 3 – Results of mechanical property testing of titanium alloys manufactured using different technologies [12]

Alloy		Mechanical properties								
		$\sigma_{\text{в}}$, MPa	$\boldsymbol{S}_{\sigma_{\text{в}}}$	δ, %	$\boldsymbol{S}_{\delta}$	ψ, %	$\boldsymbol{S}_{\psi}$	$\boldsymbol{H}^{\mathbf{04}}$, MPa	$\boldsymbol{S}_{\boldsymbol{H}\mu}$	ρ, %
cast	ВТ1-0	376,0	23,35	14,2	0,56	24,1	0,62	1400	45,46	-
sintered	ВТ1-0 (ПТ5)	330,5	75,12	5,0	0,21	7,5	0,25	1450	50,44	87,3

The ultimate strength of the sintered titanium alloy samples was 330.5 MPa, which is 45.5 MPa lower than the ultimate strength of cast VT1-0 titanium (376.0 MPa). However, analysis of the dispersion of this parameter showed that its value is significantly higher for the sintered alloys compared to the cast ones (75.12 and 23.35, respectively), which is attributed to the presence of pores.

The lower ductility of sintered powder alloys compared to cast VT1-0 is due to the presence of titanium compounds with nitrogen, oxygen, and hydrogen on the surface of the powder particles [13–15]. According to the literature [13 – 15], these compounds decompose under sintering temperatures, and the elements released during decomposition diffuse into the metal, thereby reducing its ductility. DSTU ISO 6892-1:2019 specifies that the ultimate tensile strength is calculated using a formula that is universally accepted for stress calculations in general engineering mechanics disciplines (such as strength of materials):

$$\boldsymbol{\sigma}_{\text{В}} = \frac{\boldsymbol{P}}{\boldsymbol{F_0}},$$

where $\boldsymbol{F_0}$ – cross-sectional area of the specimen; for a circular cross-section;

$$\boldsymbol{F_0} = \frac{\boldsymbol{\pi d^2}}{\boldsymbol{4}};$$

$\boldsymbol{d}$ – diameter of the cross-section;

$\boldsymbol{P}$ – value of the force that deforms the sample.

The cross-sectional area of the sample is determined by the formula $F_0 = 0{,}25\pi d^2$ and does not include the resulting pore area. When using the powder-derived VT1-0 titanium alloy, the effective cross-sectional area is reduced by the area of the pores present within the cross section. This can be taken into account in the formula for determining the ultimate strength as follows:

$$\boldsymbol{\sigma}_{\text{В}\boldsymbol{pores}} = \frac{\boldsymbol{N_{max}}}{\boldsymbol{F_0} - \boldsymbol{F_{pores}}},$$

where $\boldsymbol{F_{pores}}$ – the area of pores that fall into the plane of the cross section.

DOI 10.15588/1607-3274-2026-1-3

As noted in Tables 1 and 2, the chemical composition requirements for the materials are almost identical. The results of the chemical composition analysis of the examined materials are summarized in Table 4.

Table 4 – Chemical composition of the studied materals

Material	Average content of elements, wt%				
	Fe	**Si**	O_2	N_2	H_2
Cast	**0,25**	**0,1**	**0,10**	**0,04**0	**0,01**
Powder-based	-	-	**0,20**	**0,042**	**0,01**

As seen from the data in Table 4, the oxygen content in the VT1-0 structural titanium alloy produced from PT5 powder is twice as high. As previously noted, oxygen significantly increases the strength of the alloy. [14]. For every 0.1 wt% increase in oxygen, the strength of a titanium alloy increases by approximately 100 MPa. From Table 3, it can be seen that the ultimate tensile strength is 376.0 MPa and 330.5 MPa for the cast and powder-sintered alloys, respectively. Thus, the strength of the sintered alloy is 45.5 MPa lower, although, according to Table 4, its oxygen content is 0.1% higher. Assuming the sintered titanium alloy contained no pores and that the specimen cross-sectional area was the same, the strength of such a material could reach 450–500 MPa due to oxygen strengthening alone.

The pore content in the powder-sintered alloy was 13 %, which means a 13 % reduction of the cross-sectional area F_0 in the formula used to calculate ultimate strength. In other words, the actual cross-sectional area of the titanium specimen (for specimens with a working diameter of 5 mm) is 17.074 mm² instead of 19.625 mm². This implies that the ultimate strength of the sintered alloy should have been higher for the same applied force used in the laboratory test.

Taking into account both the higher oxygen content compared to the cast alloy and the reduced cross-sectional area due to the porosity of the sintered material, its strength should have been significantly higher than that of the cast alloy. However, the study revealed the opposite. As noted above, porosity led to an increase in the dispersion of ultimate strength values. In other words, the actual negative impact of porosity on strength far outweighs the strengthening effect produced by alloying.

Considering the high dispersion, this effect can be explained by the fact that the influence of porosity on ultimate strength is multidimensional and depends on factors such as pore shape, pore size, the presence of sharp edges, and their volumetric fraction.

Conclusions

The lower overall strength of the sintered sample, despite its elevated oxygen content, is attributable to its porosity. This strength can be increased by eliminating the pores.

The influence of pores on ultimate strength is complex and requires consideration of their shape, size, the presence of sharp edges, and their volumetric fraction.

References

1. Lario Femenia, J., Poler Escoto, R., Amigó Borras, V. (2023). Powder Metallurgy: A New Path for Advanced Titanium Alloys in the EU Medical Device Supply Chain. Metals 13, 372. https://doi.org/10.3390/met13020372

2. Gan, X., Li, S., Xiao, S. et al. (2024). Integrated high-performance and accurate shaping technology of low-cost powder metallurgy titanium alloys: A compre-hensive review. Int J Miner Metall Mater 31, 413–426 https://doi.org/10.1007/s12613-023-2774-7

3. Arévalo, C., Montealegre-Meléndez, I., Ariza, E., Kitzmantel, M., Rubio-Escudero, C., Neubauer, E. (2016). Influence of Sintering Temperature on the Microstructure and Mechanical Properties of In Situ Reinforced Titani-um Composites by Inductive Hot Pressing. Materials 9, 919. https://doi.org/10.3390/ma9110919

4. González-Guillén, C., Al Hawajreh Kamel, G., Degalez-Duran, E., Klyatskina, E., Naeem, M., Romero-Resendiz, L., Gonzalez, G., Amigó Borrás, V. (2023). The Effect of Ti/Ta Ratio and Processing Routes on the Hardness and Elastic Modulus of Porous TiNbZrTa Al-loys. Materials 16, 7362. https://doi.org/10.3390/ma16237362)

5. Pascu, C.I., Nicolicescu, C., Cioateră, N., Gheorghe, Ș., Geonea, I., Didu, A. (2022). Characterization of Tita-nium Alloy Obtained by Powder Metallurgy. Materials 15, 2057. https://doi.org/10.3390/ma15062057

6. Chávez-Vásconez, R., Lascano, S., Sauceda, S., Reyes-Valenzuela, M., Salvo, C., Mangalaraja, R.V., Gotor, F.J., Arévalo, C., Torres, Y. (2022). Effect of the Processing Parameters on the Porosity and Mechanical Behavior of Titanium Samples with Bimodal Microstruc-ture Produced via Hot Pressing. Materials 15, 136. https://doi.org/10.3390/ma15010136

7. Lavrys, S., Pohrelyuk, I., Padgurskas, J., Shliakhetka, K. (2023). Improving Wear Resistance of Highly Porous Titanium by Surface Engineering Methods. Coatings, 13, 1714. https://doi.org/10.3390/coatings13101714

8. Romero, C., Yang, F., Wei, S., Bolzoni, L. (2020). Thermomechanical Processing of Cost-Affordable Powder Metallurgy Ti-5Fe Alloys from the Blended Elemental Approach: Microstructure, Tensile Deformation Behavior, and Failure. Metals 10, 1405. https://doi.org/10.3390/met10111405

9. Alegre, J.M., Díaz, A., García, R., Peral, L.B., Lorenzo-Bañuelos, M., Cuesta, I.I. (2024). Mechanical and Fatigue Properties of Ti-6Al-4V Alloy Fabricated Using Binder Jetting Process and Subjected to Hot Isostatic Pressing. Materials 17, 3825. https://doi.org/10.3390/ma17153825

10. Wanjara, P., Backman, D., Sikan, F., Gholipour, J., Amos, R., Patnaik, P., Brochu, M. (2022). Microstructure and Mechanical Properties of Ti-6Al-4V Additively

DOI 10.15588/1607-3274-2026-1-3

Man-ufactured by Electron Beam Melting with 3D Part Nesting and Powder Reuse Influences. J. Manuf. Mater. Process. 6, 21. https://doi.org/10.3390/jmmp6010021

11. Mingyuan Zhang, Taotao Cai, Weiliang Lu, Shili Zheng, Ying Zhang, Yi Zhang (2023). Fabrication of Ti-6Al-4V alloy powder by a novel sintering-deoxygenation process. Journal of Alloys and Compounds. Volume 935, Part 1, 15. https://doi.org/10.1016/j.jallcom.2022.168113

12. Skrebtsov, A. A. (2015). Improving the mechanical and service properties of sintered titanium alloys: dis. cand. tech. sciences: 05.02.01. Zaporozhye

13. T. Chen, C. Suryanarayana, C. Yang (2023). Advanced titanium materials processed from titanium hydride powder. Powder Technology, Volume 423, 1 June. https://doi.org/10.1016/j.powtec.2023.118504

14. Zhang, H., Wang, C., Guo, J., Li, W., Cheng, C., Xiang, N., Huang, T., Niu, H., Zhang, D., Chen, F. (2004). Phase Transformation, Microstructural Evolution and Tensile Properties of a TiH_2-Based Powder Metallurgy Pure Titanium. Metals 14, 1218. https://doi.org/10.3390/met14111218

15. Radulescu R, Meleşcanu Imre M, Ripszky A, Rus F, Popa A, Moisa M, Funieru C, Ene R, Pituru S. (2024). Exploring the Broad Spectrum of Titanium-Niobium Implants and Hydroxyapatite Coatings-A Review. Materials (Basel). Dec 19; 17(24):6206. https://doi.org/10.3390/ma17246206

Received 16.02.2026
Accepted 01.03.2026
Published 31.03.2026

ВПЛИВ СТРУКТУРНОГО ФАКТОРУ ПОРОШКОВОГО МАТЕРІАЛУ НА МІЦНІСТЬ ЕЛЕМЕНТІВ

Андрій Скребцов	канд. техн. наук, доцент кафедри теоретичної та прикладної механіки Національного університету “Запорізька політехніка”, м. Запоріжжя, Україна, *e-mail: nic_tz@ukr.net,* ORCID: 0000-0002-4669-9625
Андрій Кононенко	аспірант кафедри кафедри теоретичної та прикладної механіки Національного університету «Запорізька політехніка», м. Запоріжжя, Україна, *e-mail: andrju3952@gmail.com,* ORCID: 0009-0005-4268-0854
Юлія Кононенко	старший викладач кафедри фізичного матеріалознавства Національного університету «Запорізька політехніка», м. Запоріжжя, Україна, *e-mail: juliakon7335@gmail.com,* ORCID: 0000-0002-0676-4015
Світлана Кружнова	старший викладач кафедри кафедри теоретичної та прикладної механіки Національного університету «Запорізька політехніка», м. Запоріжжя, Україна, *e-mail: krulana2017@gmail.com,* ORCID: 0000-0002-7554-0322
Ольга Омельченко	старший викладач кафедри теоретичної та прикладної механіки Національного університету «Запорізька політехніка», м. Запоріжжя, Україна, *e-mail: omelchenko15@ukr.net,* ORCID: 0000-0001-8925-4178
Олексій Омельченко	аспірант кафедри машин і технологій ливарного виробництва Національного університету «Запорізька політехніка», м. Запоріжжя, Україна, *e-mail: Kartzpua@gmail.com,* ORCID: 0009-0009-1693-395X

Мета роботи. *Дослідити вплив пористості та хімічного складу на міцність титанових конструкційних компонентів, виготовлених з нелегованого титанового сплаву ВТ1-0, отриманого методом порошкової металургії. Метою роботи є удосконалення методології розрахунку таких компонентів з урахуванням особливостей їхньої структури, оскільки наявність пор суперечить традиційній гіпотезі про суцільність матеріалу.*

Методи дослідження. *Для експерименту було використано термомеханічний титановий порошок ПТ5. Після пресування (700 МПа) та вакуумного спікання (1250 °С, 180 хв) було отримано сплав ВТ1-0. Було проведено порівняльний аналіз структури та механічних властивостей спеченого матеріалу та його литого аналога.*

Отримані результати. *Ключовою структурною відмінністю є пористість спеченого сплаву, яка становить 13%, з порами, розташованими переважно вздовж меж зерен. За хімічним складом порошковий ВТ1-0 має вдвічі більший вміст кисню (0,20 мас.%) порівняно з литим сплавом (0,10 мас.%). Відомо, що кисень значно підвищує міцність титанових сплавів. Ключовою структурною відмінністю спеченого сплаву є його пористість, яка становить 13%. За хімічним складом порошковий сплав ВТ1-0 містить вдвічі більше кисню (0,20 мас.%) порівняно з литим сплавом (0,10 мас.%). Відомо, що кисень значно підвищує міцність титанових сплавів; однак границя міцності спеченого*

DOI 10.15588/1607-3274-2026-1-3

сплаву ВТ1-0 становила 330,5 МПа, що на 45,5 МПа менше, ніж у його литого аналога (376,0 МПа). Це пов'язано з наявністю пор у структурі металу. Усунення цих пор збільшить міцність порівняно з литим матеріалом аналогічного хімічного складу та зменшить його дисперсію порівняно з литим сплавом.

Наукова новизна. *Основний висновок дослідження полягає в тому, що зменшення ефективного поперечного перерізу металу, що несе навантаження (через 13% пористість), переважує ефект зміцнення від вищого вмісту кисню та інших речовин. Наявність пор також призводить до значного збільшення розкиду значень міцності, а в деяких випадках і мікротвердості. Якщо зробити поправку на ефективну площу поперечного перерізу за вирахуванням пор, фактична міцність порошкового зразка буде вищою через збільшення вмісту кисню та інших речовин.*

Практична цінність. *В роботі доведено, що фактичний негативний вплив пористості на міцність значно переважає ефект зміцнення, що виникає внаслідок мікролегування домішками при спіканні. Враховуючи високу дисперсію показника міцності, цей ефект можна пояснити тим, що вплив пористості на границю міцності є багатовимірним і залежить від таких факторів, як форма та розмір пор, наявність у них гострих кутів та їх об'ємна частка.*

Ключові слова: *порошкова металургія, адитивні сплави, пори, гіпотези опору матеріалів, механічні властивості, міцність, напруження.*

Список літератури

1. Lario Femenia, J. Powder Metallurgy: A New Path for Advanced Titanium Alloys in the EU Medical Device Supply Chain / Lario Femenia, J., Poler Escoto, R., Amigó Borras V. // Metals. − 2023. – No. 13. – 372 p. https://doi.org/10.3390/met13020372

2. Integrated high-performance and accurate shaping technology of low-cost powder metallurgy titanium alloys: A comprehensive review / Gan, X., Li, S., Xiao, S. et al. // Int J Miner Metall Mater 31, – 2024. – P. 413–426. https://doi.org/10.1007/s12613-023-2774-7

3. Influence of Sintering Temperature on the Microstructure and Mechanical Properties of In Situ Reinforced Titanium Composites by Inductive Hot Pressing / Arévalo, C., Montealegre-Meléndez, I Ariza, E. et al. // Materials. − 2016. – No. 9. – 919 p. https://doi.org/10.3390/ma9110919

4. The Effect of Ti/Ta Ratio and Processing Routes on the Hardness and Elastic Modulus of Porous TiNbZrTa Alloys / González-Guillén, C., Al Hawajreh Kamel, G., Degalez-Duran, E. et al. // Materials. − 2023. – No. 16, 7362 p. https://doi.org/10.3390/ma16237362

5. Characterization of Titanium Alloy Obtained by Powder Metallurgy / Pascu, C.I., Nicolicescu, C., Cioateră, N. et al. // Materials. − 2022. − No. 15. – 2057 p. https://doi.org/10.3390/ma15062057

6. Effect of the Processing Parameters on the Porosity and Mechanical Behavior of Titanium Samples with Bimodal Microstructure Produced via Hot Pressing / Chávez-Vásconez, R, Lascano, S., Sauceda, S. et al. // Materials. − 2022. – No. 15. – 136 p. https://doi.org/10.3390/ma15010136

7. Improving Wear Resistance of Highly Porous Titanium by Surface Engineering Methods / Lavrys, S., Pohrelyuk, I., Padgurskas, J., Shliakhetka, K. // Coatings. − 2023. – No. 13. – 1714 p. https://doi.org/10.3390/coatings13101714

8. Thermomechanical Processing of Cost-Affordable Powder Metallurgy Ti-5Fe Alloys from the Blended Elemental Approach: Microstructure, Tensile Deformation Behavior, and Failure / Romero, C., Yang, F., Wei, S., Bolzoni, L. // Metals. − 2020. − No. 10. – 1405 p. https://doi.org/10.3390/met10111405

9. Mechanical and Fatigue Properties of Ti-6Al-4V Alloy Fabricated Using Binder Jetting Process and Subjected to Hot Isostatic Pressing / Alegre, J.M., Díaz, A., García, R. et al. // Materials. − 2024. – No. 17. – 3825 p. https://doi.org/10.3390/ma17153825

10. Microstructure and Mechanical Properties of Ti-6Al-4V Additively Manufactured by Electron Beam Melting with 3D Part Nesting and Powder Reuse Influences / Wanjara, P., Backman, D., Sikan, F. et al. // Manuf. Mater. Process. − 2022. – No. 6. – 21 p. https://doi.org/10.3390/jmmp6010021

11. Fabrication of Ti-6Al-4V alloy powder by a novel sintering-deoxygenation process / Mingyuan Zhang, Taotao Cai, Weiliang Lu et al. // Journal of Alloys and Compounds. Volume 935, Part 1, 15 February 2023. https://doi.org/10.1016/j.jallcom.2022.168113

12. Скребцов, А. А. Підвищення механічних та службових властивостей спечених титанових сплавів: дис. канд. техн. наук: 05.02.01 / А. А. Скребцов. – Запоріжжя, 2015.

13. Advanced titanium materials processed from titanium hydride powder / T. Chen, C. Suryanarayana, C. Yang // Powder Technology, Volume 423, 1 June 2023. − 118504. https://doi.org/10.1016/j.powtec.2023.118504

14. Phase Transformation, Microstructural Evolution and Tensile Properties of a TiH$_2$-Based Powder Metallurgy Pure Titanium / Zhang, H., Wang, C., Guo, J. et al. // Metals. − 2024. − No. 14. – 1218 p. https://doi.org/10.3390/met14111218

15. Exploring the Broad Spectrum of Titanium-Niobium Implants and Hydroxyapatite Coatings-A Review / Radulescu R, Meleșcanu Imre M, Ripszky A et al. // Materials (Basel). − 2024. − Dec 19;17(24):6206. https://doi.org/10.3390/ma17246206

DOI 10.15588/1607-3274-2026-1-3

p-ISSN 1607-6885 Нові матеріали і технології в металургії та машинобудуванні. 2026/1
e-ISSN 2786-7358 New materials and technologies in metallurgy and mechanical engineering. 2026/1

ТЕХНОЛОГІЇ ОТРИМАННЯ ТА ОБРОБКИ КОНСТРУКЦІЙНИХ МАТЕРІАЛІВ

TECHNOLOGIES OF OBTAINING AND PROCESSING OF CONSTRUCTION MATERIALS

UDC 669.017:621.78:539.4:621.771.29

Ihor Vakulenko — Doctor of Technical Sciences, Professor of the Department of Condensed State Physics of the Dnipro State Technical University, Kamianske, Ukraine, *e-mail: vakulenko_ihor@ukr.net*, ORCID: 0000-0002-7353-1916

Serhii Plitchenko — Candidate of Technical Sciences, Associate Professor of the Department of Applied Mechanics and Materials Science of the Ukrainian State University of Science and Technologies, Dnipro, Ukraine, *e-mail: plit4enko@ukr.net*, ORCID: 0000-0002-0613-2544

Tatyana Kalinina — Candidate of Technical Sciences, Associate Professor, Head of the Department of Condensed State Physics of the Dnipro State Technical University, Kamianske, Ukraine, *e-mail: kalinina_tv@ukr.net*, ORCID: 0000-0002-6806-3425

EFFECT OF AUSTENITE DEGRADATION CONDITIONS ON THE PROPERTIES OF STEEL 20

Purpose. *To investigate the nature of property changes in thermally strengthened coiled steel 20 depending on the mechanism of austenite degradation.*

Research methods. *The material for study was a wire with a diameter of 3 mm, made of low-carbon steel, with 0.22 % C, 0.46 % Mn, 0.088 % Si, 0.1 % Cr, 0.03 % S, 0.012 % P. The different structure state of the steel was obtained after certain processing. The samples, 0.3 m long, were subjected to austenitization at a temperature of 920 °C for 8 min, after that for 10 min followed isotherm exposure, at temperatures of 650–200 °C and tempering at temperature of isothermal transformation, duration by 60 min. The microstructure was studied using light and electron microscopy. Dimensions of structural element were determined by quantitative metallography methods. The mechanical properties were determined from analyzing tensile curves at room temperature and strain rate of* 10^{-3} s^{-1}.

Results. *The change at structure and properties is largely determined by the mechanism of austenite transformation under isothermal conditions. During diffusion transformation of austenite, the dispersion of the phase components is accompanied by an increase at super saturation of the solid solution by carbon. For the intermediate transformation region, a change at phase composition of the steel is added. The subsequent tempering determines the kinetics and degree of completion processes of structure formation of the thermally hardened rolled steel. At low tempering temperatures of steel with a bainite structure, hardening is due to the development of aging processes. With an increase at tempering temperature, the development of softening processes is accelerated.*

Scientific novelty. *The increase plasticity of the steel with a bainite structure is due to a decrease of dispersion of cementite particles, dislocation density, and the development of polygonization at initial stages of recrystallization. The softening of steel with a ferrite-pearlite structure is determined by a decrease in phase hardening during austenite transformation.*

Practical value. *Mechanism analysis of structural transformations has determined that manufacture of thermally strengthened rolled steel, the expected softening after coiling is recommended to compensate by a corresponding decrease of temperature of the end of accelerated cooling.*

Key words: *low-carbon steel, isothermal transformation, austenite, ferrite, pearlite, dispersion.*

Introduction

In metallurgical production, the enhancement of strength and service properties of products can be achieved via two fundamentally different technological approaches. The required phase composition of steel is obtained by adjusting the concentration ratios of chemical elements [1, 2], which ultimately determines the basic structure and property set of the rolled product. At the same time, the morphology and dispersion of phase constituents are governed by the conditions of the final stage of product manufacturing [2, 3].

DOI 10.15588/1607-3274-2026-1-4

Another approach to modifying the structure and properties of metallurgical products involves targeted variation of the heating and cooling temperature-rate parameters [4, 5]. This technology can be applied both to individual products and to billets at intermediate processing stages. The variety of such processing schemes is generally referred to as thermal strengthening technology.

Compared to altering the phase composition of steel through alloying, the use of thermal treatment technologies significantly expands the possibilities for structural modification during the production of iron-carbon alloys [6, 7]. This provides an additional factor for change not only in the morphology and dispersion of phase constituents, but also in their nature and quantitative ratio during structure formation [8].

The allotropic transformation of iron and the thermokinetic conditions of cooling form the basis for obtaining a variety of phase constituents, depending on the component ratios and the degree of undercooling relative to the critical temperatures of phase equilibrium.

Analysis of research and publication

Compared to the structure of low-carbon steel after hot plastic deformation, the use of thermal strengthening in the rolling mill flow leads to qualitative changes in the structure and the corresponding set of properties [9, 10]. Proportionally to the cross-sectional thickness of the rolled product, the complexity of achieving the critical cooling rate results in the formation of a structural gradient, starting from the surface with intensive heat removal. The continuous decrease in cooling rate with increasing distance from the surface determines the structural state and the corresponding set of properties [11]. Thus, the structural gradient formed along the cross-section of the rolled product is determined by the temperature at the end of forced cooling for a given metal volume [6].

Compared to the production of metallic products in the form of rods, the manufacture of rolled products wound into a bundle has its own specific features [12, 13]. One of these is the additional thermal effect on the metal after the completion of forced cooling and coiling into a bundle [14, 15]. Indeed, after coiling, the rolled product remains for some time under the influence of the final accelerated cooling temperature. The duration of this thermal exposure at tempering is proportional to the mass of metal in the coil. Therefore, additional holding at such temperatures inevitably affects the structure and the associated set of properties of the rolled product [1, 5].

Meeting certain challenges, the additional thermal effect on the structure and properties of thermally strengthened rolled steel, which is wound into a bundle, can be evaluated by modeling the structural transformation processes in the metal. For this purpose, thermal strengthening in the rolling mill flow and holding the metal at the coiling temperature can be represented as alternating isothermal transformation at a certain temperature (below A_{c1}) and holding at this temperature.

Research material and methodology

The material selected for the study was a 3 mm diameter low-carbon steel wire with the following chemical composition: 0.22 % C, 0.46 % Mn, 0.088 % Si, 0.1 % Cr, 0.03 % S, and 0.012 % P.

Different structural states of the steel were obtained through specific thermal treatments. Wire samples, 0.3 m in length, were austenitized at 920 °C for 8 minutes. This was followed by isothermal holding for 10 minutes at temperatures ranging from 650 °C to 200 °C, and subsequent tempering at the isothermal transformation temperature for 60 minutes. Heating to the austenitization temperature, isothermal holding, and tempering were carried out in molten mixtures of various salts.

Sample preparation for microstructural analysis was performed in accordance with the requirements of light and electron microscopy [16]. To reveal the microstructure, specimens were etched using a standard reagent (4 % HNO_3 solution in ethanol).

Mechanical properties, including strength, ductility, and the strain hardening coefficient, were determined by analyzing tensile curves [17, 18] obtained at room temperature and a strain rate of 10^{-3} s^{-1}.

In the first stage, the technical tensile diagram was converted into a true stress-strain diagram and then plotted in logarithmic coordinates (Fig. 1).

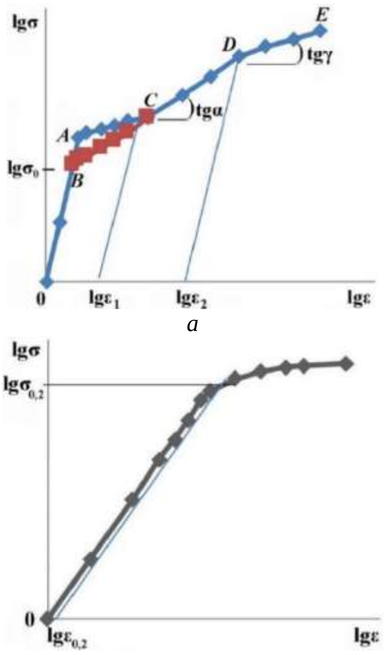

a

b

Figure 1. Schematic view of true tension diagrams in logarithmic coordinates:
a – with a section of discontinuous flow and *b* – without it

From the technical tensile curve in the coordinates "applied load (P_i) – sample elongation (Δl_i)", where elongation was calculated as $\Delta l_i = l_k - l_0$ (with l_0 and l_k being the initial and final gauge lengths, respectively), the true

DOI 10.15588/1607-3274-2026-1-4

stress (σ_i) and true strain (ε_i) were calculated. The calculation method was based on the assumption of constant of metal volume during plastic deformation.

True strain was calculated using the relation $\varepsilon_i = \ln(l_k/l_0)$.

To calculate the true stress (σ_i), it is necessary to estimate the current cross-sectional area (F_i) of the gauge section of the specimen after loading with force P_i. Considering the constancy of the metal volume in the gauge section, after elongation by Δl_i, the cross-sectional area decreases accordingly to the value F_i. Thus, the true stress is determined as: $\sigma_i = P_i/F_i$.

Based on the current values of σ_i and ε_i obtained from the true tensile curves (σ_i and ε_i), the strength characteristics were determined, including the yield strength (σ_y) and ultimate tensile strength (σ_S). The relative elongation (δ) was calculated using the relation: $\delta = [\Delta l_i/l0]\cdot 100$ %.

Further, by analyzing the constructed tensile curve in the coordinates $\lg \sigma_i - \lg \varepsilon_i$ (Fig. 1*a*), the strain hardening coefficient (n) was determined. This coefficient is the exponent in the equation $\sigma = K\cdot\varepsilon_n$, which describes the general form of the deformation curve. The value of n was determined as the tangent of the slope angle (α) in the initial segment (CD) of uniform strain hardening, according to: $\mathrm{tg}\alpha = \Delta\lg \sigma_i/\Delta\lg \varepsilon_i$.

Results and their discussion

The process of structure formation in thermally strengthened coiled steel after the completion of hot deformation can be divided into two stages. The first stage ends when the rolled product reaches a certain temperature after accelerated cooling. The structural state at this point corresponds to the conditions of isothermal austenite transformation at the temperature of the end of accelerated cooling.

In the second stage, structural transformations occur due to the thermal effect on the metal after it is coiled. In terms of its effect on the structure and properties of the metal, the thermal influence after coiling into a bundle is equivalent to tempering at the isothermal austenite transformation temperature [8, 11].

Accepting the concept of two-stage structure formation in rolled products, it is first necessary to consider the effect of the isothermal austenite transformation temperature on the structure and properties of low-carbon steel. In the temperature range up to the minimum stability of austenite, the diffusion transformation mechanism determines the morphology and dispersion of the structural constituents of the studied steel [19, 20]. At transformation temperatures starting from 650 °C, the structure consists of a small amount of regions similar to Widmanstätten ferrite (Fig. 2*a*), polyhedral ferrite grains, and pearlite colonies of defined dispersion. It should be noted that at isothermal austenite transformation temperatures under the diffusion mechanism, structure formation is determined by the quantitative ratios and dispersion of the structural constituents, without qualitative changes in the phase composition of the steel.

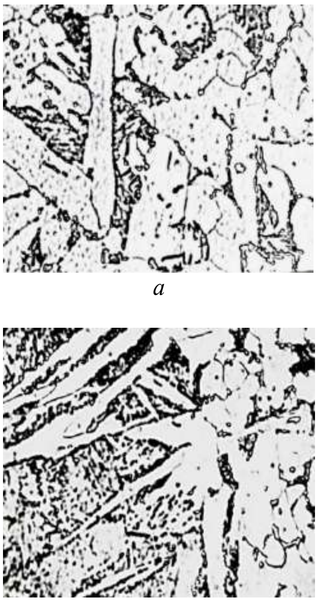
a

b

Figure 2. Microstructure of steel 20 after isothermal transformation at 650 °C (*a*) and 600 °C (*b*). Magnification: ×1000

Indeed, when the isothermal transformation temperature is reduced to 600 °C, alongside the refinement of structural constituents, a progressive decrease in the number of polyhedral ferrite grains is observed, accompanied by an increase in the fraction of Widmanstätten ferrite (Fig. 2*b*). The absence of qualitative changes in the steel structure at this transformation temperature is explained by the insufficient stability of austenite during cooling [11, 19], which is analogous to the effect of reduced carbon concentration in steel.

Further lowering the isothermal transformation temperature of austenite to the range of 500–400 °C, while structural refinement continues, leads to the emergence of initial signs of qualitative changes in the steel's phase composition (Fig. 3*a*). As the average size and volume fraction of polyhedral ferrite grains decrease, the amount of Widmanstätten ferrite increases [20], and changes in its morphology begin to appear (Fig. 3*b*).

A clear confirmation of this phenomenon is the microstructure of steel after isothermal transformation at 400 °C (Fig. 3*c*). Compared to the number of individual Widmanstätten ferrite plates formed at 500 °C (Fig. 3*a*), their quantity is significantly lower at 400 °C.

Proportional to the decrease in transformation temperature, the dispersion of compactly arranged cementite particles increases (Fig. 3*d*). Moreover, it should be noted that Widmanstätten ferrite begins to form in two distinct morphologies: as branched structures and as plate-like packets (Fig. 3*c*).

DOI 10.15588/1607-3274-2026-1-4

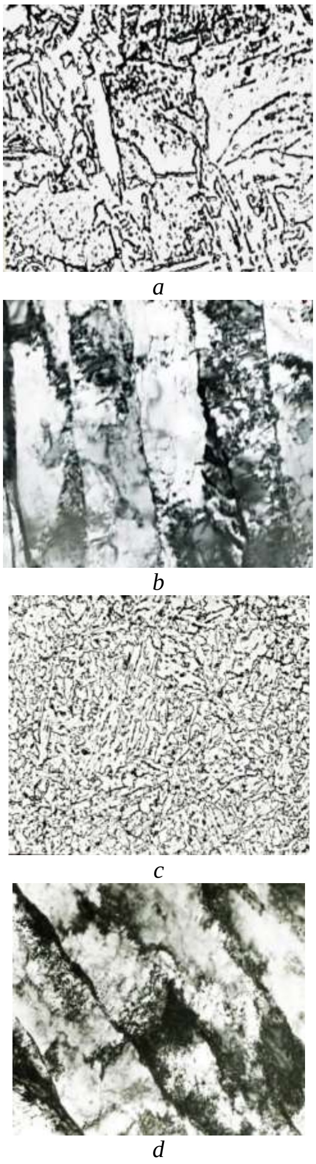

Figure 3. Microstructure of steel 20 after isothermal transformation at 500 °C (*a*, *b*) and 400 °C (*c*, *d*). Magnification: ×1000 (*a*, *c*), ×14,000 (*b*, *d*)

The observed structural changes should be considered as an approach to the temperature range where a change in the austenite transformation mechanism may occur [15, 19]. Based on this, when the isothermal transformation temperature drops below 400 °C, qualitative changes in the structural state of the steel are expected.

The microstructure formed after isothermal transformation at 300 °C and 200 °C confirms these expectations. Considering that even a slight decrease in the transformation temperature starting from 350 °C leads to a rapid reduction in the number of polyhedral ferrite grains [12, 20], their presence at 300 °C becomes difficult to detect (Fig. 4*a*, *b*).

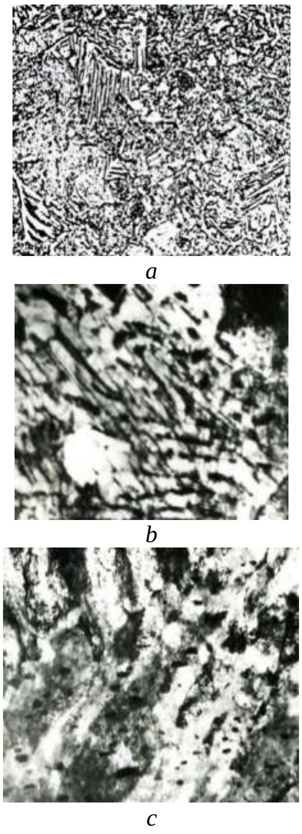

Figure 4. Microstructure of steel 20 after isothermal transformation at 300 °C. Magnification: ×1000 (*a*), ×18,000 (*b*, *c*)

Simultaneously, regions resembling highly dispersed pearlite colonies begin to appear (Fig. 4*b*), and the emergence of metal volumes with a bainite-like structure (Fig. 4*c*) should be considered as confirmation of the onset of qualitative changes. After lowering the isothermal transformation temperature to 200 °C, it becomes extremely difficult to identify any signs of austenite transformation via the shear mechanism based on the steel’s microstructure (Fig. 5).

The microstructure mainly consists of bainitic crystals (Fig. 5*a*, *b*) and a number of finely dispersed cementite particles with localized distribution (Fig. 5*c*). One of the reasons for the absence of martensite is the low stability of austenite in low-carbon steel due to the high temperature of onset of martensitic transformation (M_S). The M_S temperature can be estimated using the following relation:

$$M_S = 520 - 320(\%\,C) - 50(\%\,Mn) - 30(\%\,Cr) - 20(\%\,Ni + \%\,Mo) - 5(\%\,Si + \%\,Cu). \qquad (1)$$

where % C is concentration of the carbon and other chemical elements.

Using equation (1), the calculated martensite start temperature for the investigated steel is 423 °C, which corresponds well with known experimental data (420–400 °C) [12, 19]. Based on this, preventing intermediate decomposition of austenite during cooling and isothermal holding at 200 °C is a rather challenging task.

DOI 10.15588/1607-3274-2026-1-4

As a result of partial austenite decomposition, proportional to the degree of undercooling starting from temperatures around 400 °C, there is a gradual increase in the volume fraction of the bainitic component in the steel structure.

Overall, it can be considered that during isothermal holding of low-carbon steel at temperatures close to M_S, qualitatively similar structures are formed, differing only in the ratio of structural constituents and their dispersion [6, 11].

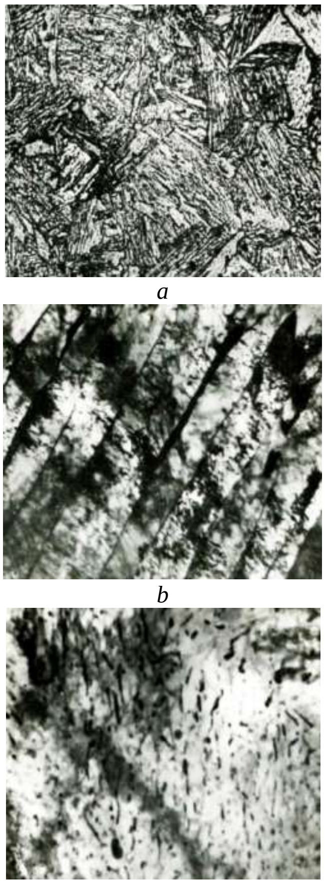
a

b

c

Figure 5. Microstructure of steel 20 after isothermal transformation at 200 °C. Magnification: ×1000 (*a*), ×18,000 (*b*, *c*)

When the temperature drops below M_S, the products of austenite transformation by the diffusion mechanism are gradually replaced by those formed via the intermediate mechanism [9]. The transformation of the steel structure depending on the isothermal austenite transformation temperature is accompanied by corresponding changes in mechanical properties (Fig. 6).

In view of the fact that range changes in the relative narrowing is 73–75 %, uniform elongation (δ_P) was used as a characteristic plasticity of the steel.

Analysis of presented dependencies shows that increasing the isothermal transformation temperature is accompanied by a predictable decrease in strength characteristics (Fig. 6*a*, *b*) and an increase in ductility (Fig. 6*c*). At the same time, the metal's ability for strain hardening changes according to a more complex relationship (Fig. 6*d*).

Overall, the non-monotonic nature of the changes in steel properties indicates the need to conventionally divide the temperature axis of the curves into separate regions: *I* (650–500 °C), *II* (450–350 °C), and *III* (300–200 °C).

For region *I* (Fig. 6), starting from 650 °C, the gradual decrease in the isothermal transformation temperature down to 500–450 °C is accompanied by a monotonic decrease in elongation (δ_P), an increase in strength characteristics (yield strength σ_y and ultimate tensile strength σ_S), and an increase in the metal's strain hardening ability (n).

This behavior of mechanical properties is explained by the evolution of the structure and changes in the phase composition of the steel. According to microstructural analysis, when the isothermal transformation temperature decreases from 650–600 °C (Fig. 2) to 500 °C (Fig. 3*a*, *b*), there are practically no qualitative changes in the structural state.

The phase composition remains constant, with only the quantitative ratio and dispersion of the structural constituents changing. In general, the increase in strength properties is due to the growth in the amount of Widmanstätten ferrite, the reduction in the size of polyhedral ferrite grains (d_P), and the thickness of the ferrite interlamellar spacing in pearlite colonies (λ) [2, 19].

According to stoichiometry for the investigated steel under nearly equilibrium conditions, the amount of pearlite does not exceed 30 %, for temperatures of 650–600 °C, d_P can be considered the main structural element.

At the same time, the presence of Widmanstätten ferrite may, to some extent, distort the influence of d_P on the overall properties of the steel.

Indeed, the well-known effect of ferrite grain size on strength characteristics will be observed only in the absence of excessive supersaturation of ferrite with carbon atoms and in the presence of substructural features.

When d_P serves as the main structural element for low-carbon steel, the strain hardening coefficient and plasticity of steel are directly proportional [22].

For pearlite colonies, a qualitatively different relationship is observed: a decrease in λ leads to a decrease in n, which promotes an increase in the ductility of eutectoid steel. Thus, as the transformation temperature decreases from 650 to 500 °C, the reduction in d_P, along with an increase in the amount of Widmanstätten ferrite and a higher degree of ferrite supersaturation with carbon atoms, contributes to a decrease in elongation (δ_P). Considering that the dispersion of pearlite colonies should increase δ_P, the amount of pearlite is insufficient to compensate for the effect of d_P, resulting in an overall decrease in δ_P. At the same time, the strain hardening coefficient and d_P are inversely proportional (Fig. 6*c*, *d*).

DOI 10.15588/1607-3274-2026-1-4

A further decrease in the isothermal austenite transformation temperature in region *II* is accompanied, similarly to region *I*, by an increase in strength and a decrease in relative elongation. The exception is the behavior of the strain hardening coefficient *n*.

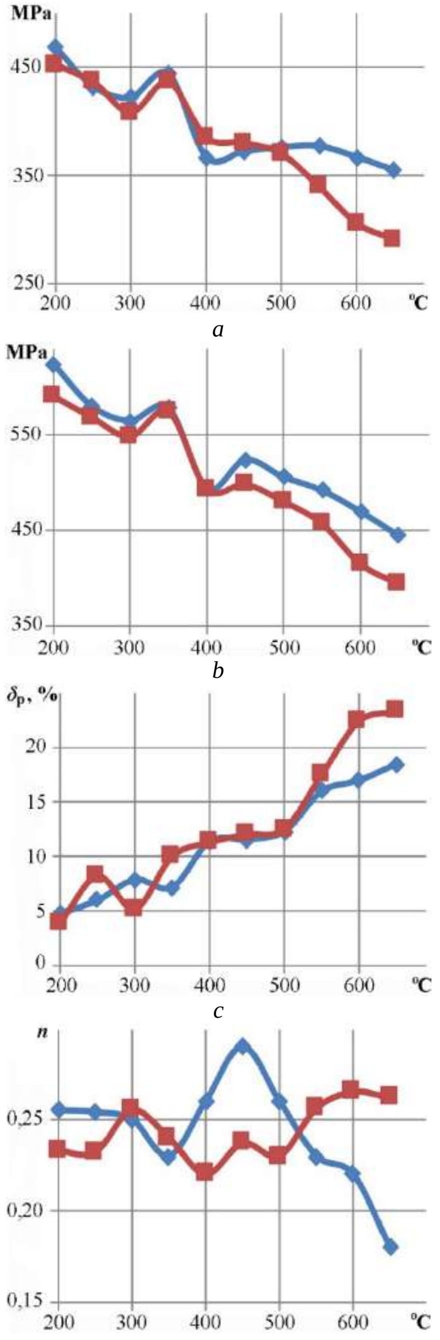

a

b

c

d

Figure 6. Variation of yield strength (*a*), ultimate tensile strength (*b*), uniform elongation (δ_P) (*c*), and strain hardening coefficient (*n*) (*d*) depending on the isothermal transformation temperature (♦) and subsequent tempering at this temperature (■)

The nature of the dependence of *n* indicates the emergence of structural changes in the steel that can influence the development of strain hardening processes (Fig. 6*d*). Indeed, microstructural analysis (Fig. 3*c*) shows that lowering the isothermal transformation temperature from 450–400 °C is accompanied by an increase in the amount of Widmanstätten ferrite due to a decrease in the number of polyhedral ferrite grains. Simultaneously, there is an increase in regions containing locally distributed dispersed cementite particles, similar to remnants of pearlite colonies. Moreover, according to studies [19, 20] of steels with similar composition, after isothermal austenite transformation at 450–400 °C, the structure is expected to contain areas resembling bainitic crystals. Thus, the appearance of the bainitic phase should be considered one of the reasons for qualitative changes in the property dependencies of the steel.

Against the background of a sharp decrease in the strain hardening coefficient in the temperature range of 450–400 °C, the ability of the bainitic phase to undergo plastic deformation [11] should be regarded as one of the reasons for the change in the rate of decrease of elongation δ_P. On the other hand, at 350 °C, the almost complete disappearance of Widmanstätten ferrite and the increase in the amount of bainitic phase, together with the refinement of cementite particles and a decrease in the amount of pearlite colonies (Fig. 4*a*, *b*), collectively lead to a sharp reduction in the ductility of the steel.

As an additional source of δ_P reduction, the differences in the strain hardening ability of bainite and pearlite should be considered, as confirmed by the relationship between n and δ_P (Fig. 6*d*, designation ♦).

Region *III*. Lowering the temperature from 300 to 200 °C results in the formation of a bainitic structure (Fig. 4, 5). This promotes an increase in the strain hardening effect, which is primarily due to the supersaturation of the solid solution with carbon atoms during bainite formation [2, 11] and dispersion strengthening from carbide phase particles (Fig. 4*b*, *c*) [20, 21].

Compared to isothermal transformation, the additional effect of tempering has a distinct impact on the nature of property changes in the steel (Fig. 6). In general, the difference in the dependence of mechanical properties on tempering temperature is reasonably consistent with the formed structural state of the metal. On the other hand, it should be noted that the tempering temperature has a different effect on the change of specific properties. This is due to the dependence of steel properties on the development of strain hardening processes.

Thus, for the temperature range from 200 to 500 °C, significant differences in the values of σ_y and δ_P are observed at a tempering temperature of about 500 °C (Fig. 7*a*, *c*), while for σ_S and the strain hardening coefficient (Fig. 7*d*), the temperature is lower and is approximately 400 °C (Fig. 7*b*).

DOI 10.15588/1607-3274-2026-1-4

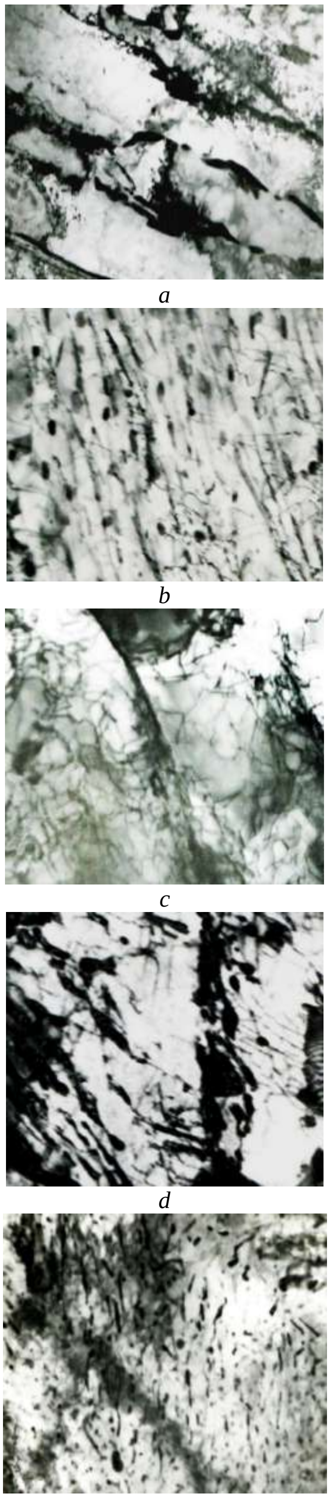

a

b

c

d

e

Figure 7. Microstructure of steel 20 after isothermal transformation at 500 °C and tempering at the same temperature (*a*, *b*); at 600 °C (*c*, *d*); and at 650 °C (*e*). Magnification: ×6000 (*a*), ×10,000 ×1.5 (*b*–*e*)

Compared to yield strength (σ_y), the lower tempering temperature at which differences in ultimate tensile strength (σ_S) appear is attributed to the development of strain hardening processes. Considering that in the region of initial plastic deformation (at the level of σ_y), the contribution of strain hardening is minimal [22], while at the level of σ_S, its influence becomes significant. The nature of the dependence of the strain hardening coefficient (*n*) on tempering temperature (Fig. 7*d*) confirms this reasoning. Based on this, it can be concluded that minor structural changes during tempering, to which σ_y is insensitive, will affect σ_S due to the development of strain hardening.

Compared to strength properties, the strain hardening coefficient is a more sensitive indicator of structural changes, both after isothermal transformation and subsequent tempering. Indeed, qualitative changes in the phase composition of steel due to isothermal transformation temperature correspond to changes in the nature of the *n*-dependence, with clear segmentation between regions (Fig. 6*d*).

After the temperature range of 200–300 °C lies the region of 350–450 °C (Fig. 6*d*), which corresponds to the transition from substructural strengthening to the emergence of strengthening due to the presence of ferrite grain boundaries [16, 17]. Thus, the nearly identical behavior of property changes up to 450–500 °C indicates the absence of qualitative differences in the metal's structure. Compared to isothermal transformation at 500 °C (Fig. 3*b*, *d*), additional tempering at this temperature leads to dislocation redistribution within Widmanstätten ferrite regions (Fig. 7*a*). These changes visually correspond to the development of polygonization processes. As a result of sub-boundary formation, ferrite grains are subdivided into microvolumes and partially cleared of unconnected dislocations (Fig. 7*a*). At the same time, dispersed particles that are excretion at sub-boundaries contribute to the development of dispersion strengthening.

Dislocation redistribution is inevitably accompanied by their annihilation, reducing the accumulated dislocation density resulting from phase hardening after isothermal austenite transformation.

Similar structural changes are observed in ferrite microvolumes with compactly arranged cementite particles (Fig. 7*b*). Dislocations blocked at cementite particles form a sub-boundary-like network. However, the extent of structural evolution during tempering is insufficient to fully explain the nature of property changes. The relatively small softening effect after tempering at 500 °C (Fig. 6) should be considered as the result of competing structural transformation processes. The softening effect from polygonization is partially offset by dispersion strengthening from cementite particles precipitated along sub-boundaries during tempering.

As the tempering temperature increases, the acceleration of diffusion-driven mass transfer enhances the softening effect. The initial stages of dislocation redistribution at 500 °C are further intensified at 550–600 °C (Fig. 7*c*, *d*).

In addition to polygonization, tempering at 600 °C is accompanied by the onset of recrystallization processes in regions of Widmanstätten ferrite (Fig. 7*c*).

DOI 10.15588/1607-3274-2026-1-4

Visually, this is manifested as a change in the development of recrystallization mechanism – from the migration of high-angle grain boundaries to the disappearance of low-angle boundaries, similar to those separating adjacent plates of Widmanstätten ferrite (Fig. 7*c*) [11, 16]. This recrystallization mechanism is typical for alloys with structures formed through the presence of boundaries with misorientation angles in the range of 1.5–2°.

Due to the low energy of such boundaries, no additional energy is required for their migration during recrystallization; instead, neighboring subgrains merge through the elimination of the boundary between them [16]. The growth of subgrains, via a mechanism similar to coalescence, is partially hindered by the presence of dispersed cementite particles (Fig. 7*d*), which also act as obstacles to dislocation annihilation [23].

Overall, recrystallization in Widmanstätten ferrite regions leads to the formation of polyhedral ferrite grains, similar to those shown in Fig. 2*a*.

Moreover, considering the interdependence of the process's ferrite recrystallization, spheroidization and cementite coalescence processes, the localized distribution of cementite particles contributes to the refinement of ferrite grains.

As a result, tempering at 600 °C leads to the formation of a highly heterogeneous ferrite structure (Fig. 7*d*). Similar structural changes are observed in steel tempered at 650 °C (Fig. 7*e*).

Compared to the structure after isothermal austenite transformation, where the strain hardening coefficient (n) and elongation (δ_P) are mostly inversely related (Fig. 8), additional tempering starting from 500 °C results in a direct proportional relationship between these characteristics (Fig. 6*c*, *d* and 8).

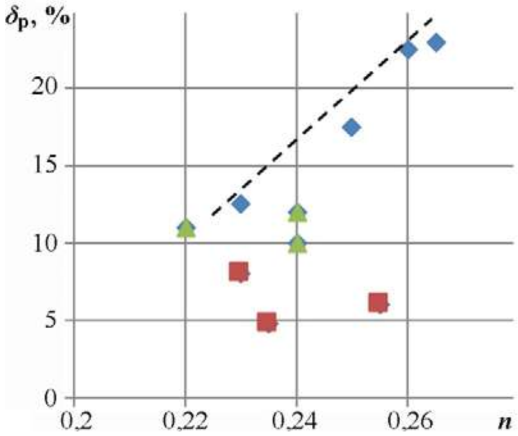

Figure 8. Correlation between elongation (δ_P) and strain hardening coefficient (n) after isothermal transformation and tempering within the temperature ranges: 500–650 °C (♦); 350–450 °C (▲); 200–300 °C (■)

The validity of this correlation is confirmed by the increase in ductility of low-carbon steel during cold rolling, which is proportional to the ferrite grain size. In fact, the observed relationship is based on the enhanced ability of low-carbon steels to undergo strain hardening, which increases proportionally with ferrite grain size [22].

Detailed analysis of substructural changes in deformed low-carbon steel has shown that the direct correlation between ferrite grain size (d_P), strain hardening coefficient (n), and elongation (δ_P) is rooted in the ability of the dislocation cell structure to evolve. The larger the ferrite grain size, the earlier the breakdown of uniform dislocation distribution into periodic structures begins, even at lower accumulated dislocation densities [16, 17].

Considering that the size of a dislocation cell is proportional to the ferrite grain size, the larger the d_P, the smaller the difference in dislocation concentration between the cell boundary and its interior.

As a result, the larger the dislocation cell and the lower the total dislocation density, the greater the cell's ability to evolve during metal deformation. Therefore, in low-carbon steel, the capacity for dislocation accumulation until reaching the maximum allowable concentration increases proportionally with ferrite grain size. Consequently, the increase in ductility of low-carbon steel with increasing ferrite grain size is fully justified. In this context, the strain hardening coefficient in low-carbon steel subjected to significant plastic deformation is often used as a controlling parameter.

Conclusions

The influence of the isothermal transformation temperature on the balance between strength and ductility of steel characteristics of low-carbon rolled products is determined by the mechanism of austenite degradation and the duration of holding after coiling into a bundle. Based on the analysis of the research results, it was found that the increase in ductility of steel during austenite transformation via the intermediate mechanism is achieved through the growth of cementite particle size, reduction in dislocation density due to polygonization, and the onset of recrystallization. For steel with ferrite-pearlite structures, ductility is proportional to the reduction in phase hardening effects and the degree of ferrite supersaturation with carbon atoms.

From a technological standpoint, the softening effect of coiled into a bundle thermally strengthened steel is proposed to be compensated by appropriately lowering the final temperature of forced cooling. This temperature should be determined based on the level of metal strengthening and the coil mass.

References

1. Liu, M., Wang, J., Zhang, Q., Hu, H., & Xu, G. (2021). Optimized properties of a quenching and partitioning steel by quenching at fine martensite start temperature. Metals and Materials International, 27, 2473–2480. https://doi.org/10.1007/s12540-020-00726-5.

DOI 10.15588/1607-3274-2026-1-4

2. Deineko, L. M., Borysenko, A. Yu., Taranenko, A. A., Zaitseva, T. O., & Romanova, N. S. (2021). Features of the ferrite-bainite structure low-alloy low-carbon steel after heat hardening and subsequent tempering. Metal Science and Heat Treatment of Metals, 2(93), 33–47. https://doi.org/10.30838/J.PMHTM.2413.270421.33.739

3. Liu, J.-H., Binot, N., Delagnes, D., & Jahazi, M. (2021). Influence of the cooling rate below Ms on the martensitic transformation in a low alloy medium-carbon steel. Journal of Materials Research and Technology, 12, 234–242. https://doi.org/10.1016/j.jmrt.2021.02.075

4. Morawiec, M., Skowronek, A., Król, M., & Grajcar, A. (2020). Dilatometric analysis of the austenite decomposition in undeformed and deformed low-carbon structural steel. Materials, 13(23), 5443. https://doi.org/10.3390/ma13235443

5. Bharadwaj, R., Sarkar, A., & Rakshe, B. (2022). Effect of cooling rate on phase transformation kinetics and microstructure of Nb–Ti microalloyed low carbon HSLA steel. Metallography, Microstructure, and Analysis, 11, 661-672. https://doi.org/10.1007/s13632-022-00864-9

6. Beketov, O. V., Laukhin, D. V., Osypchuk, M. M., Pomazan, A. R., & Radko, O. V. (2025). Study of the influence of accelerated cooling on the kinetics of destruction of low-carbon low-alloy steels. Ukrainian Journal of Civil Engineering and Architecture, (1)025, 17–24. https://doi.org/10.30838/UJCEA.2312.270225.17.1124

7. Mondal, J., Das, K., & Das, S. (2021). Isothermal transformation kinetics, microstructure and mechanical properties of a carbide free bainitic steel. Materials Characterization, 177, 111166. https://doi.org/10.1016/j.matchar.2021.111166

8. Zhang, J., Gu, S., Wang, J., Wei, F., Li, Z., Zeng, Z., Shen, B., & Li, C. (2024). Effect of isothermal transformation temperature on the microstructure, precipitation behavior, and mechanical properties of anti-seismic rebar. High Temperature Materials and Processes, 43(1), 20240028. https://doi.org/10.1515/htmp-2024-0028

9. Li, J., Yang, Z., Ma, H., Chen, C., & Zhang, F. (2023). A medium-C martensite steel with 2.6 GPa tensile strength and large ductility. Scripta Materialia, 228, Article 115327. https://doi.org/10.1016/j.scriptamat.2023.115327

10. Singh, P. P., Ghosh, S., & Mula, S. (2022). Strengthening behaviour and failure analysis of hot-rolled Nb+V microalloyed steel processed at various coiling temperatures. Materials Science and Engineering: A, 859, 144210. https://doi.org/10.1016/j.msea.2022.144210

11. Vakulenko, I., Plitchenko, S., Gubarev, S., & Khlebnikov, A. (2024). Structural changes during thermal strengthening of the railway wheel. New Materials and Technologies in Metallurgy and Mechanical Engineering, 2, 6-12. https://doi.org/10.15588/1607-6885-2024-2-11

12. Gu, C., Scott, C., Fazeli, F., Gaudet, M. J., Su, J., Wang, X., Bassim, N., & Zurob, H. (2023). Evolution of the microstructure and mechanical properties of a V-containing microalloyed steel during coiling. Materials Science and Engineering: A, 880, 145332. https://doi.org/10.1016/j.msea.2023.145332

13. Dai, M., Hu, Y., Hao, Y., Qiu, P., & Xiao, H. (2025). Analysis of temperature and stress fields in the process of hot-rolled strip coiling. Metals, 15(2), 111. https://doi.org/10.3390/met15020111

14. Dai, M., Liang, S., Qiu, P., & Xiao, H. (2024). Efficient finite element simulation of cold rolled strip coiling process considering additional contact deformation between layers. ISIJ International, 64, 1037-1046. https://doi.org/10.2355/isijinternational.ISIJINT-2023-405

15. Wang, C., Wu, H., & Zhang, Y. (2024). Structural transformation behavior of oxide scale during coiling of 0.9wt% Cr-containing high-strength steel. Journal of Materials Research and Technology, 30, 840–853. https://doi.org/10.1016/j.jmrt.2024.03.094

16. Sukhomlin, G. (2013). Special boundaries in ferrite of low-carbon steels. Metallophysics and Advanced Technologies, 35(9), 1237-1249 [in Russian]. Retrieved from http://dspace.nbuv.gov.ua/bitstream/handle/123456789/104215/11-Sukhomlin.pdf?sequence=1

17. Vakulenko, I.O., Vakulenko, L.I., Bolotova, D.M., Kurt, B., Asgarov, H., & Colova, O. (2022). Influence structure on the plasticity of carbon steel of the railway wheel rim in operation. Scientific Journal of Silesian University of Technology, Series Transport, 115, 183-192. http://dx.doi.org/10.20858/sjsutst.2022.115.13

18. Tsuchida, N., Inoue, T., & Nakado, H. (2013). Effect of ferrite grain size on the estimated true stress –strain relationship up to the plastic deformation limit in low carbon ferrite – cementite steels. Journal of Materials Research, 28(18), 2171–2179. https://doi.org/10.1557/jmr.2013.221

19. Vakulenko, I., Plitchenko, S., Bolotova, D., & Asgarov, Kh. (2023). Influence hot plastic deformation on the structure and properties of carbon steel of the railway wheel. Scientific Journal of Silesian University of Technology, Series Transport, 121, 257–266. https://doi.org/10.20858/sjsutst.2023.121.16

20. Zhao, S., Min, N., & Li, W. (2022). Formation of Widmanstätten ferrite and grain boundary ferrite in a hypereutectoid pearlitic steel. Metals, 12(3), 493. https://doi.org/10.3390/met12030493

21. Liu, G., Li, Y., Liao, T., Wang, S., Lv, B., Guo, H., Huang, Y., Yong, Q., & Mao, X. (2023). Revealing the precipitation kinetics and strengthening mechanisms of a 450 MPa grade Nb-bearing HSLA steel. Materials Science and Engineering: A, 884, Article 145506. https://doi.org/10.1016/j.msea.2023.145506

22. Vakulenko, I. A., Plitchenko, S., & Yılmaz, A. F. (2025). Influence degree and scheme of hot reduction on properties of the carbon steel. Manufacturing Technologies and Applications, 6(1), 150–156. https://doi.org/10.52795/mateca.1634663.

DOI 10.15588/1607-3274-2026-1-4

23. Wang, J., Hong, H., Huang, A., Yang, X., Qian, R., & Shang, C. (2022). New insight into the relationship between grain boundaries and hardness in bainitic/martensitic steels from the crystallographic perspective. Materials Letters, 308, 131105. https://doi.org/10.1016/j.matlet.2021.131105

Received 02.02.2026
Accepted 17.02.2026
Published 31.03.2026

ВПЛИВ УМОВ ДЕГРАДАЦІЇ АУСТЕНІТУ НА ВЛАСТИВОСТІ СТАЛІ 20

Ігор Вакуленко — д-р техн. наук, професор, професор кафедри фізики конденсованого стану Дніпровського державного технічного університету, м. Кам’янське, Україна, *e-mail: vakulenko_ihor@ukr.net*, ORCID: 0000-0002-7353-1916

Сергій Плітченко — канд. техн. наук, доцент, доцент кафедри прикладної механіки та матеріалознавства Українського державного університету науки і технологій, м. Дніпро, Україна, *e-mail: plit4enko@ukr.net*, ORCID: 0000-0002-0613-2544

Тетяна Калініна — канд. техн. наук, доцент, завідувач кафедри фізики конденсованого стану Дніпровського державного технічного університету, м. Кам’янське, Україна, *e-mail: kalinina_tv@ukr.net*, ORCID: 0000-0002-6806-3425

Мета роботи. *Досліджено характер зміни властивостей термічно зміцненого бунтового прокату зі сталі 20 залежно від механізму деградації аустеніту.*

Методи дослідження. *Матеріалом для дослідження обраний дріт діаметром 3 мм з низьковуглецевої сталі, з 0,22 % C, 0,46 % Mn, 0,088 % Si, 0,1 % Cr, 0,03 % S, 0,012 % P. Різний структурний стан сталі отримували після певної обробки. Зразки довжиною 0,3 м піддавали аустенітизації при температурі 920 °С протягом 8 хв, ізотермічно витримували 10 хв, при температурах 650 – 200 °С та піддавали відпуску при температурі ізотермічного перетворення тривалістю 60 хв. Мікроструктуру досліджували з використанням світлової і електронної мікроскопії на просвіт. Розміри структурного елемента визначали за методиками кількісної металографії. Механічні властивості визначали за аналізом кривих розтягу за кімнатної температури та швидкості деформації* 10^{-3} *с*$^{-1}$.

Отримані результати. *Зміна структури і властивостей в більший мірі визначаються механізмом перетворення аустеніту за ізотермічних умов. За дифузійного перетворення аустеніту, диспергування фазових складових супроводжується зростанням пересичення твердого розчину на вуглець. Для області проміжного перетворення додається ще зміна фазового складу сталі. Наступний відпуск визначає кінетику та ступінь завершення процесів структуроутворення термічно зміцненого бунтового прокату. За низьких температур відпуску сталі зі структурою бейніту, зміцнення обумовлено розвитком процесів старіння. За підвищення температури відпуску прискорюється розвиток процесів пом’якшення.*

Наукова новизна. *Збільшення пластичності сталі з бейнітною структурою обумовлене зниженням дисперсності частинок цементиту, щільності дислокацій, розвитком полігонізації та початкових стадій рекристалізації. Пом’якшення сталі з ферито-перлітною структурою визначається зменшенням фазового наклепу при перетворенні аустеніту.*

Практична цінність. *За аналізом механізму структурних перетворень визначено, що при виготовленні термічно зміцненого прокату, очікуване пом’якшення після змотки в бунт можливо компенсувати відповідним зниженням температури кінця прискореного охолодження.*

Ключові слова: *низьковуглецева сталь, ізотермічне перетворення, аустеніт, ферит, перліт, дисперсність.*

Список літератури

1. Optimized properties of a quenching and partitioning steel by quenching at fine martensite start temperature [Text] / M. Liu, J. Wang, Q. Zhang, H. Hu, G. Xu // Metals and Materials International. – 2021. – Vol. 27. – P. 2473–2480. https://doi.org/10.1007/s12540-020-00726-5.

2. Features of the ferrite-bainite structure low-alloy low-carbon steel after heat hardening and subsequent tempering [Text] / L. M. Deineko, A. Yu. Borysenko, A. A. Taranenko, T. O. Zaitseva, N. S. Romanova // Metal Science and Heat Treatment of Metals. – 2021. – No. 2 (93). – P. 33–47. https://doi.org/10.30838/J.PMHTM.2413.270421.33.739

3. Influence of the cooling rate below Ms on the martensitic transformation in a low alloy medium-carbon steel [Text] / J.-H. Liu, N. Binot, D. Delagnes, M. Jahazi // Journal of Materials Research and Technology. – 2021. – Vol. 12. – P. 234–242. https://doi.org/10.1016/j.jmrt.2021.02.075

4. Dilatometric analysis of the austenite

DOI 10.15588/1607-3274-2026-1-4

decomposition in undeformed and deformed low-carbon structural steel [Text] / M. Morawiec, A. Skowronek, M. Król, A. Grajcar // Materials. – 2020. – Vol. 13, No. 23. – Art. 5443. https://doi.org/10.3390/ma13235443

5. Bharadwaj, R. Effect of cooling rate on phase transformation kinetics and microstructure of Nb–Ti microalloyed low carbon HSLA steel [Text] / R. Bharadwaj, A. Sarkar, B. Rakshe // Metallography, Microstructure, and Analysis. – 2022. – Vol. 11. – P. 661–672. https://doi.org/10.1007/s13632-022-00864-9

6. Study of the influence of accelerated cooling on the kinetics of destruction of low-carbon low-alloy steels [Text] / O. V. Beketov, D. V. Laukhin, M. M. Osypchuk, A. R. Pomazan, O. V. Radko // Ukrainian Journal of Civil Engineering and Architecture. – 2025. – No. 1. – P. 17–24. https://doi.org/10.30838/UJCEA.2312.270225.17.1124

7. Mondal, J. Isothermal transformation kinetics, microstructure and mechanical properties of a carbide free bainitic steel [Text] / J. Mondal, K. Das, S. Das // Materials Characterization. – 2021. – Vol. 177. – Art. 111166. https://doi.org/10.1016/j.matchar.2021.111166

8. Effect of isothermal transformation temperature on the microstructure, precipitation behavior, and mechanical properties of anti-seismic rebar [Text] / J. Zhang, S. Gu, J. Wang, F. Wei, Z. Li, Z. Zeng, B. Shen, C. Li // High Temperature Materials and Processes. – 2024. – Vol. 43, No. 1. – Art. 20240028. https://doi.org/10.1515/htmp-2024-0028

9. A medium-C martensite steel with 2.6 GPa tensile strength and large ductility [Text] / J. Li, Z. Yang, H. Ma, C. Chen, F. Zhang // Scripta Materialia. – 2023. – Vol. 228. – Art. 115327. https://doi.org/10.1016/j.scriptamat.2023.115327

10. Singh, P. P. Strengthening behaviour and failure analysis of hot-rolled Nb+V microalloyed steel processed at various coiling temperatures [Text] / P. P. Singh, S. Ghosh, S. Mula // Materials Science and Engineering: A. – 2022. – Vol. 859. – Art. 144210. https://doi.org/10.1016/j.msea.2022.144210

11. Structural changes during thermal strengthening of the railway wheel [Text] / I. Vakulenko, S. Plitchenko, S. Gubarev, A. Khlebnikov // New Materials and Technologies in Metallurgy and Mechanical Engineering. – 2024. – No. 2. – P. 6–12. https://doi.org/10.15588/1607-6885-2024-2-11

12. Evolution of the microstructure and mechanical properties of a V-containing microalloyed steel during coiling [Text] / C. Gu, C. Scott, F. Fazeli, M. J. Gaudet, J. Su, X. Wang, N. Bassim, H. Zurob // Materials Science and Engineering: A. – 2023. – Vol. 880. – Art. 145332. https://doi.org/10.1016/j.msea.2023.145332

13. Analysis of temperature and stress fields in the process of hot-rolled strip coiling [Text] / M. Dai, Y. Hu, Y. Hao, P. Qiu, H. Xiao // Metals. – 2025. – Vol. 15, No. 2. – Art. 111. https://doi.org/10.3390/met15020111

14. Efficient finite element simulation of cold rolled strip coiling process considering additional contact deformation between layers [Text] / M. Dai, S. Liang, P. Qiu, H. Xiao // ISIJ International. – 2024. – Vol. 64. – P. 1037–1046. https://doi.org/10.2355/isijinternational.ISIJINT-2023-405

15. Wang, C. Structural transformation behavior of oxide scale during coiling of 0.9wt% Cr-containing high-strength steel [Text] / C. Wang, H. Wu, Y. Zhang // Journal of Materials Research and Technology. – 2024. – Vol. 30. – P. 840–853. https://doi.org/10.1016/j.jmrt.2024.03.094

16. Сухомлин Г. Д. Специальные границы в феррите низкоуглеродистых сталей [Текст] / Г. Д. Сухомлин // Металлофизика и новейшие технологии. – 2013. – Т. 35, № 9. – С. 1237–1249. Режим доступа: http://dspace.nbuv.gov.ua/bitstream/handle/123456789/104215/11-Sukhomlin.pdf?sequence=1

17. Influence structure on the plasticity of carbon steel of the railway wheel rim in operation [Text] / I. O. Vakulenko, L. I. Vakulenko, D. M. Bolotova, B. Kurt, H. Asgarov, O. Colova // Scientific Journal of Silesian University of Technology, Series Transport. – 2022. – Vol. 115. – P. 183–192. http://dx.doi.org/10.20858/sjsutst.2022.115.13

18. Tsuchida, N. Effect of ferrite grain size on the estimated true stress –strain relationship up to the plastic deformation limit in low carbon ferrite – cementite steels [Text] / N. Tsuchida, T. Inoue, H. Nakado // Journal of Materials Research. – 2013. – Vol. 28, No. 18. – P. 2171–2179. https://doi.org/10.1557/jmr.2013.221

19. Influence hot plastic deformation on the structure and properties of carbon steel of the railway wheel [Text] / I. Vakulenko, S. Plitchenko, D. Bolotova, Kh. Asgarov // Scientific Journal of Silesian University of Technology, Series Transport. – 2023. – Vol. 121. – P. 257–266. https://doi.org/10.20858/sjsutst.2023.121.16

20. Zhao, S. Formation of Widmanstätten ferrite and grain boundary ferrite in a hypereutectoid pearlitic steel [Text] / S. Zhao, N. Min, W. Li // Metals. – 2022. – Vol. 12, No. 3. – Art. 493. https://doi.org/10.3390/met12030493

21. Revealing the precipitation kinetics and strengthening mechanisms of a 450 MPa grade Nb-bearing HSLA steel [Text] / G. Liu, Y. Li, T. Liao, S. Wang, B. Lv, H. Guo, Y. Huang, Q. Yong, X. Mao // Materials Science and Engineering: A. – 2023. – Vol. 884. – Art. 145506. https://doi.org/10.1016/j.msea.2023.145506

22. Vakulenko, I. A. Influence degree and scheme of hot reduction on properties of the carbon steel [Text] / I. A. Vakulenko, S. Plitchenko, A. F. Yılmaz // Manufacturing Technologies and Applications. – 2025. – Vol. 6, No. 1. – P. 150–156. https://doi.org/10.52795/mateca.1634663.

23. New insight into the relationship between grain boundaries and hardness in bainitic/martensitic steels from the crystallographic perspective [Text] / J. Wang, H. Hong, A. Huang, X. Yang, R. Qian, C. Shang // Materials Letters. – 2022. – Vol. 308. – Art. 131105. https://doi.org/10.1016/j.matlet.2021.131105

DOI 10.15588/1607-3274-2026-1-4

p-ISSN 1607-6885 Нові матеріали і технології в металургії та машинобудуванні. 2026/1
e-ISSN 2786-7358 New materials and technologies in metallurgy and mechanical engineering. 2026/1

UDC 621.316.13

Daria Burova

PhD, Associate Professor of the Department of Materials Science and Advanced Technologies of the State Higher Educational Institution "Pryazovskyi State Technical University", Dnipro, Ukraine, *e-mail: burovadasha1990@gmail.com,* ORCID: 0009-0000-3460-8602

DETERMINATION OF THE INFLUENCE OF METASTABLE AUSTENITE IN THE SURFACE LAYER ON THE ABRASIVE WEAR RESISTANCE OF IRON-BASED ALLOYS

Purpose. *To consider and summarize the research results that show the influence of metastable austenite on the surface layer of steels in order to increase abrasive wear resistance. To demonstrate that in a number of cases, to enhance the specified characteristics in the structure of the surface layer of alloys, it is necessary to obtain metastable residual austenite alongside other components through various treatments. To present data showing that a self-hardening effect can be achieved under load, resulting in the formation of a renewable martensitic high-strength layer that provides protection against destruction. To present new data on the advantages of a differentiated approach to selecting the structure considering specific testing conditions or operational properties. Regarding these, it is necessary to optimize the quantity and stability of austenite in relation to the deformation martensitic transformation (DMT).*

Research methods. *Cemented steels 20Х, 18ХГ, 12Х13, 12ХН3А, and 12Х2Н4А, У8, ШХ15 were tested for abrasive wear resistance on the X4B installation. Abrasive wear tests were conducted on a setup designed according to the Brinell-Haworth scheme. The microstructure was studied on microsections prepared according to the generally accepted polishing and etching methodology. Metallographic and durometric studies were conducted. Cementation was carried out in a solid carburizer with additives that prevented surface oxidation.*

Results. *It has been established that to enhance the operational properties of cemented steels, it is necessary to utilize the self-hardening effect under load. It has been determined that the ambiguous assessments of the influence of residual austenite on the properties of cemented steels are due to the fact that the loading conditions, the amount, and the stability of austenite, which must be optimal for each specific case, are often not taken into account. It has been shown that in some cases it is advisable to ensure the formation of a large amount of metastable austenite after high-temperature treatment, and then, through deformation or (and) heat treatments, as well as other influences, to induce its partial transformation into martensite.*

Scientific novelty. *The work presents an alternative viewpoint, according to which, under dynamic loads, diffusion-alloyed steels should create a metastable austenite sublayer by means of the diffusion layer's absorption. To obtain wear-resistant thermodiffusion layers of significant thickness, it is advisable to create a structure of white chromium-manganese cast irons with metastable austenite. The effective use of concentrated energy sources for strengthening cemented steels ensures high surface hardness and the necessary amount of metastable austenite in the structure. Furthermore, this allows the creation of a discrete structure that alternates in a specified sequence between hard and soft components, significantly enhancing wear resistance.*

Practical value. *Increasing the mechanical properties of steels allows for greater operational stability of machine parts, which is an important task in materials science. One of the directions for solving this issue is to obtain a multiphase structure in steels, one component of which is metastable austenite, where dynamic deformation martensitic transformation (DDMT) occurs under load, resulting in the self-hardening effect under load (SHE). Methods for obtaining a surface layer structure of iron-based alloys, along with other components of metastable residual austenite, to enhance wear resistance under abrasive impact are easily implementable in production conditions. A differentiated approach to selecting the structure, taking into account specific testing or operational conditions, is necessary.*

Key words: *metastable austenite, self-hardening effect under load, dynamic deformation martensitic transformation (DDMT), cementation, strengthening.*

Introduction

Cementation and subsequent heat treatment are widely used in industry to increase the hardness, wear resistance, contact endurance, and other properties of steels. It is generally accepted that the surface layer of cemented steels should have a structure of tempered high-carbon martensite and carbides. The amount of residual austenite should not exceed 10–15 %. At some plants, a higher amount of austenite is considered a sign of defect. To reduce or completely eliminate the residual austenite in the structure, various methods are used: subcooling during quenching from cementation heating, cold treatment, intermediate high tempering followed by quenching from the

DOI 10.15588/1607-3274-2026-1-5

intercritical temperature range, and others [1]. Meanwhile, there are known works [2–14] that demonstrate the positive influence of residual austenite obtained in the surface layer and the effect of self-hardening under load (SHUL) on wear resistance and fatigue strength. However, these works are few, and until now, in educational literature and practice, residual austenite is considered an undesirable structure. This is a consequence of the insufficient study of the conditions under which residual austenite is beneficial. In this regard, there is an interest in summarizing the research results on this issue, which is the focus of this work.

Analysis of research and publications

Let's first consider the influence of residual austenite on abrasive wear resistance. The study [2] shows that during tests of cemented steels 20Х, 18ХГ, 12Х13, 12ХН3А, and 12Х2Н4А on the Х4Б installation, abrasive wear resistance increases with the increase in the content of residual austenite to levels that reduce hardness by almost 2 times. A pattern is observed, explained by the fact that during the impact of abrasive particles, austenite transforms into thermodynamically more stable martensite. At this point, the carbon remains in solid solution, determining its increased resistance to destruction. It has been established [3] that in cemented steel 20Х, hardened from an elevated temperature (1080 °C), when approximately 3 7% of austenite transforms into martensite under abrasive impact, wear resistance is at a high level. It differs little from the level in high-alloy steel Х12Ф1, which has a martensitic-carbide structure after heat treatment. The influence of residual austenite on the abrasive wear resistance of steels 18ХГ and 12ХН3А was studied in [4]. It was shown that the highest wear resistance is achieved when the surface layer structure is predominantly austenitic (80 %). This is achieved by hardening from the carburizing heating without cooling, as well as from reheating at 1000 °C (tempering at 180 °C for 1 hour). In this case, the increase in deformation martensite on the worn surface is the largest (40 %). Based on the obtained data, it was concluded that to increase the resistance to abrasive wear of cemented steels, heat treatment should not be aimed at achieving high hardness, which is provided by a martensitic-carbide structure, but at realizing the self-hardening effect under load due to the formation of metastable austenite and abrasive particles in the surface layer. Depending on the loading conditions, austenite can be obtained alongside martensite and carbides [5]. The necessary amount of metastable austenite alongside martensite and carbides, ensuring high wear resistance can be achieved in low-carbon high-chromium stainless steels through surface carburizing and subsequent heat treatment. This is demonstrated on steel 12Х13 [6].

The purpose of the work

Consider and summarize the results of studies that show the influence of metastable austenite on the surface layer of steels in order to enhance abrasive wear resistance. It should be demonstrated that in a number of cases, to improve the specified characteristics in the structure of the surface layer of alloys, metastable residual austenite should be obtained alongside with other components through various treatments. Provide data showing that a self-hardening effect can be achieved under load, resulting in the formation of a renewable martensitic high-strength layer that provides protection against destruction. Present new data on the advantages of a differentiated approach to selecting the structure, taking into account specific testing conditions or operational properties. In relation to them, the quantity and stability of austenite should be optimized concerning the deformation martensitic transformation (DMT).

Materials and research methodology

Cemented steels 20Х, 18ХГ, 12Х13, 12ХН3А, and 12Х2Н4А, У8, ШХ15 were tested for abrasive wear resistance on the Х4Б installation. Tests for abrasive wear were conducted on a setup designed according to the Brinell-Hauworth scheme. The scheme of the testing installation is shown in Fig. 1.

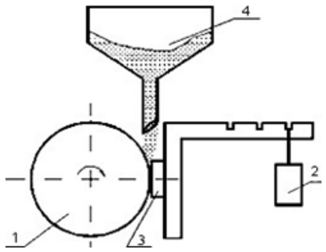

Figure 1. Scheme of abrasive wear testing:

1 – roller; 2 – weight; 3 – sample; 4 – hopper with abrasive

The rubber disk (1), which rotates, presses the sample (3) sized 25×10×10 mm with the weight (2). Through a funnel with a calibrated opening from the hopper (4), the abrasive (sea sand) is fed, which is captured by the rubber disk and drawn across the surface of the sample, causing its wear. A sample made of steel 45 (hardness HV220) was used as a reference. The tests were conducted for 30 minutes (with weighing the samples every 5 minutes of wear).

Tests for impact-abrasive wear were conducted according to the scheme presented in Fig. 2.

The samples were fixed on a disk that rotated at a speed of 1350 rpm. Impact-abrasive wear of the surface of the samples occurred due to collisions with particles of cast iron shot (0.8 mm) that fall freely. The samples were weighed with an accuracy of up to 0.01 g. Wear (I) was evaluated by the weight loss relative to the area of the samples using the equation: $I = P/S$, where P is the weight loss, kg; S is the area of the sample, m². The relative wear resistance (ε) was determined as the ratio of the indicators of the sample (I_sample) to the reference (I_reference) using the equation: $\varepsilon = I\_sample / I\_reference$.

DOI 10.15588/1607-3274-2026-1-5

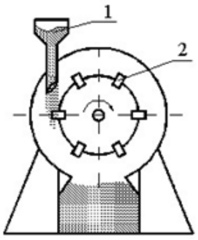

Figure 2. Scheme of impact-abrasive wear tests:
1 – hopper with shot; 2 – samples

Hardness was determined by the Rockwell method according to DST 9013-59 (indentation with a diamond pyramid under a load of 1500 N). Hardness was defined as the average of three measurements.

The microstructure was studied on microsections, which were made according to the generally accepted polishing and etching methodology.

Metallographic studies were conducted using an optical microscope “Neophot-21” and an electron microscope “JEM-100CX-11” (by the method of transmission of thin foil).

To determine the phase composition, an X-ray diffractometer DRON-4 was used.

Cementation was carried out in a solid carburizer with additives that prevented surface oxidation. The cementation temperature was 930 °C, and the depth of the carbon layer was 0.7 mm.

Diffusion chromizing was carried out by a gas contact method in a powder mixture of ferrochrome, aluminum oxide, and ammonium chloride at a temperature of 1050° C for 10 hours. The chromized samples were heated in the range of 850–1000 °C and held for 20 to 240 minutes. Metallographic and durometric studies showed that there is a certain heating regime for diffusion-chromized steels before hardening, which allows obtaining a white sublayer that is not etched and has a microhardness of H100 > 9000 MPa.

Research results

A promising direction is the development of methods for strengthening cemented (nitrocemented) steels, in which, unlike those traditionally used in industry, it is proposed to obtain a certain amount of metastable austenite in the structure of the surface layer and its subsequent transformation into martensite under load during the wear process [14–19]. According to the method [18], alloyed steels are subjected to nitrocementation to obtain an austenitic structure in the surface layer, after which strengthening is carried out using means of strain hardening or dispersion hardening. As a result, high hardness of 60–62 HRC is achieved without the use of quenching, which eliminates warping of the parts. At the same time, favorable compressive stresses are created. However, this work does not consider the possibility of using the deformation martensitic transformation of austenite under subsequent loading during the wear process. This is implemented in a method that includes conducting thermochemical treatment, plastic deformation (δ) with a degree of 40 % at elevated temperatures to obtain metastable austenite in the structure. It is proposed [20] that after obtaining a large amount of metastable austenite, a deformation or thermal effect should be applied in such a way that, along with strengthening the austenite and transitioning part of it into martensite, it would be preserved in the structure to a certain amount. This ensures the occurrence of DDMT during the loading in the operation of parts and tools, and, accordingly, increases their durability. The amount and degree of stability of the austenite remaining after processing must be regulated concerning specific operating conditions. It is proposed [16] to obtain a differentiated (discrete) structure in the surface layer of cemented steels with alternating martensitic and austenitic areas. This can be implemented by quenching with laser, electron beams, or plasma jets in specified local areas. This ensures a regular alternation of areas of high and low hardness.

Usually, the microstructure of the surface after cementation consists of pearlite and carbides, while the core consists of martensite and ferrite. After quenching from 900 °C and low tempering (200 °C), the surface structure contains tempered martensite, carbides, and a small amount of residual austenite. As the heating temperature during quenching increases to 1000–1100 °C, the hardness of the cemented surface decreases due to the complete dissolution of carbides in austenite and an increase of the amount of residual austenite (table 1).

Table 1 – The influence of heating temperature during hardening on the hardness and amount of residual austenite in the surface layer structure of carburized steel 12X13

Temperature, °C	Hardness, HRC	$\gamma_{residual}$, %
900	59,3	12
1000	49,0	17
1100	45,0	25

A similar effect is achieved by conducting local chemical-thermal treatment and hardening. The macro-heterogeneous structure significantly increases resistance to destruction during operation, as softer areas with increased toughness prevent chipping due to the propagation of cracks that originate in regions of high hardness. Furthermore, the Sharpy principle can be realized, as the premature wear of local areas of low hardness-forming “pockets”-allows for better retention of lubrication and, consequently, greater durability of the components. The effect of such treatment is also due to a significant increase in microhardness from 6000–6500 MPa (after conventional heat treatment) to 8000–12300 MPa (after the application of laser and electron beam treatments), as well as the formation of metastable austenite, which undergoes DMT under load during operation. The authors of the work [20] showed that in the case of obtaining a predominantly austenitic

DOI 10.15588/1607-3274-2026-1-5

structure, laser and electron beam treatments under certain conditions cause the formation of martensite in the affected zone, which is due to the high levels of stress that arise. This allows for the management of the ratio of martensite to austenite in the structure of steels subjected to preliminary chemical-thermal treatment. Maximum wear resistance and contact fatigue occur when a concentrated heat source achieves 50–60 % residual austenite in the surface layer of steels and cast iron.

The increase in heating temperature during the hardening of cemented steel 12X13 from 900 to 1100 °C, despite a decrease in hardness, results in an increase in abrasive wear resistance by 1.5 times compared to the level achieved after hardening at 900 °C. This is due to DMT and dynamic aging. When determining the resistance to destruction under impact-abrasive wear, a different pattern is observed. Wear resistance changes according to a curve with a maximum at 1000 °C. The lowest level is observed in steel after hardening from 900 °C, when the structure of the surface layer is predominantly martensitic-carbide. This is due to the formation of microcracks in high-carbon martensite, which has increased brittleness. After hardening from 1000 °C, the wear resistance of cemented steel 12X13 increases by 1.35 times compared to the level achieved after hardening from 900 °C. Hardening from 1100°C already reduces wear resistance due to excessive stability and, accordingly, less development of DMT. The presented data confirm the position that it is possible to significantly enhance the properties of alloys by achieving optimal amounts and stability of austenite in the structure for specific loading conditions.

Obtaining austenite alongside with martensite in the surface layer and increasing resistance to dynamic loads is facilitated by the heat treatment of diffusion-chromated high-carbon steels, as a result of which there is a “dissolution” of the external carbide layer [10]. This has been demonstrated on steels У8 and ШХ15. For each heating temperature during hardening in the studied range, there is an optimal holding time that ensures the greatest strengthening of the sublayer and its magnitude. Figure 1 shows the microstructure of steel У8, in which the sublayer has been obtained.

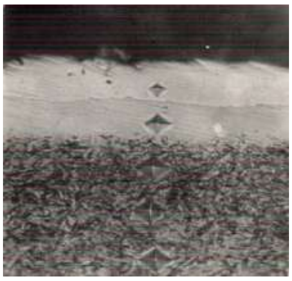

Figure 3. Microstructure of diffusion-chromized steel У8 after “dissolution” at 900 °C, 2 hours; ×500

The lowest of the studied tempering temperatures that allow for the necessary microhardness of the sublayer with acceptable holding time (1.5–2 hours) is 900 °C. At lower temperatures, it is not possible to obtain a solid sublayer in which no etching occurs within the specified time (1.5–2 hours), and at higher temperatures, the microhardness is not achieved. After hardening at 1000°C and low tempering, the microhardness of the sublayer is H = 6200–6500 MPa. At the same time, the grain of the base metal increases significantly. The highest level of resistance of the studied steels to impact and high contact loads is provided by diffusion chromizing at 900–920 °C with a holding time of 1.5–2 hours, followed by cooling to 800-820°C, hardening, and low tempering. The amount of residual austenite in the sublayer is 17–20 %. In this case, the wear resistance of diffusion-chromized steels increases by 1.5–2.0 times compared to the wear resistance obtained after conventional hardening and low tempering. The effectiveness of the proposed method was confirmed by operational tests of diffusion-chromized wedges in the binding systems of machines.

The method of strengthening discussed above can be applied when the permissible wear is relatively small (hundredths or tenths of a millimeter), which corresponds to the total thickness of the layer and sublayer obtained through diffusion chromizing and heat treatment. Moreover, the process of saturating the surface with chromium is lengthy, as it occurs in the solid phase – austenite. In this regard, [10] proposed and implemented a technology for obtaining thick diffusion layers, the structure of which corresponds to that of alloyed white cast irons. The basis of the technology is the principle that a shell of liquid phase is created on the surface of the treated part, in which the diffusion of alloying elements occurs, coming from a saturated medium. The liquid phase itself, enriched with the necessary elements, becomes a coating after crystallization. Since the diffusion process in the liquid phase occurs at a high speed, it is possible to alloy a layer several times thicker in a relatively short time than with the conventional saturation technology. To create a shell of liquid phase on the surface of the treated part, a metal or alloy containing the necessary components for the coating and having a lower melting point than the part and the saturating mixture is used. The temperature of diffusion alloying should be higher than the melting point of the low-melting alloy while keeping the part in a solid state. Numerous variants of the proposed technology can be implemented, as various heating methods, application of low-melting alloys, and different compositions of their saturating media are applicable. One of the simple methods for creating multi-component thermodiffusion layers of large thickness is the gas contact method using a saturating mixture containing ferroalloys, an inert additive, and a halide. Authors [21] studied the production of coatings from the a Fe-Cr-Mn-C system. The liquid phase during the process temperature was created by melting the filler elements placed on the surface of the steel sample. The filler elements were made from cast iron with a composition close to eutectic in the form of plates with a

DOI 10.15588/1607-3274-2026-1-5

diameter of 25 mm and a thickness of 4 mm. They were placed on the surface of the samples being strengthened, which were made of steel 45, and placed in a container with the saturating mixture. This container was sealed and placed in a furnace heated to 950–1000 °C. Then the temperature was raised to 1250–1280 °C and held for 0.5–1.5 hours. As a result of this treatment, wear-resistant chromium-manganese cast irons of various chemical compositions were obtained in the surface layer. The most successful were the diffusion coatings of the following composition: 2.5 %C, 12–15 % Cr, 4–7 % Mn. They had an austenitic-martensitic-carbide structure after heat treatment, which provided the highest abrasive wear resistance. These data became the basis for further development of chromium-manganese cast irons and filler materials with a similar structure [21]. The presented data demonstrate the great potential for obtaining surface layers through chemical-thermal and subsequent thermal treatment of multi-phase structures with metastable austenite.

Conclusions

It has been established that to enhance the operational properties of cemented steels, it is necessary to utilize the self-hardening effect under load. For this purpose, austenite capable of transforming into martensite under load should be obtained in the structure of the surface layer. The amount of austenite, the degree of its strengthening, and stability should be regulated by processing concerning specific loading conditions, taking into account the initial chemical and phase compositions of the steels obtained after heat treatment.

It has been determined that the ambiguous assessments of the influence of residual austenite on the properties of cemented steels are due to the fact that the loading conditions, the amount, and the stability of austenite, which must be optimal for each specific case, are often not taken into account.

It has been shown that in a number of cases, it is advisable to ensure the formation of a large amount of metastable austenite after heat treatment, and then, through deformation or (and) heat treatments, as well as other influences, to induce its partial transformation into martensite. At the same time, it is necessary to implement dynamic deformation martensitic transformation, which significantly enhances the service properties of the surface layer.

Under dynamic loads, diffusion-alloyed steels should create a substrate with metastable austenite due to the absorption of the diffusion layer.

To obtain wear-resistant thermodiffusion layers of significant thickness, it is advisable to create a structure of white chromium-manganese cast iron with metastable austenite.

The effective use of concentrated energy sources for strengthening cemented steels ensures high surface hardness and the necessary amount of metastable austenite in the structure. Moreover, this allows the creation of a discrete structure that alternates hard and soft components in a specified sequence, significantly enhancing wear resistance.

References

1. Dyachenko, S. S.,Doshchechkina, G. V., Movlyan, A. A., & Pleshakov,E. I. (2007). Material science (440). Khnadu Publishing House.

2. Malinov, L. S., Malinova, E. L., & Kharlanova, E. Ya. (1993). Increasing the abrasive wear resistance of cemented steels 18KHGT and 12KHN3A due to the production of metastable austenite. Metals, (2), 108–111.

3. Malinov, L.S., Malinov, V.L., Malysheva, I., & Burova, D.V. (2022). Principle Universality of Obtaining Metastable Austenite in the Alloy and Cast Iron Structure to Increase the Abrasive Wear Resistance. Journal of Friction and Wear, 43, 185–190. DOI: https://doi.org/10.3103/s1068366622030102

4. Malysheva, I. E. (2004). Increasing the abrasive and impact-abrasive wear resistance of steels and cast iron due to metastable austenite. Abstract of Candidate of Technical Sciences dissertation, Specialty 05.16.01 (19). Priazovskyi State Technical University.

5. Wang, W., Song, R., Peng, S., & Pei, Z. (2016). Multiphase steel with improved impact-abrasive wear resistance in comparison with conventional Hadfield steel. Materials & Design, 105, 96–105. DOI: https://doi.org/10.1016/J.MATDES.2016.05.056

6. Siepak, J. (1982). The influence of contact stress on the wear of a carburized steel case with a high content of retained austenite. Wear, 80, 301-305. DOI: https://doi.org/10.1016/0043-1648(82)90258-7

7. Efremenko, V.G., Zurnadzhi, V.I., Chabak, Y.G., Tsvetkova, O.V., & Dzherenova, A.V. (2017). Application of the Q-n-P-Treatment for Increasing the Wear Resistance of Low-Alloy Steel with 0.75% C. Materials Science, 53, 67-75. DOI: https://doi.org/10.1007/s11003-017-0045-3

8. Efremenko, V.G., Shimizu, K., Noguchi, T., Efremenko, A.V., & Chabak, Y.G. (2013). Impact–abrasive-corrosion wear of Fe-based alloys: Influence of microstructure and chemical composition upon wear resistance. Wear, 305, 155–165. DOI: https://doi.org/10.1016/J.WEAR.2013.06.006

9. Efremenko, V.G., Hesse, O., Friedrich, T., Kunert, M., Brykov, M.N., Shimizu, K., Zurnadzhy, V., & Suchmann, P. (2019). Two-body abrasion resistance of high-carbon high-silicon steel: Metastable austenite vs nanostructured bainite. Wear. 418–419, 24–35. DOI: https://doi.org/10.1016/J.WEAR.2018.11.003

10. Malinov, L. S.,& Malinov,V. L. (2009). Resource-saving economically alloyed alloys and hardening technologies that ensure the effect of self-hardening (568). Renata Publishing House.

11. Malinov, L.S., Malysheva, I., Klimov, E., Kukhar, V.V., & Balalayeva, E.Y. (2019). Effect of Particular

DOI 10.15588/1607-3274-2026-1-5

Combinations of Quenching, Tempering and Carburization on Abrasive Wear of Low-Carbon Manganese Steels with Metastable Austenite. Materials Science Forum, 945, 574–578. DOI: https://doi.org/10.4028/www.scientific.net/msf.945.574

12. Cheiliakh, Ya. A., Cheiliakh, A. P.,Shimmitsu, K.,& Noguchi, T. (2013). The use of chemical and thermal treatment to create metastable modifications that realize the effect of self-hardening during steel wear. Bulletin of the Azov State Technical University. Series: Technical Sciences, (27), 98–110.

13. Cheiliakh, A. P., Cheylyakh, Y. A., & Samotugina, Y. S. (2016). Strengthening technologies of materials treatment (337). KU Leuven.

14. Cheiliakh, O. P., Cheiliakh, Y. A., Karavaieva, N. E. et al. (2014). Development of innovative ways of surface hardening by means of creation of wear-resistant layers with metastable structure, strengthening at wear (part 1). Tratamientos Térmicos (Heat Treatment of Metals), (143), 35–36.

15. Cheiliakh, O. P., Cheiliakh, Y. A., Karavaieva, N. E., et al. (2014). Development of innovative ways of surface hardening by means of creation of wear-resistant layers with metastable structure, strengthening at wear (part 2). Tratamientos Térmicos (Heat Treatment of Metals), (144), 25–66.

16. Malinov, L.S. (1997). Obtaining a macroscopically nonuniform regular structure in steel by methods of differential treatment. Metal Science and Heat Treatment, 39, 139-143. DOI: https://doi.org/10.1007/BF02469067

17. Cheylyakh, Y., Cheiliakh, O.P., Mak-Mak, N.E., & Kazumichi, S. (2016). Effect of rising wear-resistance by plasma treatment of carburized structural steel. Vestnik of Nosov Magnitogorsk State Technical University, 14(2), 76–82. DOI: https://doi.org/10.18503/1995-2732-2016-14-2-76-82

18. Malinov, L.S., Malinov, V.L., & Burova, D.V. (2018). Impact of Metastable Austenite on the Wear Resistance of Tool Steel. Journal of Friction and Wear, 39, 349-353. DOI: https://doi.org/10.3103/S1068366618040098

19. Mak-Mak, N. E. (2019). Creation of metastable states and strengthening of structural steels by thermal and chemical-thermal treatment (24). Abstract of Candidate of Technical Sciences dissertation, Specialty 05.16.01. Priazovskyi State Technical University.

20. Malinov, L. S., & Malysheva, I. E. (2019). Abrasive wear resistance of alloys with metastable austenite (217). Priazovskyi State Technical University.

21. Malinov, L.S., Malinov, V.L., Burova, D.V., & Anichenkov, V.V. (2015). Increasing the abrasive wear resistance of low-alloy steel by obtaining residual metastable austenite in the structure. Journal of Friction and Wear, 36, 237–240. DOI: https://doi.org/10.3103/S1068366615030083

Received 19.01.2026
Accepted 02.02.2026
Published 31.03.2026

ВИЗНАЧЕННЯ ВПЛИВУ МЕТАСТАБІЛЬНОГО АУСТЕНІТУ В ПОВЕРХНЕВОМУ ШАРІ НА АБРАЗИВНУ ЗНОСОСТІЙКІСТЬ СПЛАВІВ НА ОСНОВІ ЗАЛІЗА

Дар'я Бурова

канд. техн. наук, доцент кафедри «Матеріалознавство і перспективні технології» ДВНЗ «Приазовський державний технічний університет», м. Дніпро, Україна, *e-mail: burovadasha1990@gmail.com*, ORCID: 0009-0000-3460-8602

Мета роботи. *Розглянути і узагальнити результати досліджень, які показують вплив метастабільного аустеніту на поверхневий шар сталей для того, щоб підвищіти абразивну зносостійкость. Показати, що в ряді випадків для підвищення зазначених характеристик у структурі поверхневого шару сплавів слід за рахунок різних обробок отримувати поряд з іншими складовими метастабільний залишковий аустеніт. Привести дані, які показують, що можна отримати ефект самозагартування при навантаженні, в результаті зовнішнього впливу відбувається утворення поновлюваного мартенситного високоміцного шару, що забезпечує захист від руйнування. Представити нові данні о перевагах диференційованого підходу до вибору структури з урахуванням конкретних умов випробувань властивостей чи експлуатації. Стосовно них слід оптимізувати кількість та стабільність аустеніту по відношенню до деформаційного мартенситного перетворення (ДМП).*

Методи дослідження. *Цементовані сталі 20Х, 18ХГ, 12Х13, 12ХН3А, та 12Х2Н4А, У8, ШХ15 випробовували на абразивну зносостійкість на установці Х4Б. Випробування на абразивне зношування проводили на установці, яку сконструювали за схемою Брінеля-Хауорта. Мікроструктуру вивчали на мікрошліфах, які виготовляли по загальноприйнятій методиці полірування і травлення. Були проведені металографічні та дюрометрічні дослідження. Цементацію проводили у твердому карбюризаторі з добавками, що запобігали окисленню поверхні.*

Отримані результати. *Встановлено, що для підвищення експлуатаційних властивостей цементованих сталей необхідно використовувати ефект самозагартування при навантаженні. Визначено, що неоднозначні*

DOI 10.15588/1607-3274-2026-1-5

оцінки впливу залишкового аустеніту на властивості цементованих сталей обумовлені тим, що часто не враховуються умови навантаження, кількість та стабільність аустеніту, які мають бути оптимальними для кожного конкретного випадку. Було показано, що доцільно в ряді випадків забезпечити отримання після ХТО великої кількості метастабільного аустеніту, а потім за допомогою деформації або (і) термообробок, а також інших впливів викликати його часткове перетворення на мартенсит.

Наукова новизна. *У роботі розглядається альтернативна точка зору, згідно з якою при динамічних навантаженнях дифузійнолегованих сталей слід створювати за рахунок розсмоктування дифузійного шару підшар із метастабільним аустеніт. Для отримання зносостійких термодифузійних шарів великої товщини доцільно створювати структуру білих хромомарганцевих чавунів із метастабільним аустенітом. Ефективне для зміцнення цементованих сталей використання джерел концентрованої енергії, що забезпечує високу твердість поверхні та отримання необхідної кількості метастабільного аустеніту у структурі. Крім того, це дозволяє створювати дискретну структуру, що є чергуванням в заданій послідовності твердих і м'яких складових і істотно підвищити зносостійкість.*

Практична цінність. *Підвищення механічних властивостей сталей дозволяє збільшити експлуатаційну стійкість деталей машин, що є важливою задачею матеріалознавства. Одним із напрямків її вирішення є отримання в сталях багатофазної структури, однією зі складових якої є метастабільний аустеніт, в якому відбувається при навантаженні динамічне деформаційне мартенситне перетворення (ДДМП) ефект само гартування при навантаженні (СГН). Способи отримання в структурі поверхневого шару сплавів на залізній основі поряд з іншими складовими метастабільного залишкового аустеніту для підвищення зносостійкості при абразивному впливі легко реалізуються в умовах виробництва. Необхідно використати диференційований підхід до вибору структури з урахуванням конкретних умов випробувань властивостей чи експлуатації.*

Ключові слова: *метастабільний аустеніт, ефект самозагартування при навантаженні, динамічне деформаційне мартенситне перетворення (ДДМП), цементація, зміцнення.*

Список літератури

1. Матеріалознавство / С.С. Дьяченко, Г.В. Дощечкіна, А.О. Мовлян, Е.І. Плешаков. – Харьків : Видавництво ХНАДУ, 2007. – 440 с.

2. Малінов Л. С. Підвищення абразивної зносостікості цементованих сталей 18ХГТ і 12ХН3А за рахунок отримання метастабільного аустеніта / Л. С. Малінов, Е.Л. Малінова, Е.Я. Харланова // Метали. – 1993. – № 2. – С. 108–111.

3. Principle Universality of Obtaining Metastable Austenite in the Alloy and Cast Iron Structure to Increase the Abrasive Wear Resistance / L. S. Malinov, V. L. Malinov, I. E. Malysheva, D. V. Burova // Journal of Friction and Wear. – 2022. – Vol. 43, No. 3. – P. 185-190. – DOI: https://doi.org/10.3103/s1068366622030102

4. Малишева І. Є. Підвищення абразивної і ударно-абразивної зносостійкості сталей і чавунів за рахунок метастабільного : автореф. дис. на здобуття наук. ступеня канд. техн. наук : спец. 05.16.01 / Малишева Інна Юхимівна; Приазов. держ. техн. ун-т Маріуполь, 2004. – 19 с.

5. Multiphase steel with improved impact-abrasive wear resistance in comparison with conventional Hadfield steel / W. Wang, R. Song, S. Peng, Z. Pei // Materials & Design. – 2016. – Vol. 105. – P. 96–105. – DOI: https://doi.org/10.1016/j.matdes.2016.05.056

6. Siepak, J. The influence of contact stress on the wear of a carburized steel case with a high content of retained austenite / J. Siepak // Wear. – 1982. – Vol. 80, No. 3. – P. 301–305. – DOI: https://doi.org/10.1016/0043-1648(82)90258-7

7. Application of the Q-n-P-Treatment for Increasing the Wear Resistance of Low-Alloy Steel with 0.75% C / V. G. Efremenko, V. I. Zurnadzhi, Y. G. Chabak et al. // Materials Science. –2017. –Vol. 53. – № 1. – P.1-9. – DOI: https://doi.org/10.1007/s11003-017-0053-3

8. Impact-abrasive-corrosion wear of Fe-based alloys: Influence of microstructure and chemical composition upon wear resistance / V. G. Efremenko, A. V. Efremenko, Y. G. Chabak et al. // Wear. – 2013. – Vol. 305, No. 1–2. – P. 155–165. – DOI: https://doi.org/10.1016/j.wear.2013.06.006

9. Two-body abrasion resistance of high-carbon high-silicon steel: Metastable austenite vs nanostructured bainite / V. G. Efremenko, V. I. Zurnadzhy, O. Hesse et al. // Wear. – 2019. – Vol. 418–419. – P. 24–35. – DOI: https://doi.org/10.1016/j.wear.2018.11.003

10. Малінов Л. С. Ресурсосберігаючі економнолеговані сплави та зміцнюючі технології, які забезпечують ефект самозагартування/ Л. С. Малінов, В. Л. Малінов. – Маріуполь : Вид-во «Рената», 2009. – 568 с.

11. Effect of particular combinations of quenching, tempering and carburization on abrasive wear of low-carbon manganese steels with Metastable austenite / L. S. Malinov, I. E. Malysheva, V. V. Kukhar et al. // Materials Science Forum. 2019. – Vol. 945. – P. 574–578. – DOI: https://doi.org/10.4028/www.scientific.net/MSF.945.574

12. Використання хіміко-термічної обробки для створення метастабільних модифікацій, які реалізують ефект самозміцнення при зношуванні сталі / Я. А. Чейлях, А. П. Чейлях, К. Шиміцу, Т. Ногучи // Вестник Приазовского державного технічного університета. Серія: Технічні науки. – 2013. – № 27. – С. 98–110.

DOI 10.15588/1607-3274-2026-1-5

13. Cheiliakh A.P. Strengthening technologies of materials treatment / A. P. Cheiliakh, Y. A. Cheylyakh, Yu. S. Samotugina. – Leuven: KU Leuven (Belgium), 2016. – 337 p.

14. Development of innovative ways of surface hardening by means of creation of wear-resistant layers with metastable structure, strengthening at wear (part 1) / O.P. Cheiliakh, Y.A. Cheiliakh, N.E.Karavaieva et al. // Treatamientos Termicos (Heat Treatment of Metals). – Spain. – 2014. – № 143. – P. 35–36.

15. Development of innovative ways of surface hardening by means of creation of wear-resistant layers with metastable structure, strengthening at wear (part 2) / O.P. Cheiliakh, Y.A. Cheiliakh, N.E. Karavaieva [et al.] // Treatamientos Termicos (Heat Treatment of Metals). – Spain. – 2014. – № 144. – P. 25–26.

16. Malinov, L. S. Obtaining a macroscopically nonuniform regular structure in steel by methods of differential treatment / L. S. Malinov // Metal Science and Heat Treatment. – 1997. – Vol. 39, No. 3–4. – P. 139–143. – DOI: https://doi.org/10.1007/bf02469067

17. Effect of increased wear-resistance by the plasma treatment of carbonized structural steel / Y.A. Cheylyakh, O.P. Cheiliakh, N.E. Mak-Mak, Sh. Kazumichi // Vestnik of Nosov Magnitogorsk State Technical University. – 2016. – Vol. 14. – № 2. – P. 76–82. DOI: https://doi.org/10.18503/1995-2732-2016-14-2-76-82

18. Malinov, L. S. Impact of Metastable Austenite on the Wear Resistance of Tool Steel / L. S. Malinov, V. L. Malinov, D. V. Burova // Journal of Friction and Wear. 2018. – Vol. 39 (4). – P. 349–353. DOI: https://doi.org/10.3103/S1068366618040098

19. Мак-Мак Н. Є. Створення метастабільних станів та зміцнення конструкційних сталей способами термічної та хіміко-термічної обробки : автореф. дис. на здобуття наук. ступеня канд. техн. наук : спец. 05.16.01 /Мак-Мак Н. Є. – Маріуполь, 2019. – 24 с.

20. Малінов Л. С. Абразивна зносостійкість сплавів з метастабільним аустенітом / Малінов Л. С., Малишева И. Е. – Маріуполь : ПДТУ, 2019. – 217 с.

21. Increasing the abrasive wear resistance of low-alloy steel by obtaining residual metastable austenite in the structure / L. S. Malinov, V. L. Malinov, D. V. Burova, V. V. Anichenkov // Journal of Friction and Wear. – 2015. – Vol. 36, No. 3. – P. 237–240. – DOI: https://doi.org/10.3103/S1068366615030083

.

DOI 10.15588/1607-3274-2026-1-5

p-ISSN 1607-6885 Нові матеріали і технології в металургії та машинобудуванні. 2026/1
e-ISSN 2786-7358 New materials and technologies in metallurgy and mechanical engineering. 2026/1

МОДЕЛЮВАННЯ ПРОЦЕСІВ В МЕТАЛУРГІЇ ТА МАШИНОБУДУВАННІ

MODELING OF PROCESSES IN METALLURGY AND MECHANICAL ENGINEERING

UDC 621.941:004.85

APPLICATION OF MACHINE LEARNING METHODS FOR MODELING THE QUALITY AND STABILITY OF THE TURNING PROCESS

Oleksii Prykhodko	PhD, Associate Professor, Associate Professor of the Department of Applied Mathematic and Mechanic, Lutsk National Technical University, Lutsk, Ukraine, *e-mail: cdrr.mechanic@gmail.com*, ORCID: 0000-0001-8496-1295
Olha Babenko	PhD, Acting dean faculty of construction, architecture and design National University Zaporizhzhia Polytechnic, Zaporizhzhia, Ukraine, *e-mail: olyababenko15@gmail.com*, ORCID: 0000-0003-4020-0173

Purpose. *Development and validation of a predictive modeling methodology that enables multi-objective analysis of the turning process by simultaneously predicting two key parameters: average surface quality and process stability (variability).*

Research methods. *A comparative analysis of models based on Multiple Linear Regression (empirical formula) and the Random Forest algorithm was conducted. The models were trained on an open experimental dataset for $42CrMo_4$+QT steel. Accuracy was evaluated using R^2 and MAE metrics on a test set. Validation was performed on an independent dataset.*

Results. *The Random Forest model demonstrated slightly higher predictive capability for average roughness ($R^2=0.59$ vs. 0.53) and significantly higher capability for process stability ($R^2=0.139$ vs. negative values for the formula). The dominant influence of feed rate and tool nose radius on quality was established, as well as the key role of cutting speed and tool geometry on stability.*

Scientific movelty. *An approach for the simultaneous modeling of the quality and stability of the turning process is proposed. The substantial advantage of flexible ML models over classical regression for analyzing stochastic aspects of the process, such as process variability, has been quantitatively proven.*

***Practical** Value. The developed methodology serves as a tool for the multi-objective optimization of cutting parameters. Recommendations for improving process reliability have been formulated: increasing the depth of cut to enhance productivity, avoiding low-speed regimes ($v<95$m/min), and using a tool with a nose radius of $r=0.8$mm, which reduces the maximum expected process variability by more than 16%.*

***Key words**: machine learning, Random Forest algorithms, surface roughness, process stability, optimization, turning, multi-objective analysis.*

Introduction

Ensuring high surface quality and stable operation of turning processes is a key task in modern mechanical engineering. This issue is of particular importance in the production of critical components – aircraft engine elements, high-load shafts, axles, and hydraulic system parts – where even minor deviations in surface layer parameters can lead to a significant reduction in reliability, fatigue strength, or operational failure. Surface roughness parameters and process repeatability depend on a complex set of operational and structural factors, the interaction of which exhibits a pronounced non-linear character.

Classical approaches to selecting cutting parameters rely on empirical power laws and tabular recommendations. While these often provide an acceptable quality level, they fail to account for the complex non-linear interconnections and stochastic effects inherent in real-world cutting processes. Furthermore, such approaches are primarily focused on predicting the mean value of the roughness parameter and practically do not consider process variability, which is critically important in the context of increasing production stability.

The development of machine learning (ML) methods opens the possibility of transitioning from simplified analytical relationships to flexible models capable of reflecting the complex behavior of technological systems in a multidimensional parameter space. However, the challenge of applying them in metal machining remains open due to the limited amount of high-quality experimental data and the insufficiently studied ability of ML approaches to model not only the mean values of quality parameters but also their stability.

DOI 10.15588/1607-3274-2026-1-6

Therefore, there is a scientific and practical need to create a comprehensive predictive model capable of simultaneously predicting average surface quality and the stability of the turning process, taking into account non-linear interactions between technological parameters.

Analysis of Research and Publications

Modern research in surface roughness prediction for turning is characterized by a gradual transition from traditional empirical methods to the application of machine learning algorithms. Early works were largely based on constructing analytical dependencies of the mean value $\overline{R_a}$ on cutting parameters and tool geometry, primarily using power equations and response surface models. Although such approaches provided basic engineering interpretation, they demonstrated limited capability in describing the non-linear and interdependent effects inherent to the cutting process [1, 2].

Further progress in this field was driven by the implementation of machine learning methods capable of modeling multidimensional non-linear dependencies. Recent publications have employed Support Vector Machines (SVM), Random Forest, Gradient Boosting (XGBoost), Gaussian Process Regression (GPR), as well as deep neural networks and neuro-fuzzy systems. Most researchers indicate a significant advantage of ensemble and deep models over classical regression methods regarding $\overline{R_a}$ prediction accuracy, especially under conditions of limited and noisy experimental data [3–5]. Certain works demonstrate the potential of using GPR for tasks requiring not only point forecasts but also probabilistic uncertainty assessment, which is critical in production environments [1, 6].

An important research vector has been the integration into predictive models of informative features derived not only from process parameters but also from sensor signals – vibrations, acoustic emission, and drive current signals. The use of temporal and spectral characteristics allows for the effective identification of dynamic effects and process instability, particularly the onset of self-excited vibrations (chatter), which have a significant impact on surface microgeometry. Studies [7–9] have proven that the addition of vibration and acoustic features significantly improves the accuracy of both machining regime classification and roughness regression analysis.

Despite the intensive development of this topic, a critical review of the literature highlights a number of unresolved problems. Firstly, the vast majority of works focus on predicting the mean value $\overline{R_a}$, while variability indicators, specifically the standard deviation S_{Ra}, are practically not considered as independent modeling objects [10, 11]. This limits the possibilities for quantitative analysis of process stability and risk assessment of production fluctuations, although the consistency of quality indicators is often a decisive factor in industry. Secondly, many publications use relatively small experimental datasets on which models show high accuracy on test samples, but external validation of results is often absent [4, 12]. Consequently, the question of model generalization and scalability in real production conditions remains relevant. Thirdly, the degree of integration of such models into online monitoring systems remains insufficient to ensure automatic adjustment of parameters or early detection of deviations.

In this context, the scientific novelty and aim of this study are as follows. First, the work is aimed at modeling not only the mean roughness value $\overline{R_a}$ but also its variability S_{Ra}, which allows for filling one of the key gaps in modern research. Second, the choice of the Random Forest ensemble method is justified, providing the necessary balance between prediction accuracy and model interpretability, allowing for an assessment of the contribution of each factor to the formation of both mean and variable roughness indicators. The clarity of the model structure is a critical requirement for engineering practice [3, 4]. Third, conducting external validation on an independent dataset increases the reliability of the obtained results and confirms the robustness of the proposed approach across a wider range of conditions, which distinguishes this work from many previous studies. Finally, the formulated practical recommendations facilitate the transition from theoretical modeling to the optimization of technological processes in real production [13].

Thus, the analysis of the current state of the problem confirms both the relevance and feasibility of the chosen research direction: comprehensive modeling of mean and variable roughness characteristics using ensemble machine learning methods and ensuring external validation allows for expanding existing methodological approaches and creating a foundation for developing reliable prediction systems for turning quality.

Aim of the Study

The aim of this work is to develop and validate a predictive modeling methodology that ensures the simultaneous forecasting of two key characteristics of the turning process for $42CrMo_4$+QT steel:

- mean surface roughness ($\overline{R_a}$);
- process stability, defined by the standard deviation of roughness (S_{Ra}).

To achieve this aim, the following objectives must be met:

- form a representative experimental dataset;
- construct two models: an empirical power law formula (linear regression) and a Random Forest model;
- perform a comparative accuracy assessment using R^2 and MAE metrics;
- conduct an engineering interpretation of the influence of cutting factors on the target variables;
- validate the approach on an independent dataset;
- formulate recommendations for optimizing cutting parameters.

Material and Research Methodology

The study utilizes the open experimental dataset MaRoReS [14] for the turning of $42CrMo_4$+QT steel. The dataset contains the results of 68 independent experiments,

DOI 10.15588/1607-3274-2026-1-6

each accompanied by three parallel measurements of the roughness parameter R_a. The input data includes the main technological parameters of the turning process: v – cutting speed in the range of 76–200 m/min, f – feed rate (0.05–0.25 mm/rev), d – depth of cut (0.05–0.25 mm), and r – tool nose radius (0.4 or 0.8 mm). This structure ensures a representative factor space sufficient for building models to predict surface quality indicators and assess process stability based on machine learning methods.

Data preprocessing involved calculating integral characteristics for each experiment. The arithmetic mean of the roughness was defined as $\overline{R_a}$, and the standard deviation between the three measurements was defined as S_{Ra}, which was interpreted as a quantitative assessment of process stability (variability). Table 1 demonstrates the structure of the dataset using the first five rows as an example.

Table 1 – First 5 rows of the dataset

№	r	d	s	f	$\overline{R_a}$	S_{Ra}
0	0.4	0.05	138	0.15	0.857667	0.004726
1	0.4	0.05	138	0.15	1.078333	0.023629
2	0.4	0.10	107	0.10	0.408667	0.014012
3	0.4	0.10	107	0.10	0.558000	0.007810
4	0.4	0.10	107	0.20	1.133333	0.034819
5	0.4	0.10	107	0.20	1.185000	0.011358

In the first stage of modeling, an empirical power model was built based on multiple linear regression in logarithms. This approach yielded a formula of the form:

$$R_a = C \cdot r^a \cdot d^b \cdot v^c \cdot f^d, \qquad (1)$$

which reproduces the traditional form of the dependence of roughness on cutting parameters.

For comparison, a Random Forest Regressor model was also built with hyperparameter tuning using the GridSearchCV method. The data was split into training and test sets in a 75/25 ratio. An analysis of the importance of input parameters on the target roughness variable was also conducted.

Subsequent analysis focused on modeling process stability, represented by the S_{Ra} value. For this purpose, a Random Forest model was also applied, trained on the same four technological factors. The influence of critical cutting parameters on process stability and a comparison of stability for tools with different nose radii were also investigated.

The final stage was the external validation of the models on an independent dataset [15], which contains 20 experimental data points regarding the dependence of surface roughness on cutting regimes.

Research Results

Based on the power model (1), the following empirical formula was obtained to determine the mean roughness value:

$$R_a = 24.824 \cdot r^{-0.456} \cdot d^{-0.1811} \cdot v^{-0.5643} \cdot f^{0.7435}. \qquad (2)$$

Despite its simplicity and convenience, formula (2) demonstrated a somewhat limited capability in predicting the mean roughness value $\overline{R_a}$. On the test sample, the coefficient of determination was only $R^2 = 0.53$, indicating that the model explains only 53% of the data variability. The Mean Absolute Error (MAE) was 0.13μm. These results suggest a significant discrepancy between the linear model and the actual nature of parameter dependencies in cutting processes, as well as an inability to adequately reproduce interactions between them. This is consistent with the fact that the roughness formation process has a pronounced non-linear character, limiting the effectiveness of traditional regression formulas.

The application of the Random Forest model allowed for a slight improvement in prediction accuracy. On the test dataset, $R^2 = 0.59$ and MAE = 0.127μm were obtained. Figure 1 compares the predictions of both models with the actual experimental values on the test sample.

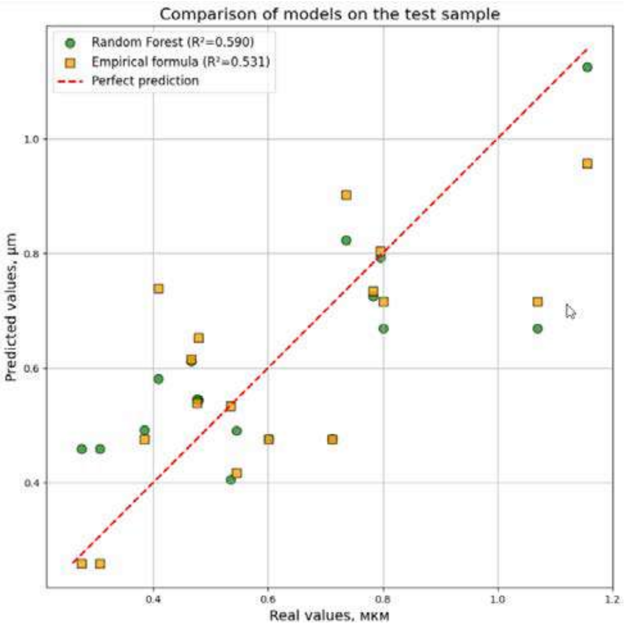

Figure 1. Comparison of predictions of the two models, $\overline{R_a}$

It can be seen that the points predicted by Random Forest cluster somewhat more tightly around the ideal prediction line (dashed line) than the points of the empirical formula.

Additionally, the importance of input parameters for the Random Forest model was analyzed (Fig. 2). The obtained values confirm the dominant influence of the feed rate f, which contributes the most to roughness variation. The tool nose radius r was the second most important factor, while the influence of the depth of cut d was the least significant. The cutting speed v manifested itself as a factor of medium significance.

DOI 10.15588/1607-3274-2026-1-6

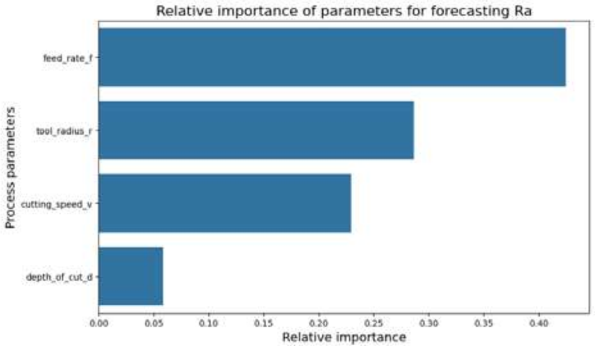

Figure 2. Feature importance for predicting $\overline{R_a}$

Process stability modeling, represented by the standard deviation of the roughness parameter S_{Ra}, was conducted separately. The results proved to be significantly less accurate compared to $\overline{R_a}$ prediction: for the Random Forest model, $R^2 = 0.139$ and MAE=0.0059µm were obtained. The empirical formula showed a negative value, indicating an inability to predict the data. The low value of the coefficient of determination is expected, as the variability of the S_{Ra} indicator is largely formed by stochastic factors (micro-vibrations, local microstructural differences, the initial state of the cutting edge, etc.) which are not represented in the dataset as input variables. The nature of the influence of the feed rate *f* on process stability is shown in Fig. 3.

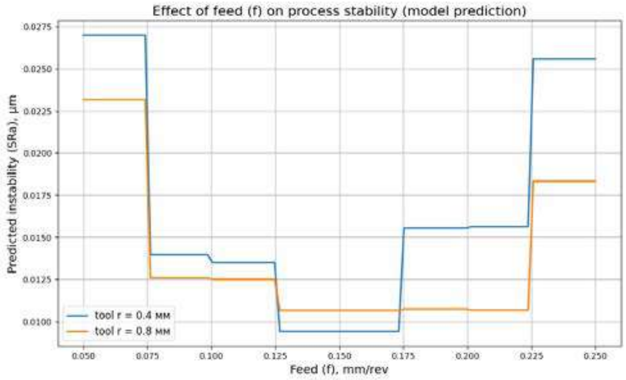

Figure 3. Influence of feed rate on S_{Ra}

An increase in S_{Ra} is observed with increasing feed, which corresponds to the complication of chip formation conditions and increased fluctuations in the load on the tool. The influence of cutting speed is shown in Fig. 4.

Here, an opposite trend is observed: stability deteriorates at low speeds, while increasing the cutting speed leads to a decrease in variability, corresponding to a more stable chip formation regime.

The influence of the tool nose radius on process stability is worth considering separately (Fig. 5).

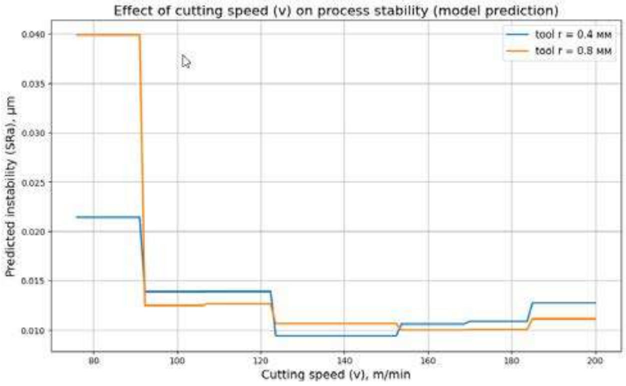

Figure 4. Influence of cutting speed on S_{Ra}

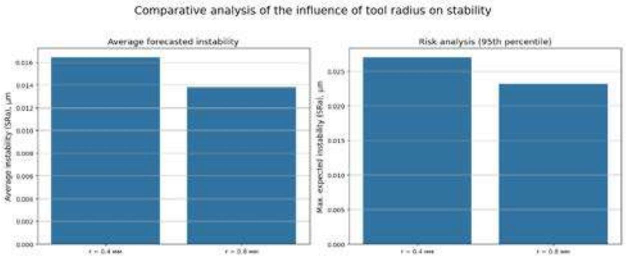

Figure 5. Comparison of S_{Ra} for r = 0.4 mm and r = 0.8 mm

The tool with a radius $r = 0.8$ mm showed significantly lower variability values than the tool with $r = 0.4$ mm, which can be explained by better load distribution and a reduction in local stress in the cutting zone. In particular, for certain combinations of regimes, a reduction in expected instability of more than 16 % is observed.

An important stage of the study was external validation on an independent set [15], which allowed for evaluating the generalizability of the constructed models. A comparison of the three approaches showed significant differences: the formula from [15] demonstrated a negative result ($R^2 \approx -0.675$), meaning it was unable to predicted the data. The modified power model obtained in this study showed a significantly more modest but non-zero consistency ($R^2 \approx 0.051$). The best result was provided by the Random Forest model with $R^2 \approx 0.525$, indicating its ability to transfer to other datasets without overfitting. A visual comparison of the three models relative to the ideal prediction is shown in Fig. 6.

As can be seen from Fig. 6, the points of the Random Forest model are located closest to the ideal prediction line, while the points of both empirical formulas are scattered across almost the entire range, indicating a complete inadequacy of prediction.

DOI 10.15588/1607-3274-2026-1-6

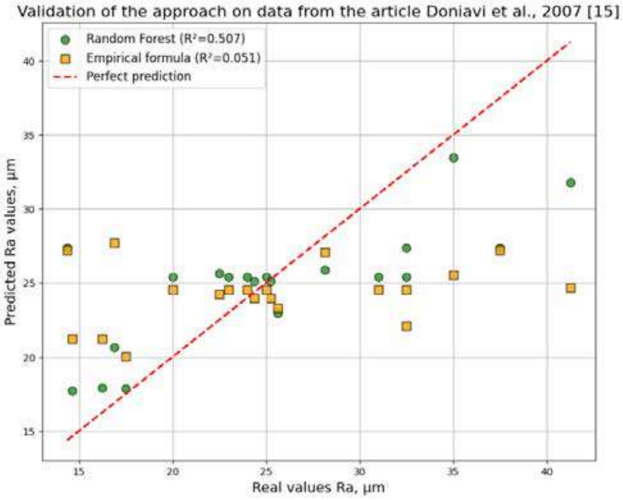

Figure 6. Comparison of predictions of three models on the external dataset [15]

Discussion

The obtained results confirm that classical power regression models, although providing a basic level of forecasting, are insufficiently flexible to describe the complex interrelationships between cutting process parameters. Machine learning models, particularly Random Forest, demonstrated a significantly higher capacity for generalization, especially under conditions of heterogeneous or noisy experimental data.

An important practical implication is the possibility of transitioning to multi-objective optimization, which simultaneously considers:

- low surface roughness;
- process stability and repeatability;
- productivity (via the possibility of increasing the depth of cut).

Stability analysis allowed for the identification of specific risk zones that are usually not revealed in works focusing solely on $\overline{R_a}$.

Conclusions

A methodology for predictive modeling of turning based on machine learning, which simultaneously forecasts process quality and stability, has been developed and validated.

The Random Forest algorithm provided significantly higher accuracy compared to classical regression.

It was established that the feed rate and tool nose geometry are the most influential factors on $\overline{R_a}$.

The first process stability model for S_{Ra} was built, allowing for the assessment of result repeatability.

Critical zones of instability were identified: low cutting speeds and extreme feed values.

A tool with a cutting edge radius of $r = 0.8$ mm ensures a tangible reduction in process variability (up to 16%) relative to tools with $r = 0.4$ mm.

Validation on an independent dataset confirmed the robustness of the machine learning approach.

References

1. Chen, J., Lin, J., Zhang, M., & Lin, Q. (2024). Predicting surface roughness in turning complex-structured work-pieces using vibration-signal-based Gaussian process regression. Sensors, 24(7), 2117. https://doi.org/10.3390/s24072117

2. Shan, X., et al. (2024). Experimental study and random forest machine learning of surface roughness for a typical laser powder bed fusion Al alloy. Metals, 14(10), 1148.

3. Guo, M. (2024). Prediction of surface roughness using deep learning and data-driven methods. Journal of In-telligent Manufacturing and Smart Engineering. https://doi.org/10.1108/JIMSE-10-2023-0010

4. Gadagi, A., et al. (2023). Machine learning approach to the prediction of surface roughness. Indian Journal of Engineering & Materials Sciences. https://doi.org/10.56042/ijems.v30i6.2182

5. M. P. Motta et al. Machine learning models for surface roughness monitoring in machining operations (2022). Procedia CIRP. 2022, 108, 710–715. URL: https://doi.org/10.1016/j.procir.2022.03.110.

6. Pawanr, S., & Gupta, K. (2025). Analysis of surface roughness and machine-learning-based modeling in dry turning of super duplex stainless steel using textured tools. Technologies, 13(6), 243. https://doi.org/10.3390/technologies13060243

7. Khasawneh F. A., Munch E., Perea J. A. (2018). Chatter Classification in Turning using Machine Learning and Topological Data Analysis. IFAC-PapersOnLine. 2018. Vol. 51, no. 14. P. 195–200. URL: https://doi.org/10.1016/j.ifacol.2018.07.222

8. Safeer, S. S., Sadique, A., & D, N. (2025). A machine learning approach for the prediction of surface roughness using the tool vibration data in turning operation. SAE Technical Paper 2025-28-0152. https://doi.org/10.4271/2025-28-0152

9. Farzad, W. (2025). Predicting quality of surface roughness and tool wear by vibration, sound and current signals in CNC turning (Technical report, DIVA-portal). https://www.diva-portal.org/smash/get/diva2:1960908/FULLTEXT01.pdf

10. Zhang, W. (2021). Surface roughness prediction with machine learning. Journal of Physics: Conference Series, 1856, 012040. https://doi.org/10.1088/1742-6596/1856/1/012040

11. Beemaraj, R. K., Chandra Sekar, M. S., & Vijayan, V. (2020). Computer vision measurement and optimiza-tion of surface roughness using soft computing approaches. Transactions of the Institute of Measurement and Control, 42(13), 2475–2481. https://doi.org/10.1177/0142331220916056

12. Canal, A. D., Regone, W., & Borille, A. V. (2025). Predictive modeling of surface roughness in machining pro-cesses using random forest regressor. The Journal of Engineering and Exact Sciences, 11(1), 22798. https://doi.org/10.18540/jcecvl11iss1pp22798

DOI 10.15588/1607-3274-2026-1-6

13. Ambhore, N., Naranje, V., & Shelke, S. (2025). Machining performance evaluation in turning of hardened steel using machine learning. Materials and Manufacturing Processes, 40(14), 1935–1942. https://doi.org/10.1080/10426914.2025.2559622

14. Díaz-Salamanca, D., Álvarez, Á., Muñiz Calvente, M., Ebrahimzadeh, P., Llavori, I., Zabala, A., … Papuga, J. (2024). MaRoReS (Machining, Roughness and Residual Stresses generated in turning of 42CrMo4+QT steel) (Version 1). Mendeley Data. https://doi.org/10.17632/z9w23xvhbt.1

15. Doniavi, A., Eskandarzade, M., & Tahmasebian, M. (2007). Empirical modeling of surface roughness in turn-ing process of 1060 steel using factorial design meth-odology. Journal of Applied Sciences, 7(17), 2509–2513. https://doi.org/10.3923/jas.2007.2509.2513

Received 25.12.2025
Accepted 07.01.2026
Published 31.03.2026

ЗАСТОСУВАННЯ МЕТОДІВ МАШИННОГО НАВЧАННЯ ДЛЯ МОДЕЛЮВАННЯ ЯКОСТІ ТА СТАБІЛЬНОСТІ ПРОЦЕСУ ТОКАРНОЇ ОБРОБКИ

Олексій Приходько — канд. техн. наук, доцент, доцент кафедри прикладної математики та механіки Луцького національного технічного університету, м. Луцьк, Україна, *e-mail: cdrr.mechanic@gmail.com*, ORCID: 0000-0001-8496-1295

Ольга Бабенко — канд. техн. наук, в.о. декана факультету будівництва, архітектури та дизайну Національного університету «Запорізька політехніка», м. Запоріжжя, Україна, *e-mail: olyababenko15@gmail.com*, ORCID: 0000-0003-4020-0173

Мета роботи. *Розробка та валідація методики предиктивного моделювання, що дозволяє проводити багатоцільовий аналіз технологічного процесу точіння шляхом одночасного прогнозування двох ключових параметрів: середньої якості поверхні та стабільності (варіабельності) процесу.*

Методи дослідження*. Порівняльний аналіз моделей на основі множинної лінійної регресії (емпірична формула) та алгоритму Random Forest. Моделі навчалися на відкритому наборі експериментальних даних для сталі* $42CrMo_4$*+QT. Точність оцінено за метриками* R^2 *та MAE на тестовій вибірці. Проведено валідацію на незалеж-ному наборі даних.*

Отримані результати*. Модель Random Forest продемонструвала дещо вищу прогностичну здатність для середньої шорсткості (*$R^2=0.59$ *проти 0.53) та особливо для стабільності процесу (*$R^2=0.139$ *проти негативних значень для формули). Встановлено домінуючий вплив подачі та радіуса інструменту на якість, а також ключову роль швидкості різання та геометрії інструменту на стабільність.*

Наукова новизна. *Запропоновано підхід до одночасного моделювання якості та стабільності процесу точіння. Кількісно доведено суттєву перевагу гнучких ML-моделей над класичною регресією для аналізу стохастичних аспектів процесу, таких як його варіабельність процесу токарної обробки.*

Практична цінність. *Розроблена методика є інструментом для багатоцільової оптимізації режимів різання. Сформульовано рекомендації для підвищення надійності процесу: збільшення глибини різання для підвищення продуктивності, уникнення низькошвидкісних режимів (*$v < 95$ *м/хв) та використання інструменту з радіусом* $r=0.8$ *мм, що знижує максимальну очікувану варіабельність процесу більш ніж на 16%.*

Ключові слова: *машинне навчання, алгоритм Random Forest, шорсткість поверхні, стабільність процесу, оптимізація, токарна обробка, багатоцільовий аналіз.*

Список літератури

1. Predicting Surface Roughness in Turning Complex-Structured Workpieces Using Vibration-Signal-Based Gaussian Process Regression / Chen J., Lin J., Zhang M., Lin Q. // Sensors. – 2024. – Vol. 24. – No. 7. – Article 2117. – https://doi.org/10.3390/s24072117

2. Experimental Study and Random Forest Machine Learning of Surface Roughness for a Typical Laser Powder Bed Fusion Al Alloy / Shan X. та ін. // Metals. – 2024. – Vol. 14. – No. 10. – Article 1148.

3. Guo M. Prediction of surface roughness using deep learning and data-driven methods // Journal of Intelligent Manufacturing and Smart Engineering. – 2024. – https://doi.org/10.1108/JIMSE-10-2023-0010

4. Machine Learning Approach to the Prediction of Surface Roughness / Gadagi A. та ін. // Indian Journal of Engineering & Materials Sciences. – 2023. – https://doi.org/10.56042/ijems.v30i6.2182

5. Machine learning models for surface roughness monitoring in machining operations / Motta M. P. та ін. // Procedia CIRP. – 2022. – https://doi.org/10.1016/j.procir.2022.03.110

DOI 10.15588/1607-3274-2026-1-6

6. Pawanr S. Analysis of Surface Roughness and Machine Learning-Based Modeling in Dry Turning of Super Duplex Stainless Steel Using Textured Tools / Pawanr S., Gupta K. // Technologies. – 2025. – Vol. 13.– No. 6. – Article 243. – https://doi.org/10.3390/technologies13060243

7. Khasawneh F. A. Chatter Classification in Turning using Machine Learning and Topological Data Analysis / Khasawneh F. A., Munch E., Perea J. A. // IFAC-PapersOnLine. – 2018. – Vol. 51. – No. 14. – P. 195–200. – https://doi.org/10.1016/j.ifacol.2018.07.222

8. Safeer S. S. A Machine Learning Approach for the Prediction of Surface Roughness Using the Tool Vibration Data in Turning Operation / Safeer S. S., Sadique A., D N. // SAE Technical Paper 2025-28-0152. – 2025. – https://doi.org/ 10.4271/2025-28-0152

9. Farzad W. Predicting Quality of Surface Roughness and Tool Wear by Vibration, Sound and Current Signals in CNC Turning / Farzad W. // техн. звіт (DIVA-portal). – 2025. – Режим доступу: https://www.diva-portal.org/smash/get/diva2:1960908/FULLTEXT01.pdf

10. Zhang Wenhe. Surface Roughness Prediction with Machine Learning // Journal of Physics: Conference Series. – 2021. – Vol. 1856. – Article 012040. – https://doi.org/10.1088/1742-6596/1856/1/012040

11. Beemaraj R. K. Computer vision measurement and optimization of surface roughness using soft computing approaches / Beemaraj R. K., Chandra Sekar M. S., Vijayan V. // Transactions of the Institute of Measurement and Control. – 2020. – Vol. 42 – P. 2475–2481. – https://doi.org/10.1177/0142331220916056

12. Canal A. D. Predictive Modeling of Surface Roughness in Machining Processes Using Random Forest Regressor / Canal A. D., Regone W., Borille A. V. // The Journal of Engineering and Exact Sciences. – 2025. – Vol. 11. – No. 1. – Article 22798. – https://doi.org/10.18540/jcecvl11iss1pp22798

13. Ambhore N.. Machining performance evaluation in turning of hardened steel using machine learning / Ambhore N., Naranje V., Shelke S. // Materials and Manufacturing Processes. – 2025. – Vol. 40, No. 14. – P. 1935–1942. – https://doi.org/10.1080/10426914.2025.2559622

14. MaRoReS (Machining, Roughness and Residual Stresses generated in turning of 42CrMo4+QT steel) / Díaz-Salamanca D. та ін.// Version 1. – Mendeley Data, 11 Apr 2024. – https://doi.org/10.17632/z9w23xvhbt.1

15. Doniavi A. Empirical Modeling of Surface Roughness in Turning Process of 1060 Steel Using Factorial Design Methodology / Doniavi A., Eskandarzade M., Tahmasebian M. // Journal of Applied Sciences. – 2007. – Vol. 7. – No. 17. – P. 2509–2513. – https://doi.org/10.3923/jas.2007.2509.2513

DOI 10.15588/1607-3274-2026-1-6

p-ISSN 1607-6885 Нові матеріали і технології в металургії та машинобудуванні. 2026/1
e-ISSN 2786-7358 New materials and technologies in metallurgy and mechanical engineering. 2026/1

UDC 539.3

Andriy Pozhuyev
Candidate of Physical and Mathematical Sciences, Professor, Professor of the Department of Fundamental and Applied Mathematics, Zaporizhzhia National University, Zaporizhzhia, Ukraine, *e-mail: scorpio6828@gmail.com,* ORCID: 0000-0002-4083-5139

Volodymyr Pozhuyev
Doctor of Physical and Mathematical Sciences, Professor, Professor of the Department of Theoretical and Applied Mechanics, Zaporizhzhia Polytechnic National University, Zaporizhzhia, Ukraine, *e-mail: pozhuevvi@gmail.com*, ORCID: 0000-0002-9163-7888

Olena Mikhailutsa
Candidate of Technical Sciences, Associate Professor, Associate Professor of the Department of Electronics, Information Systems and Software, Zaporizhzhia National University, Zaporizhia, Ukraine, *e-mail: elenamikhaylutsa7@gmail.com*, ORCID: 0000-0003-2935-7997

THE EFFECT OF A MOVING LOAD ON A THREE-LAYER CYLINDRICAL SHELL WITH A TRANSVERSAL ISOTROPIC FILLER

Purpose. *To extend the approach previously proposed by the authors on the application of exact equations of elasticity theory to problems of dynamics of three-layer cylindrical shells with isotropic filler to one of the possible cases of anisotropy of the middle layer material, namely the situation when the filler is transversely isotropic. To obtain accurate formulas and, based on them, to construct a picture of the stress-strain state in such a composite structure when moving along the outer surface at a constant normal (radial) load speed.*

Research methods. *A mathematical model of the dynamics of a three-layer cylindrical shell has been constructed, where the motion of the supporting layers is described by the equations of thin shell theory, and for a transversely isotropic filler, the dynamic equations of the theory of elasticity of an anisotropic medium in general form are used. When considering the problem in a stationary setting, Galilean transformation is applied, after which the integral Fourier transform in complex form is applied to all sought and given values in the moving coordinate system. To calculate non-proper Fourier integrals, quadrature formulas based on the Filon method for integrating rapidly oscillating functions were developed, which made it possible to efficiently obtain numerical results with a predetermined accuracy.*

Results. *Based on the constructed model, the problem of a moving load that causes a stationary stress-strain state of a layered cylindrical shell under various conditions on the surfaces of the joint between the filler and the supporting layers is considered. In this case, the contact is considered both rigid and sliding, but the lag of the shells from the filler is excluded. The difficulties that arise when solving the equations of motion of a transversely isotropic filler are overcome by introducing a special method using undefined coefficients of potential functions. For all possible boundary conditions, the results are obtained in the form of non-special improper integrals, which are calculated using special quadrature formulas. The distribution patterns of displacements and stresses along both the length and thickness of the filler are shown, a comparison with the results for the corresponding isotropic filler is made, and a mechanical analysis of the results is performed.*

Scientific novelty*. For the first time in such a formulation, when the behaviour of the filler is described by exact equations of the dynamics of an elastic anisotropic body, a solution to the stationary dynamic problem for a three-layer cylindrical shell has been obtained. A comparison was made with the results previously obtained for the case of isotropic filler. A special technique was used to introduce potential functions to find displacements and stresses in the dynamic equations for transversely isotropic materials. Important partial boundary conditions at the boundaries of layer contacts were considered.*

Practical value. *The results obtained with this approach can be used as reference values when constructing simplified models of the dynamic behaviour of three-layer cylindrical shells, in particular those that take into account the anisotropy of the filler. Examples of such materials include so-called ribbed sound-insulating materials.*

Key words*: layered shells, transversely isotropic medium, integral transformation, potential functions, boundary conditions, displacement, stress.*

Introduction

Dynamic problems for three-layer plates and shells are of considerable practical interest due to the fact that such structural elements are extremely widely used, in particular in aircraft and rocket construction, maritime transport, construction and other industries. At the same time, historically, at the beginning of the development of

DOI 10.15588/1607-3274-2026-1-7

the theory of such systems, various simplified approaches were proposed, based on hypotheses about the behaviour of a lighter and softer filler relative to the load-bearing layers, which made it possible to obtain equations for describing the behaviour of the entire three-layer package which were no more complex than similar equations for a single-layer shell or plate. It is clear that the models would be accurate if each of the layers obeyed (was described by) the dynamic equations of elasticity theory, but in this case, the calculation algorithm became much more complex and could not be used effectively enough in engineering calculations. Therefore, this approach is usually used for comparison with the results obtained using the simplified models mentioned above, and examples of solutions using the exact approach and the comparisons are given in monographs [1-4]. As numerous examples have shown, the most effective approach in terms of the complexity-accuracy ratio, especially in so-called stationary dynamic problems, is the one where the motion of the load-bearing layers (which are relatively very thin in relation to the thickness of the entire layered plate or shell) is described by the equations of the theory of single-layer shells, which are based on the Kirchhoff-Lyaev or Timoshenko hypotheses, and the dynamic equations of elasticity theory are used for the filler. In particular, monographs [1–2] present a large number of stationary and non-stationary problems considered in this formulation, comparisons with such solutions and with simplified approaches, but in all the problems presented, the filler was considered isotropic (homogeneous or with variable mechanical characteristics in thickness). This paper considers one of the problems of this class in order to show how the approaches previously developed by the authors can be extended to the case where the filler material has different properties depending on the direction, i.e. is significantly anisotropic, in particular in the case of a cylindrical three-layer shell, which is a transversely isotropic body.

Purpose of the work

A stationary dynamic problem is considered concerning the reaction of a three-layer infinitely long cylindrical shell to the movement of an axisymmetric radial load along its outer surface at a constant subcritical speed. The aim of the work is to extend the previously proposed approaches based on Galilean transformation, the application of integral transformations, and the use of numerical algorithms developed by the authors to reverse these transformations to the case of a transversely isotropic filler. At the same time, the main focus is on the analytical solution of dynamic equations for transversely isotropic filler material by introducing potential functions in a special way, which made it possible to obtain the transformants of displacements and stresses in the image space in the form of combinations of Bessel functions. The results obtained in this work can be used to construct simpler engineering models for shells with transversely isotropic fillers.

Material and research methods

An infinitely long three-layer cylindrical shell is considered, in the general case of an asymmetrical structure in terms of thickness, i.e., one in which the thickness and mechanical characteristics of the load-bearing layers may be different, and the filler, which is significantly lighter and softer than the shell materials, is transversely isotropic. A self-balanced radial load moves along the outer surface of the shell at a constant subcritical and pre-seismic velocity. It is necessary to determine the stress-strain state at arbitrary points of the load-bearing layers and filler and to evaluate the influence of the anisotropy of the filler material by comparing it with similar results for isotropic material.

The mathematical model of the problem is constructed as follows. We will describe the motion relative to thin load-bearing layers using the most well-known equations in shell theory and more accurate equations of the Timoshenko type, which, incidentally, do not follow from the equations of elasticity theory by simplification, but are an intuitive discovery of an outstanding Ukrainian mechanic, or by simpler equations based on Kirchhoff-Leva's hypotheses and derived from the equations of elasticity theory. In the first case, for the axisymmetric problem considered here, the equations of motion of the skins are written as follows [5, 11, 13]

$$\frac{\partial^2 u}{\partial x^2}+\frac{\nu_k}{a_k}\frac{\partial w}{\partial x}=\rho_k\frac{1-\nu_k}{2G_k}\frac{\partial^2 u}{\partial t^2}-\frac{1-\nu_k}{2G_k h_k}q_{xk}$$

$$\beta^2\left(\frac{\partial^2 w}{\partial x^2}-\frac{\partial \alpha}{\partial x}\right)-\frac{2}{1-\nu_k}\left(\frac{\nu_k}{a_k}\frac{\partial u}{\partial x}+\frac{w}{a_k^2}\right)=$$

$$=\rho_k\frac{1-\nu_k}{2G_k}\frac{\partial^2 w}{\partial t^2}-\frac{1-\nu_k}{2G_k h_k}\left(q_{rk}+p_k\right)$$

$$\beta^2\left(\frac{\partial w}{\partial x}-\alpha\right)+\frac{h_k^2}{6\left(1-\nu_k\right)}\frac{\partial^2 \alpha}{\partial x^2}=\rho_k\frac{h_k^2}{3G_k}\frac{\partial^2 \alpha}{\partial t^2}. \qquad (1)$$

Here, the index k = 1 refers to the inner load-bearing layer, and k = 2 refers to the outer layer, u, w are the displacements of the points of the middle surface of the corresponding shell in the axial and radial directions, α is the angle of rotation of the normal to the middle surface, Gk, ρk are the shear modulus and density of the materials of the corresponding shells, hk, ak are the thicknesses and radii of the middle surfaces of the load-bearing layers, β2 is the Timoshenko coefficient, qrk, qxk are the radial and axial reactions from the filler on the motion of the load-bearing layers , p1 = 0, p2 – intensity of external moving load.

For Kirchhoff-Lyaev equations, we will have the following [7, 10, 12]

$$\frac{\partial^2 u}{\partial x^2}+\frac{\nu_k}{a_k}\frac{\partial w}{\partial x}=\rho_k\frac{1-\nu_k}{2G_k}\frac{\partial^2 u}{\partial t^2}-\frac{1-\nu_k}{2G_k h_k}q_{xk},$$

$$\frac{\nu_k}{a_k}\frac{\partial u}{\partial x}+\frac{h_k^2}{12}\frac{\partial^4 w}{\partial x^4}+\frac{w}{a_k^2}=\rho_k\frac{1-\nu_k}{2G_k}\frac{\partial^2 w}{\partial t^2}-\frac{1-\nu_k}{2G_k h_k}\left(q_{rk}+p_k\right). \qquad (2)$$

DOI 10.15588/1607-3274-2026-1-7

Considering the filler to be transversely isotropic, we write the dependencies between stresses and strains in the general spatial case in the following form

$$\sigma_{xx} = c_{11}\varepsilon_{xx} + c_{12}\varepsilon_{yy} + c_{13}\varepsilon_{zz},$$
$$\sigma_{yy} = c_{12}\varepsilon_{xx} + c_{11}\varepsilon_{yy} + c_{13}\varepsilon_{zz},$$
$$\sigma_{zz} = c_{13}\left(\varepsilon_{xx} + \varepsilon_{yy}\right) + c_{33}\varepsilon_{zz},$$
$$\sigma_{xy} = \frac{1}{2}\left(c_{11} - c_{12}\right)\varepsilon_{xy}, \quad \sigma_{yz} = c_{44}\varepsilon_{yz}, \quad \sigma_{zx} = c_{44}\varepsilon_{zx}. \quad (3)$$

In practice, the following technical constants are usually used: E, E' – Young's moduli for tension – compression in the direction of the plane of isotropy and, respectively, in the direction normal to this plane, ν – Poisson's ratio, which characterises transverse compression in the plane of isotropy when stretched in this plane, ν' – the same characteristic when stretched in the direction normal to the plane of isotropy, G = E / 2(1+ν), G' = E' / 2(1+ν') – shear moduli for the plane of isotropy and any plane perpendicular to it.

In this case, we obtain the necessary dependencies for further use in an obvious way [6]

$$c_{11} = \frac{E\left(E' - \nu'^2 E\right)}{\left(1+\nu\right)\left[\left(1-\nu\right)E' - 2\nu'^2 E\right]},$$
$$c_{12} = \frac{E\left(\nu E' + \nu'^2 E\right)}{\left(1+\nu\right)\left[\left(1-\nu\right)E' - 2\nu'^2 E\right]},$$
$$c_{13} = \frac{\nu' E E'}{\left(1-\nu\right)E' - 2\nu'^2 E},$$
$$c_{33} = \frac{\left(1-\nu\right)E'^2}{\left(1-\nu\right)E' - 2\nu'^2 E}, \quad c_{44} = G'. \quad (4)$$

First, we write down the dynamic equations of elasticity theory in stresses for the filler, which in a cylindrical coordinate system and for an axisymmetric problem have the following form [15]

$$\frac{\partial \sigma_{xx}}{\partial x} + \frac{\partial \sigma_{rx}}{\partial r} + \frac{1}{r}\sigma_{rx} = \rho\frac{\partial^2 u_x}{\partial t^2},$$
$$\frac{\partial \sigma_{rr}}{\partial r} + \frac{\partial \sigma_{rx}}{\partial x} + \frac{1}{r}\left(\sigma_{rr} - \sigma_{\theta\theta}\right) = \rho\frac{\partial^2 u_r}{\partial t^2}. \quad (5)$$

and then, rewriting the dependencies (3) in a cylindrical coordinate system and using the Cauchy relations according to which

$$\varepsilon_{rr} = \frac{\partial u_r}{\partial r}, \quad \varepsilon_{xx} = \frac{\partial u_x}{\partial x}, \quad \varepsilon_{\theta\theta} = \frac{u_r}{r}, \quad (6)$$
$$\varepsilon_{xr} = \frac{\partial u_r}{\partial x} + \frac{\partial u_x}{\partial r},$$

we arrive at the equations of motion of a transverse isotropic filler in displacements

$$c_{11}\frac{\partial}{\partial r}\left(\frac{\partial u_r}{\partial r} + \frac{u_r}{r}\right) + c_{44}\frac{\partial^2 u_r}{\partial x^2} + \left(c_{13} + c_{44}\right)\frac{\partial^2 u_x}{\partial r \partial x} = \rho\frac{\partial^2 u_r}{\partial t^2}$$
$$c_{44}\frac{1}{r}\frac{\partial}{\partial r}\left(r\frac{\partial u_x}{\partial r}\right) + c_{33}\frac{\partial^2 u_x}{\partial x^2} + $$
$$+\left(c_{13} + c_{44}\right)\frac{\partial}{\partial x}\left(\frac{\partial u_r}{\partial r} + \frac{u_r}{r}\right) = \rho\frac{\partial^2 u_x}{\partial t^2}. \quad (7)$$

Due to the fact that the thicknesses of the bearing layers are relatively small, it is assumed that the filler contacts each of the shells along their middle surfaces, and then the boundary conditions for the system of partial differential equations (7) are written as follows:

if the contact is considered to be sliding but lagging is excluded, then

$$r = a_k \quad \sigma_{rx} = 0, u_r = w, \sigma_{rr} = \begin{cases} -q_{r1}\left(r = a_1\right) \\ q_{r2}\left(r = a_2\right) \end{cases}. \quad (8)$$

considering the contact to be rigid, the boundary conditions are written as follows

at $r = a_k$ $u_r = w, u_x = u, \sigma_{rx} = -q_{xk}, \sigma_{rr} = \begin{cases} -q_{r1}\left(r = a_1\right) \\ q_{r2}\left(r = a_2\right) \end{cases}$. (9)

Note that since the problem is considered in the so-called steady-state formulation, there are no initial conditions for the system (7).

Since in this problem the load moves along the shell at a constant speed *c*, we apply Galilean transformation to all equations of the problem, according to which a moving coordinate system is introduced by the formulas

$$r' = r, \quad \eta = \frac{x - ct}{a_2}. \quad (10)$$

Now, in the coordinate system according to (10), the stress-strain state of our structure remains unchanged over time (the values do not depend on the variable *t*), but changes when the load velocity *c* changes.

Let us move to the moving coordinate system in equations (1), (2) and (7) according to formulas (10), then instead of (1) and (2) we will have ordinary differential equations with variable η, and (7) will become equations in partial derivatives with variables η and *r* = r'

$$\nu_k\frac{a_2}{a_k}\frac{dw}{d\eta} + \left(1 - \frac{\rho_k c^2}{2G_k}\left(1-\nu_k\right)\right)\frac{d^2 u}{d\eta^2} = -\frac{\left(1-\nu_k\right)a_2}{2G_k h_k}q_{xk},$$
$$\left(\beta^2 - \frac{\rho_k c^2}{2G_k}\left(1-\nu_k\right)\right)\frac{d^2 w}{d\eta^2} - \frac{2}{1-\nu_k}\left(\frac{\nu_k}{a_k}\frac{du}{d\eta} + \frac{w}{a_k}\right) - $$
$$-\beta^2 a_2\frac{d\alpha}{d\eta} = -\frac{\left(1-\nu_k\right)a_2}{2G_k h_k}\left(q_{rk} + p_k\right),$$
$$\beta^2\left(\frac{1}{a_2}\frac{dw}{d\eta} - \alpha\right) + \frac{h_k^2}{a_2^2}\left(\frac{1}{6\left(1-\nu_k\right)} - \frac{\rho_k c^2}{3G_k}\right)\frac{d^2\alpha}{d\eta^2} = 0. \quad (11)$$

DOI 10.15588/1607-3274-2026-1-7

System (2) takes the following form

$$\left(1-\frac{(1-\nu_k)\rho_k c^2}{2G_k}\right)\frac{d^2u}{d\eta^2}+\nu_k\frac{a_2}{a_k}\frac{dw}{d\eta}=-\frac{(1-\nu_k)a_2}{2G_k h_k}q_{xk}$$

$$\begin{gathered}\nu_k\frac{a_2}{a_k}\frac{du}{d\eta}+\frac{h_k^2}{12a_2^2}\frac{d^4w}{d\eta^4}+\frac{wa_2}{a_k}-\frac{(1-\nu_k)\rho_k c^2}{2G_k}\frac{d^2w}{d\eta^2}= \\ =-\frac{(1-\nu_k)a_2}{2G_k h_k}(q_{rk}+p_k)\end{gathered}\ . \quad (12)$$

The equation of motion of a transverse isotropic filler in a moving coordinate system is written as follows

$$\begin{gathered}c_{11}\frac{\partial}{\partial r}\left(\frac{\partial u_r}{\partial r}+\frac{u_r}{r}\right)+\frac{1}{a_2^2}\left(c_{44}-\rho c^2\right)\frac{\partial^2u_r}{\partial\eta^2}+ \\ +\frac{1}{a}(c_{13}+c_{44})\frac{\partial^2u_x}{\partial r\partial\eta}=0 \\ c_{44}\frac{1}{r}\frac{\partial}{\partial r}\left(r\frac{\partial u_x}{\partial\eta}\right)+\frac{1}{a_2^2}\left(c_{33}-\rho c^2\right)\frac{\partial^2u_x}{\partial\eta^2}+ \\ +\frac{1}{a}(c_{13}+c_{44})\frac{\partial}{\partial\eta}\left(\frac{\partial u_r}{\partial r}+\frac{u_r}{r}\right)=0\end{gathered}\ . \quad (13)$$

Since the functions *u*, *w*, α, u_x , u_r together with their derivatives tend to zero at $|\eta|\to\infty$, then we apply to equations (11)–(13) and boundary conditions (8), (9) a complex integral Fourier transform with respect to the variable η

$$\overline{w}=\int_{-\infty}^{+\infty}we^{-i\xi\eta}d\eta,\quad w=\frac{1}{2\pi}\int_{-\infty}^{+\infty}\overline{w}e^{i\xi\eta}d\xi\ . \quad (14)$$

Then, in the image space, instead of (11) and (12) we will have systems of algebraic equations, and instead of (13) we will have a system of ordinary differential equations with respect to the transformants of the sought quantities

$$\begin{gathered}i\xi\frac{a_2}{a_k}\nu_k\overline{w}-\left(1-\frac{\rho_k c^2}{2G_k}(1-\nu_k)\right)\xi^2\overline{u}=-\frac{(1-\nu_k)a_2}{2G_k h_k}\overline{q}_{xk} \\ -\left(\beta^2-\frac{\rho_k c^2}{2G_k}(1-\nu_k)\right)\xi^2\overline{w}-\frac{2}{1-\nu_k}\left(i\xi\frac{\nu_k}{a_k}\overline{u}+\frac{\overline{w}}{a_k}\right)- \\ -i\xi\beta^2a_2\overline{\alpha}=-\frac{(1-\nu_k)a_2}{2G_k h_k}(\overline{q}_{rk}+\overline{p}_k) \\ \beta^2\left(i\xi\frac{\overline{w}}{a_2}-\overline{\alpha}\right)-\frac{h_k^2}{a_2^2}\xi^2\left(\frac{1}{6(1-\nu_k)}-\frac{\rho_k c^2}{3G_k}\right)\overline{\alpha}=0\ . \quad (15)\end{gathered}$$

Equation (12) in the image space looks like this

$$\begin{gathered}i\xi\nu_k\frac{a_2}{a_k}\overline{u}+\frac{h_k^2}{12a_2^2}\xi^4\overline{w}+\frac{a_2}{a_k}\overline{w}+\frac{(1-\nu_k)\rho_k c^2}{2G_k}\xi^2\overline{w}= \\ =-\frac{(1-\nu_k)a_2}{2G_k h_k}(\overline{q}_{rk}+\overline{p}_k)\end{gathered}\ ,$$

$$-\left(1-\frac{(1-\nu_k)\rho_k c^2}{2G_k}\right)\xi^2\overline{u}+i\xi\nu_k\frac{a_2}{a_k}\overline{w}=-\frac{(1-\nu_k)a_2}{2G_k h_k}\overline{q}_{xk}\ . \quad (16)$$

Before translating system (13) into the image space, it is advisable to introduce potential functions according to the following formulas

$$\begin{gathered}u_r=\frac{\partial}{\partial r}(\varphi+\psi), \\ u_x=\frac{1}{a_2}\frac{\partial}{\partial\eta}(k_1\varphi+k_2\psi).\end{gathered} \quad (17)$$

If we substitute expressions (17) into system (13), we obtain the following partial derivative equations for determining functions φ and ψ

$$\left(\frac{\partial^2}{\partial r^2}+\frac{1}{r}\frac{\partial}{\partial r}+\frac{x_1}{a_2^2}\frac{\partial^2}{\partial\eta^2}\right)\varphi=0\ .$$

$$\left(\frac{\partial^2}{\partial r^2}+\frac{1}{r}\frac{\partial}{\partial r}+\frac{x_2}{a_2^2}\frac{\partial^2}{\partial\eta^2}\right)\psi=0\ . \quad (18)$$

where x_1 , x_2 are roots of the following quadratic equation that are not equal to each other

$$\begin{gathered}c_{11}c_{44}x^2-\left[\left(c_{44}-\rho c^2\right)c_{44}+\left(c_{33}-\rho c^2\right)c_{11}-(c_{13}+c_{44})^2\right]x+ \\ +\left(c_{33}-\rho c^2\right)\left(c_{44}-\rho c^2\right)=0\end{gathered}\ . \quad (19)$$

and the unknown constants k_1 and k_2 are determined from the following relation

$$k(c_{13}+c_{44})+\left(c_{44}-\rho c^2\right)=c_{11}x\ . \quad (20)$$

Note that in the case of an isotropic body, when the following conditions are satisfied *E* = *E'*, ν = ν', *G* = *G'* equations (19) and (20) take the following form

$$x^2-\left(m^2+m_s^2\right)x+m^2m_s^2=0\ . \quad (21)$$

$$k=2(1-\nu)x-(1-2\nu)m_s^2\ . \quad (22)$$

Here

$$m^2=1-\frac{c^2}{c_p^2},\quad m_s^2=1-\frac{c^2}{c_s^2},$$

where c_p, c_s are the propagation velocities of tensile-compressive and shear waves in an isotropic medium

$$c_p=\sqrt{\frac{2G(1-\nu)}{\rho(1-2\nu)}},\quad c_s=\sqrt{\frac{G}{\rho}}\ .$$

DOI 10.15588/1607-3274-2026-1-7

From equations (21) and (22), we find $x_1 = m^2$, $x_2 = m_s^2$, $k_1 = 1$, $k_2 = m_s^2$ and formula (18) becomes wave equations for an isotropic body.

The expressions for the components of the stress state of a transversely isotropic filler through potential functions, which are necessary for further calculations, are written as follows

$$\frac{\sigma_{rr}}{c_{44}} = -\frac{\beta + k_1}{a_2^2}\frac{\partial^2 \varphi}{\partial \eta^2} - \frac{\beta + k_2}{a_2^2}\frac{\partial^2 \psi}{\partial \eta^2} - \frac{c_{11} - c_{12}}{c_{44}}\frac{1}{r}\frac{\partial}{\partial r}(\varphi + \psi)$$

$$\frac{\sigma_{rx}}{c_{44}} = \frac{1 + k_1}{a_2}\frac{\partial^2 \varphi}{\partial r \partial \eta} + \frac{1 + k_2}{a_2}\frac{\partial^2 \psi}{\partial r \partial \eta}, \quad \beta = 1 - \frac{\rho c^2}{c_{44}}. \tag{23}$$

In the image space, equations (18) take the following form

$$\frac{d^2\overline{\varphi}}{dr^2} + \frac{1}{r}\frac{d\overline{\varphi}}{dr} - \frac{x_1 \xi^2}{a_2^2}\overline{\varphi} = 0,$$

$$\frac{d^2\overline{\psi}}{dr^2} + \frac{1}{r}\frac{d\overline{\psi}}{dr} - \frac{x_2 \xi^2}{a_2^2}\overline{\psi} = 0. \tag{24}$$

Each of the equations (24) is a Bessel equation, the solutions of which, depending on the values of x_1 and $x_{(2)}$,will be Bessel functions of various kinds. In particular, for load velocities that are less than the velocity of shear waves in the corresponding isotropic medium and less than the critical velocity, the roots x_1 and x_2 of equation (19) are real and positive numbers. Then the solutions of equations (24) take the following form

$$\overline{\varphi}(r,\xi) = A_1 K_0\left(\frac{e_1 \xi r}{a_2}\right) + A_2 I_0\left(\frac{e_1 \xi r}{a_2}\right),$$

$$\overline{\psi}(r,\xi) = A_3 K_0\left(\frac{e_2 \xi r}{a_2}\right) + A_4 I_0\left(\frac{e_2 \xi r}{a_2}\right), \tag{25}$$

where $e_1 = \sqrt{x_1}$, $e_2 = \sqrt{x_2}$, $I_n(x)$, $K_n(x)$ are Bessel functions of the first and second kind from the imaginary argument [14].

Applying the Fourier transform to formulas (17) and (23), and then substituting expressions (25) into the transformed formulas, we find the transforms of displacements and stresses at all points of a transversely isotropic filler, in particular, we will have the following formulas

$$\overline{u}_r = -\frac{\xi}{a_2}\left[e_1 K_1(e_1 \xi r_*)A_1 + e_1 I_1(e_1 \xi r_*)A_2 + e_2 K_1(e_2 \xi r_*)A_3 + \right.$$
$$\left. + e_2 I_1(e_2 \xi r_*)A_4\right], \quad r_* = \frac{r}{a_2},$$

$$\frac{\overline{\sigma}_{rr}}{c_{44}} = \frac{\xi^2}{a_2^2}\left[(\beta + k_1)K_0(e_1 \xi r_*)A_1 + (\beta + k_1)I_0(e_1 \xi r_*)A_2 + \right.$$

$$\left. + (\beta + k_2)K_0(e_2 \xi r_*)A_3 + (\beta + k_2)I_0(e_2 \xi r_*)A_4\right] +$$

$$+ \frac{c_{11} - c_{12}}{c_{44}}\frac{\xi}{r_* a_2}\left[e_1 K_1(e_1 \xi r_*)A_1 + e_1 I_1(e_1 \xi r_*)A_2 + \right.$$
$$\left. + e_2 K_1(e_2 \xi r_*)A_3 + e_1 I_1(e_2 \xi r_*)A_4\right]. \tag{26}$$

In the image space of equations (15) and (16), which are systems of algebraic equations, we use them to obtain dependencies between the transformants of loads transmitted to the outer and inner surfaces of the filler, and the displacements of the shells, which, according to conditions (8) and (9), coincide with the displacements at the boundaries of the filler. At the same time, if the contact between the skins and the filler is considered to be sliding, then in (15) and (16) we must set $\overline{q}_{xk} = 0$ and express $\overline{q}_{rk}$ only through $\overline{w}$. If, however, the contact is considered to be rigid, then $\overline{q}_{xk}$ and $\overline{q}_{rk}$ are found to be dependent simultaneously on $\overline{w}$ and $\overline{u}$. Based on these considerations, we find that in the case of a rigid contact with system (16), the above dependencies are written as follows

$$\overline{q}_{xk} = \frac{2G_k}{1 - \nu_k}\chi_k^2\left[\left(1 - \frac{1 - \nu_k}{3}c_{0k}^2\right)\xi^2 \overline{u} - i\xi \nu_k \varphi(k)\overline{w}\right]$$

$$\overline{q}_{rk} = -\overline{p}_k - \frac{2G_k}{1 - \nu_k}\chi_k^2\left[\left(\frac{\chi_k^2 \xi^4}{12} + \varphi^2(k) - \frac{1 - \nu_k}{3}c_{0k}^2 \xi^2\right)\overline{w} + \right.$$
$$\left. + i\xi \nu_k \varphi(k)\overline{u}\right] \tag{27}$$

and in the case of sliding contact, we have the following

$$\overline{q}_{rk} = -\overline{p}_k - \frac{2G_k}{1 - \nu_k}\chi_k^2\left[\frac{\chi_k^2 \xi^4}{12} + \varphi^2(k)\left(1 - \frac{3\nu_k^2}{3 - (1 - \nu_k)c_{0k}^2}\right) - \right.$$
$$\left. - \frac{1 - \nu_k}{3}c_{0k}^2 \xi^2\right]\overline{w}. \tag{28}$$

where the following designations are introduced

$$\varphi(k) = \begin{cases} \dfrac{1}{\varepsilon_1} & (k = 1) \\ 1 & (k = 2) \end{cases}, \quad \varepsilon_1 = 1 - \chi(1 + \chi_s),$$

$$\chi = \frac{h_2}{a_2}, \quad \chi_s = \frac{a_2 - a_1}{h_2} \quad c_0 = \sqrt{\frac{3\rho}{2G}} \cdot c.$$

The formulas for these dependencies have a similar form when using equations (15), but first we must exclude $\overline{\alpha}$ from the second and third equations and deal with a system similar to system (16).

If we now substitute expressions (27)–(28), as well as formulas of the form (26) for the transforms of displacements and stresses in the boundary conditions (18) or (19) recorded using the integral Fourier transform, we obtain a system of algebraic equations for determining the

DOI 10.15588/1607-3274-2026-1-7

functions $A_1(\xi) \div A_4(\xi)$, the solution of which by Cramer's method will be written as follows

$$A_1 = \frac{1}{G}\frac{a_2^2 A_{41}}{\xi K_1(e_1\xi)\,det\|a_{ij}\|},\ A_2 = -\frac{1}{G}\frac{a_2^2 A_{42}}{\xi I_1(e_1\xi)\,det\|a_{ij}\|}$$

$$A_3 = -\frac{i}{G}\frac{a_2^2 A_{43}}{e_2\xi^2 K_1(e_2\xi)\,det\|a_{ij}\|},$$

$$A_4 = \frac{i}{G}\frac{a_2^2 A_{44}}{e_2\xi^2 I_1(e_2\xi)\,det\|a_{ij}\|}, \tag{29}$$

where the elements of the determinant $det\|a_{ij}\|$ in the case of sliding contact are calculated using the following formulas

$$a_{11} = 2e_1 s_1,\ a_{12} = -2e_1 s_4,\ a_{13} = n_1 s_7,\ a_{14} = n_1 s_{10}$$
$$a_{21} = 2e_1,\ a_{22} = -2e_1,\ a_{23} = n_1,\ a_{24} = n_1,$$
$$a_{31} = n_1\xi s_2 + 2e_1 t_1 s_1,\ a_{32} = n_1\xi s_5 - 2e_1 t_1 s_4, \tag{30}$$
$$a_{33} = 2(e_2\xi s_8 + t_1 s_7),\ a_{34} = -2(e_2\xi s_{11} - t_1 s_{10}),$$
$$a_{41} = n_1\xi s_3 + 2e_1 t_2,\ a_{42} = n_1\xi s_6 - 2e_1 t_2,$$
$$a_{43} = 2(e_2\xi s_{10} + t_2),\ a_{44} = -2(e_2\xi s_{12} - t_2),$$
$$n_1 = 1 + e_2^2,\ n_2 = \frac{\chi\gamma}{1-\nu},$$
$$t_1 = 1/\varepsilon_1,\ t_2 = 1 - n_2 n_4,$$
$$\gamma = \frac{G_2}{G_1},\ \rho^* = \frac{\rho_2}{\rho},$$
$$n_3 = \frac{\chi^2\xi^4}{12} + \frac{1}{\varepsilon_1^2}\left(1 - \frac{3\nu_k^2}{(1-\nu_k)c_0^2}\right) - \frac{1-\nu_k}{3}c_0^2\xi^2,$$
$$s_1 = \frac{K_1(e_1\xi\varepsilon_1)}{K_1(e_1\xi)},\ s_2 = \frac{K_0(e_1\xi\varepsilon_1)}{K_1(e_1\xi)},\quad s_3 = \frac{K_0(e_1\xi)}{K_1(e_1\xi)},$$

s_4– s_6 are obtained from s_1– $s_3$by replacing the functions $K_n(x)$ with the functions $I_n(x)$, s_7– $s_9$from s_1– s_3, and s_{10}– s_{12} from s_4 – s_6 by replacing e_1 with e_2 , n_4 is found from n_3 when ε_1 = 1, and A_{4j} – minors of elements.

In the case of rigid contact (9), the functions A_k are calculated using formulas (29), if $det\|a_{ij}\|$ is replaced with $det\|b_{ij}\|$, A_{4j} with B_{4j} , and the elements of the determinants are found using the following formulas

$$b_{11} = 2e_1(1-n_8)s_1 - t_3 s_2,\ b_{12} = -2e_1(1-n_8)s_4 - t_3 s_5,$$
$$b_{13} = (n_1 - 2n_8)s_7 - t_4 s_8,\ b_{14} = (n_1 - 2n_8)s_{10} + t_4 s_{11},$$
$$b_{21} = 2e_1(1-\nu n_2) - t_3 s_3,\ b_{22} = -2e_1(1-\nu n_2) - t_3 s_6,$$
$$b_{23} = n_1 - 2\nu n_2 - t_4 s_9,\qquad b_{24} = n_1 - 2\nu n_2 + t_4 s_{12}$$
$$b_{31} = 2e_1 n_9 s_1 + \xi(n_1 + 2n_8)s_2$$
$$b_{32} = -2e_1 n_9 s_4 + \xi(n_1 + 2n_8)s_5$$
$$b_{33} = 2n_9 s_7 + 2e_2\xi(1+n_8)s_8,$$
$$b_{34} = 2n_9 s_{10} - 2e_2\xi(1+n_8)s_{11},$$
$$b_{41} = 2e_1 n_{10} + \xi(n_1 - 2\nu n_2)s_3,$$
$$b_{42} = -2e_1 n_{10} + \xi(n_1 - 2\nu n_2)s_6,$$
$$b_{43} = 2n_{10} + 2e_2\xi(1-\nu n_2)s_9,$$
$$b_{44} = 2n_{10} - 2e_2\xi(1-\nu n_2)s_{12},$$
$$n_5 = \frac{\chi^2\xi^4}{12} + \frac{1}{\varepsilon_1^2} - \frac{1-\nu}{3}c_0^2\xi^2,$$
$$n_7 = 1 - \frac{1-\nu}{3}c_0^2,\ n_8 = \frac{\nu}{\varepsilon_1}n_2,$$
$$n_9 = \frac{1}{\varepsilon_1} + n_2 n_5\ \ n_{10} = 1 - n_2 n_6$$
$$t_3 = 2n_2 n_7,$$

where n_6 is obtained from n_5 at ε_1 = 1.

After finding $A_1 \div A_4$ using formulas (29), we find the transformants of displacements and stresses using expressions (26). As a result, we arrive at the following dependencies

$$\frac{\bar{u}_r}{h_2} = -\frac{v(\xi, r_*)}{\chi G\,det\|a_{ij}\|}, \tag{32}$$

$$v(\xi, r_*) = e_1 s_{14} A_{41} + e_2 s_{16} A_{42} + s_{18} A_{43} - s_{20} A_{44}, \tag{33}$$

$$\bar{\sigma}_{rr} = \frac{\varepsilon(\xi, r_*)}{det\|a_{ij}\|}, \tag{34}$$

$$\varepsilon(\xi, r_*) = \left(n_1\xi s_{13} + \frac{2e_1}{r_*}s_{14}\right)A_{41} - \left(n_1\xi s_{16} - \frac{2e_1}{r_*}s_{16}\right)A_{42} +$$
$$+ 2\left(e_2\xi s_{17} + \frac{1}{r_*}s_{18}\right)A_{43} + 2\left(e_2\xi s_{19} - \frac{1}{r_*}s_{20}\right)A_{44}, \tag{35}$$

$$s_{13} = \frac{K_0(e_1\xi r_*)}{K_1(e_1\xi)},\ s_{14} = \frac{K_1(e_1\xi r_*)}{K_1(e_1\xi)},\quad r_* = \frac{r}{a_2},$$

s_{15} – s_{16} are obtained from s_{13} – s_{14} by replacing the functions K_n with the functions I_n , s_{17} – s_{18} from s_{13} – s_{14}, and s_{19} – s_{20} from s_{15} – s_{16} by replacing e_1 with e_2.

As an example, calculations are performed for a ring load moving along the outer shell at a speed *of c*

$$p(x,t) = p_0\delta(x - ct), \tag{36}$$

where δ (x) is the Dirac delta function.

After applying the inverse Fourier transform in the space of originals, we obtain the following improper integrals for finding displacements and stresses at arbitrary points of a three-layer shell

$$\frac{2Gu_r}{p_0} = -\frac{2\gamma}{\pi}\int_0^\infty \frac{v(\xi, r_*)cos(\xi\eta)}{det\|a_{ij}\|}d\xi, \tag{37}$$

$$\frac{\sigma_{rr}a_2}{p_0} = \frac{1}{\pi}\int_0^\infty \frac{\varepsilon(\xi, r_*)cos(\xi\eta)}{det\|a_{ij}\|}d\xi. \tag{38}$$

DOI 10.15588/1607-3274-2026-1-7

From the results obtained, we can obtain solutions for some boundary cases. In particular, if we assume that the inner surface of the filler does not contact the supporting layer, we obtain a problem about a shell with a hollow filler on the inner surface of which there are no stresses, then at $r = a_1$, we have the following boundary conditions

$$\sigma_{rr} = 0, \quad \sigma_{rx} = 0. \tag{39}$$

The solution is given by formulas (37) and (38) if some elements of the determinant are replaced as follows

$$a_{31} = n_1 \xi s_2 + 2e_1 \frac{s_1}{\varepsilon_1}, \quad a_{32} = n_1 \xi s_5 - 2e_1 \frac{s_4}{\varepsilon_1},$$
$$a_{33} = 2\left(e_2 \xi s_8 + \frac{s_7}{\varepsilon_1} \right), \quad a_{34} = -2\left(e_2 \xi s_{11} - \frac{s_{10}}{\varepsilon_1} \right). \tag{40}$$

Under conditions (39) and rigid contact between the outer shell and the filler in formulas (31), taking into account (40), the following substitutions must be made

$$b_{1j} = a_{1j}, \quad b_{3j} = a_{3j} \quad (j = 1, \ ,4). \tag{41}$$

All other elements of the determinants $det\left\| a_{ij} \right\|$ and $det\left\| b_{ij} \right\|$ remain unchanged.

If the inner shell is considered to be absolutely rigid, then in the case of sliding contact between such a shell and the filler, the following conditions must be satisfied

$$\text{when } r = a_1 \quad u_r = 0, \quad \sigma_{rx} = 0 \tag{42}$$

and in the case of rigid contact, this condition is written as follows

$$\text{when } r = a_1 \quad u_x = 0, \quad u_r = 0 \tag{43}$$

and in the latter case, the elements in the determinant $det\left\| b_{ij} \right\|$ must be replaced as follows

$$b_{11} = -s_2, \quad b_{12} = -s_5, \quad b_{13} = -e_2 s_8, \quad b_{14} = e_2 s_{11},$$
$$b_{31} = es_1, \quad b_{32} = -es_4, \quad b_{33} = s_7, \quad b_{34} = s_{10}. \tag{44}$$

In all cases, to obtain the final results, it is necessary to calculate the improper Fourier integrals according to the formulas of the form (37), (38) and, since, as can be seen from the above calculations, the subintegral functions are very complex, these integrals cannot be calculated analytically, i.e., the answers cannot be obtained in the form of combinations of elementary and even special tabulated functions. In this regard, we have developed a special programme that takes into account the fact that, due to the presence of cosines, we are dealing with highly oscillating subintegral functions. Therefore, we applied a special method proposed by Filon for constructing quadrature formulas, which allowed us to obtain numerical results with any desired accuracy in an optimally short period of time on a personal computer.

As an example, calculations were performed for the following parameter values: $E/E' = 1.3$; $\nu = 0.3$; $\nu' = 0.2$; $\rho/\rho' = 1.5$; $h_1 = h_2$; $a_2/a_1 = 1.2$; $\chi = h_2/a_2 = 0.004$; $E_1 = E_2$; $\rho_1 = \rho_2$; $\gamma = E_1/E = 125$, $\rho^* = \rho_1/\rho = 12.5$. For comparison, the results for the corresponding isotropic filler are also given, where $E' = E$, $\nu' = \nu$, $\rho' = \rho$. Fig. 1 shows the change in deflections of the outer load-bearing shell ($w^* = G_2 w/p_0$) along the length at $c_{01} = 0.05$. Here, curves 1 correspond to the solution for rigid contact between the load-bearing layers and the transversely isotropic filler, curves 2 have no inner load-bearing layer, and curves 3 have a completely rigid inner layer. The dotted curves correspond to the isotropic filler.

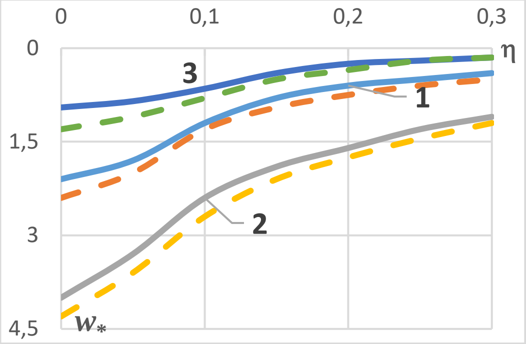

Figure 1. Distribution of shell deflections along the length

Figure 2 shows similar graphs for dimensionless ($\sigma^* = -a_2\sigma_{rr}/p_0$) contact stress on the contact surface of the outer layer and filler. Fig. 2 shows that with distance from the point of application of the concentrated ring load, the contact stresses change sign, which indicates the possibility of separation of the loaded shell from the filler in the case of sliding contact. In addition, Figures 1 and 2 show that changing the conditions on the inner surface of the filler significantly affects the deflections of the loaded bearing layer and has a much smaller effect on the contact stresses on the outer surface of the filler. The anisotropy of the filler material for the given parameter values does not change the qualitative picture, but it does change the quantitative characteristics of the stress-strain state of such a mechanical system composed of three elements.

Figure 3 shows the distribution of dimensionless radial displacements, and Figure 4 shows the distribution of dimensionless radial stresses across the thickness of the filler for different cross-sections η = *const* during the movement of the ring load. The meaning of indices 1–3 is the same as in Figures 1 and 2.

It can be seen that with distance from the point of application of the load, the distribution pattern changes significantly, especially for stresses.

DOI 10.15588/1607-3274-2026-1-7

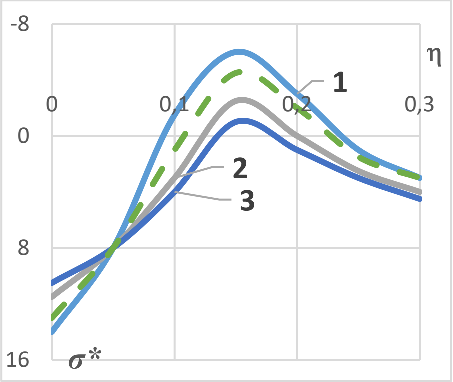

Figure 2. Contact stresses between the outer load-bearing layer and the aggregate

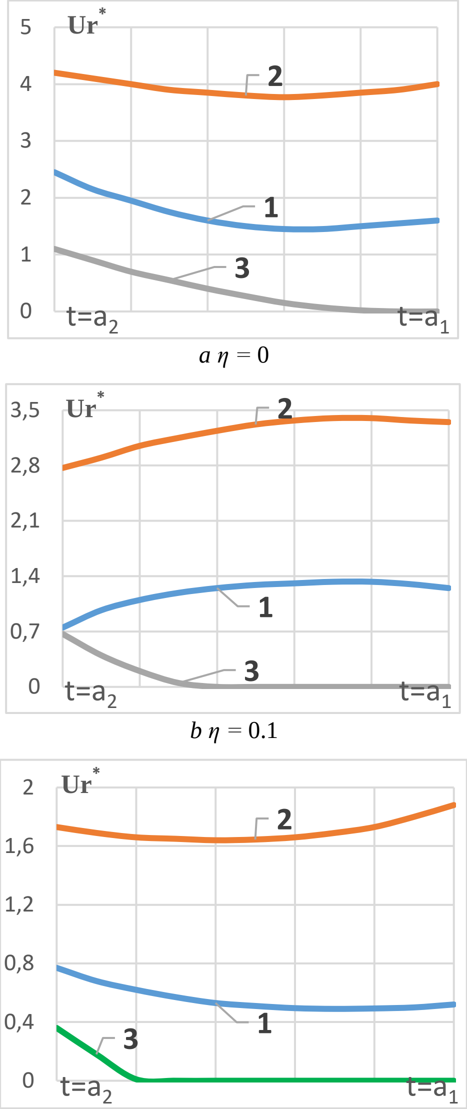

a $\eta = 0$

b $\eta = 0.1$

c) $\eta = 0.2$

Figure 3. Radial displacements in different cross-sections of the filler

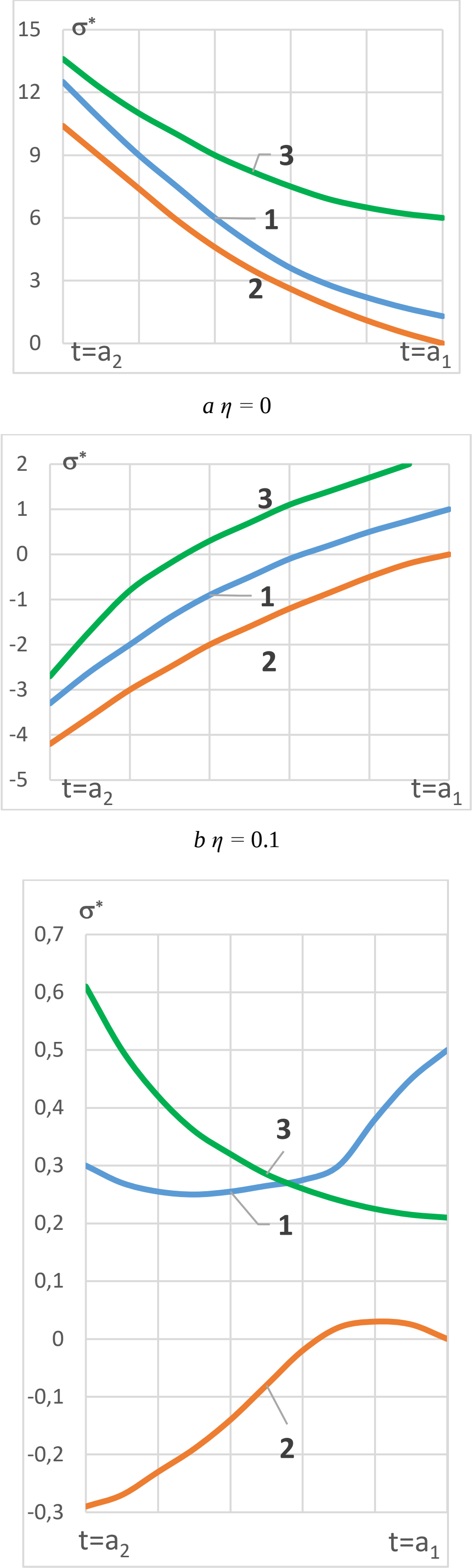

a $\eta = 0$

b $\eta = 0.1$

c $\eta = 0.2$

Figure 4. Change in normal stresses across the thickness of the filler filler

DOI 10.15588/1607-3274-2026-1-7

In conclusion, we note that the approach proposed in this work to extend the authors' approach describing the dynamics of three-layer shells to the case of a filler made of transversely isotropic material opens up possibilities for its use for other types of anisotropic materials. At the same time, the main difficulties on this path may arise when integrating dynamic equations for such media.

Conclusions

1. A semi-accurate mathematical model is proposed to describe the dynamics of a three-layer cylindrical shell with a transversely isotropic filler, where the motion of the supporting layers is described by the equations of motion of such shells, which are based on the approaches of Timoshenko or Kirchhoff-Lyau, and for the filler, the exact equations of the elasticity theory of an anisotropic body are used, with the contact conditions at the boundaries of each of the three layers being satisfied.
2. To solve the stationary dynamic problem of motion along the surface of an infinitely long three-layer cylindrical shell, an algorithm has been developed that consists of using Galilean transformation and applying, in a moving coordinate system that moves together with the load, complex integral Fourier transform. In this case, potential functions are introduced in a special way using previously unknown coefficients in the image space for integrating the equations of motion of a transversely isotropic material.
3. In general, the results after applying the inverse Fourier transform are obtained in the form of improper integrals with complex subintegral functions, therefore, for their approximate calculation with a given accuracy, a program has been developed based on the method proposed by Filon for constructing quadrature formulas for the case of strongly oscillating functions.
4. Various cases of boundary conditions on the inner surface of the filler are considered as special cases of the general results, in particular, the case of a shell with a liquid filler and a shell with a filler and a rigid core inside it.
5. For all the problems considered, numerical results were obtained using a computer and corresponding graphs were constructed, showing the influence of anisotropy and boundary conditions on the stress-strain state of a cylindrical shell composed of three layers.
6. The results of the work can be used for comparison when constructing approximate models of the dynamics of three-layer cylindrical shells with both isotropic and anisotropic filler material.

References

1. Pozhuyev, A. V., Pozhuev, V. I. (2015). Nestatsionarni protsesy v plastynakh i obolonkakh, yaki vzayemodiyutʹ z tryvymirnym pruzhnym seredovyshchem [Unsteady processes in plates and shells interacting with a three-dimensional elastic medium]. Kruhozir, 228.

2. Pozhuyev, A. V., Pozhuev, V. I. (2016). Vilʹni khvyli ta statsionarne deformuvannya elementiv konstruktsiy, yaki vzayemodiyutʹ z inertsiynym seredovyshchem [Free waves and stationary deformation of structural elements interacting with an inertial environment]. Kruhozir, 248.

3. Pozhuyev, A. V., Pozhuev, V. I., Fasolyak A.V. (2019). Matematychni modeli ta metody rozrakhunku nestatsionarnoyi dynamiky tsylindrychnykh obolonok u tryvymirnomu pruzhnomu seredovyshchi [Mathematical models and methods for calculating unsteady dynamics of cylindrical shells in a three-dimensional elastic medium]. Status, 152.

4. Gorshkov, A. G., Pozhuev, V. I. (1992). Statsionarnyye zadachi dinamiki mnogosloynykh konstruktsiy [Stationary problems of dynamics of multilayer structures]. Mashinostroyeniye, 224.

5. Pozhuev, V. I. (1980). Reaktsiya trekhsloynoy tsilindricheskoy obolochki na deystviye podvizhnoy zagruzki [Reaction of a three-layer cylindrical shell to the action of a moving load]. Prikladnaya mekhaníka, (16 (1)), 32–39.

6. Pozhuev, V. I. (1980). Reaktsiya tsilindricheskoy obolochki, nakhodyashcheysya v transversal'no izotropnoy srede, na deystviye podvizhnoy zagruzki [Reaction of a cylindrical shell located in a transversely isotropic medium to the action of a moving load]. Prikladnaya mekhaníka, (16 (11)), 28–35.

7. Pozhuyev, A. V., Pozhuyev, V. I., Fasolyak, A. V. (2016). Nestatsionarna deformatsiya tsylindrych-noyi obolonky u pruzhnomu pivprostori pid diyeyu poverkhnevykh navantazhenʹ [Non-stationary deformation of a cylindrical shell in a spring space under surface forces] Novi materialy i tekhnolohiyi v metalurhiyi ta mashynobuduvanni, (2), 201–213.

8. Pozhuyev, V. I., Fasolyak, A. V. (2017). Dynamika koaksialʹnykh tsylindrychnykh obolonok u pruzhnomu inertsiynomu seredovyshchi [Dynamics of coaxial cylindrical shells in an elastic inertial medium]. Tekhnichna mekhanika, (3), 90–98.

9. Pozhuyev, A., Pozhuyev, V., Mikhaylutsa, O. (2024). Diya zhorstkoho tila na vnutrishnyu poverkhnyu tovstostinnoho bimetalichnoho tsylindra. [The action of a rigid body on the inner surface of a thick-walled bimetallic cylinder] Novi materialy i tekhnolohiyi v metalurhiyi ta mashynobuduvanni, (2), 62–71.

10. Orlenko, S. P. (2024). Dynamika trysharovykh neodnoridnykh tsylindrychnykh obolonok na pruzhniy osnovi za nestatsionarnoho navantazhennya [Dynamics of three-layer inhomogeneous cylindrical shells on an elastic base under unsteady loading]. Dopovidi Natsionalʹnoyi akademiyi nauk Ukrayiny, (4), 14–23.

11. Teshaev, M., Safarov, I., Ibragimova, D., Rayimov, D., Akhmedov, S. (2024). Stationary response of the system “Cylindrical shell – viscoelastic filler” to the effect of a moving load, Journal of Physics: Conference Series, 2697, 641–658.

DOI 10.15588/1607-3274-2026-1-7

12. Foroutan, K., Dai, L. (2023). Nonlinear dynamic response and vibration of spiral stiffened FG toroidal shell segments with variable thickness. Mechanics of Advanced Materials and Structures, 30, 3184–3203.

13. Safarov, I., Teshaev, M., Marasulov, A., Jurayev, T., Raxmonov, B. (2021). Vibrations of cylindrical shell structures filled with layered viscoelastic material. E3S Web of Conferences, 264, 451–461.

14. Gaidaichuk, V., Kotenko, K., Mamedov A. (2023). Investigation of the dynamics of a three-layer shell structure of an elliptical cross-section under non-stationary dynamic loading, Strength of Materials and Theory of Structures, 111, P. 395–404.

15. Chen, Z., Wang, A., Qin, B., Wang, Q., Zhong, R. (2020). Investigation on free vibration and transient response of functionally graded graphene platelets reinforced cylindrical shell resting on elastic foundation. Eur. Phys. J. Plus. 135(7), 1–34.

Received 18.01.2026
Accepted 24.02.2026
Published 31.03.2026

ДІЯ РУХОМОГО НАВАНТАЖЕННЯ НА ТРЬОХШАРОВУ ЦИЛІНДРИЧНУ ОБОЛОНКУ З ТРАНСВЕРСАЛЬНО ІЗОТРОПНИМ ЗАПОВНЮВАЧЕМ

Андрій Пожуєв — канд. фіз.-мат. наук, професор, професор кафедри фундаментальної та прикладної математики Запорізького національного університету, м. Запоріжжя, Україна, *e-mail: scorpio6828@gmail.com,* ORCID: 0000-0002-4083-5139

Володимир Пожуєв — д-р фіз.-мат. наук, професор, професор кафедри теоретичної та прикладної механіки Національного університету «Запорізька політехніка», м. Запоріжжя, Україна, *e-mail: pozhuevvi@gmail.com,* ORCID: 0000-0002-9163-7888

Олена Міхайлуца — канд. техн. наук, доцент, доцент кафедри електроніки, інформаційних систем та програмного забезпечення Запорізького національного університету, м. Запоріжжя, Україна, *e-mail: elenamikhaylutsa7@gmail.com,* ORCID: 0000-0003-2935-7997

Мета роботи. *Розповсюдити раніше запропонований авторами підхід про застосування для задач динаміки трьохшарових циліндричних оболонок з ізотропним заповнювачем точних рівнянь теорії пружності на один із можливих випадків анізотропії матеріалу середнього шару, а саме ситуацію, коли заповнювач є трансверсально ізотропним. Отримати точні формули і на їх основі побудувати картину напружено-деформованого стану в такій складеній конструкції при русі вздовж зовнішньої поверхні зі сталою швидкістю нормального (радіального) навантаження.*

Методи дослідження. *Побудована математична модель динаміки трьохшарової циліндричної оболонки, коли рух несучих шарів описується рівняннями теорії тонких оболонок, а для трансверсально ізотропного заповнювача використовуються динамічні рівняння теорії пружності анізотропного середовища у загальному вигляді. При розгляді задачі у стаціонарній постановці застосовується перетворення Галілея, після чого в рухомій системі координат до усіх шуканих і заданих величин застосовується інтегральне перетворення Фур'є у комплексній формі. Для обчислення невласних інтегралів Фур'є розроблено квадратурні формули, які основані на методі Файлона для інтегрування швидко осцилюючих функцій, що дозволило ефективно отримувати чисельні результати із наперед заданою точністю.*

Отримані результати. *На основі побудованої моделі розглянута задача про рухоме навантаження, яке викликає стаціонарний напружено-деформований стан шаруватої циліндричної оболонки при різних умовах на поверхнях стику заповнювача і несучих шарів. При цьому контакт розглядається як жорсткий, так і ковзний, але виключається відставання оболонок від заповнювача. Складнощі, які виникають при розв'язанні рівнянь руху трансверсально ізотропного заповнювача здолані шляхом введення спеціальним способом з використанням невизначених коефіцієнтів потенціальних функцій. Для усіх можливих варіантів граничних умов результати отримані у вигляді неособливих невласних інтегралів, які обчислені за спеціальними квадратурними формулами. Показані картини розподілу переміщень і напружень як за довжиною так і за товщиною заповнювача, проведено порівняння з результатами для відповідного ізотропного заповнювача і проведено механічний аналіз результатів.*

Наукова новизна*. Вперше в такій постановці, коли поведінка заповнювача описується точними рівняннями динаміки пружного анізотропного тіла, отримано розв'язання стаціонарної динамічної задачі для трьохшарової циліндричної оболонки. Проведено порівняння з результатами раніше отриманими для випадку ізотропного заповнювача. Застосовано спеціальний прийом для введення потенціальних функцій для знаходження переміщень*

DOI 10.15588/1607-3274-2026-1-7

і напружень в динамічних рівняннях для трансверсально ізотропних матеріалів. Розглянуті важливі частинні граничні умови на границях контактів шарів.

Практична цінність. *Отримані при такому підході результати можуть бути використані в якості еталонних при побудові спрощених моделей динамічної поведінки трьохшарових циліндричних оболонок, зокрема таких, які враховують анізотропію заповнювача. До таких можна для прикладу віднести так звані ребристі звукоізолюючі матеріали.*

Ключові слова*: шарові оболонки, трансверсально ізотропне середовище, інтегральне перетворення, поте-нціальні функції, граничні умови, переміщення, напруження.*

Список літератури

1. Пожуєв А. В. Вільні хвилі та стаціонарне деформування елементів конструкцій, які взаємодіють з інерційним середовищем [Текст] / А. В. Пожуєв, В. І. Пожуєв. – Запоріжжя : Кругозір, 2016. – 248 с.

1. Пожуєв, А. В. Нестаціонарні процеси в пластинах і оболонках, які взаємодіють з тривимірним пружним середовищем [Текст] / А. В. Пожуєв, В. І. Пожуєв. – Запоріжжя : Кругозір, 2015. – 228 с.

3. Пожуєв А. В. Математичні моделі та методи розрахунку нестаціонарної динаміки циліндричних оболонок у тривимірному пружному середовищі [Текст] / А. В. Пожуєв, В. І. Пожуєв, А.В. Фасоляк. – Запоріжжя : Статус, 2019. – 152 с.

4. Горшков, А. Г. Стационарные задачи динамики многослойных конструкций [Текст] / А. Г. Горшков, В. И. Пожуев. – М. : Машиностроение, 1992. – 224 с.

5. Пожуев В. И. Реакция трехслойной цилиндрической оболочки на действие подвижной загрузки / Пожуев В. И. [Текст] // Прикладная механіка. – 1980. – Т. 16. – №1. – С. 32–39.

6. Пожуев В. И. Реакция цилиндрической оболочки, находящейся в трансверсально изотропной среде, на действие подвижной загрузки [Текст] / Пожуев В. И. // Прикладная механіка, 1980. – Т. 16. – № 11. – С. 28–35.

7. Пожуєв А. В. Нестаціонарна деформація циліндричної оболонки у пружному півпросторі під дією поверхневих навантажень /А. В. Пожуєв, В. І. Пожуєв, А. В. Фасоляк // Нові матеріали і технології в металургії та машинобудуванні. – 2016. – № 2. – С. 201–213.

8. Пожуєв В. І. Динаміка коаксіальних циліндричних оболонок у пружному інерційному середовищі / В. І. Пожуєв, А. В. Фасоляк // Технічна механіка. – 2017. – № 3. – С. 90–98.

9. Пожуєв А. Дія жорсткого тіла на внутрішню поверхню товстостінного біметалічного циліндра. [Текст] / А. Пожуєв, В. Пожуєв, О. Міхайлуца // Нові матеріали і технології в металургії та машинобудуванні. – 2024. – № 2. – С. 62–71.

10. Орленко С. П. Динаміка тришарових неоднорідних циліндричних оболонок на пружній основі за нестаціонарного навантаження [Текст] / Орленко С. П. // Доповіді Національної академії наук України, 2024, № 4. – С. 14–23.

11. Stationary response of the system “Cylindrical shell – viscoelastic filler” to the effect of a moving load [Text] / M. Teshaev, I. Safarov, D. Ibragimova et al. // Journal of Physics: Conference Series. – 2024. – 2697. – P. 641–658.

12. Foroutan K. Nonlinear dynamic response and vibration of spiral stiffened FG toroidal shell segments with variable thickness [Text] / K. Foroutan, L. Dai // Mechanics of Advanced Materials and Structures. – 2023. – 30. – P. 3184–3203.

13. Vibrations of cylindrical shell structures filled with layered viscoelastic material [Text] / I. Safarov, M. Teshaev, A. Marasulov et al. // E3S Web of Conferences. – 2021. – 264. – P. 451–461.

14. Gaidaichuk V. Investigation of the dynamics of a three-layer shell structure of an elliptical cross-section under non-stationary dynamic loading [Text] / V. Gaidaichuk, K. Kotenko, A. Mamedov // Strength of Materials and Theory of Structures. – 2023. – 111. – P. 395–404.

15. Investigation on free vibration and transient response of functionally graded graphene platelets reinforced cylindrical shell resting on elastic foundation. [Text] / Z. Chen, A. Wang, B. Qin et al. // Eur. Phys. J. Plus. – 2020. – 135(7). – P. 1–34.

DOI 10.15588/1607-3274-2026-1-7

p-ISSN 1607-6885 Нові матеріали і технології в металургії та машинобудуванні. 2026/1
e-ISSN 2786-7358 New materials and technologies in metallurgy and mechanical engineering. 2026/1

UDC 621.791.754:621.791.92:004.942

Ruslan Kulykovskyi — Candidate of Technical Sciences, Associate Professor, Vice-Rector for Scientific and Pedagogical Work and Issues of University Development Prospects, National University Zaporizhzhia Polytechnic, Zaporizhzhia, Ukraine, *e-mail: kulikovski@zp.edu.ua*, ORCID: 0000-0001-8781-2113

Kyrylo Krasnoselsky — Postgraduate student of the Department of Integrated Welding Technologies and Structural Modeling, National University Zaporizhzhia Polytechnic, Zaporizhzhia, Ukraine, *e-mail: kvkras@gmail.com*, ORCID: 0009-0006-5251-9076

MODELING OF THE INFLUENCE OF SHIELDING GAS COMPOSITION ON THE GEOMETRY OF THE DEPOSITED LAYER IN WIRE ARC ADDITIVE MANUFACTURING (WAAM)

Purpose. *To develop a generalized theoretical approach for describing the influence of shielding gas composition on the geometry of the deposited layer in the WAAM process, taking into account arc thermophysics, surface phenomena, and the thermohydrodynamics of the weld pool.*

Research methods. *Methods of analysis and generalization of scientific publications, the principles of heat transfer theory and fluid mechanics with a free surface, physical modeling of thermocapillary convection, as well as a semi-empirical mathematical description based on the introduction of integral gas-environment indices.*

Results. *A cause-and-effect framework describing the influence of shielding gas composition on effective heat input, melt surface activity, and the geometric parameters of the deposited layer was developed. A gas thermophysical index (GTI) was proposed to characterize the effect of the gas mixture on the thermal state of the arc, and a gas activity index (GAI) was introduced to reflect the influence of active components on the thermocapillary response of the molten pool. A structure of semi-empirical model was constructed, relating gas composition to bead width, layer height, and penetration depth.*

Sciettific novelty. *An integrated approach describing the influence of shielding gas on the formation of deposited-layer geometry in WAAM is proposed, in which the gas environment is considered as a physically meaningful process parameter. For the first time within the framework of this formulation, a system of integral indices, GTI and GAI, has been introduced for the formalized consideration of the thermophysical and chemical-surface channels through which gas mixture affects the process.*

Practical value. *The obtained results may serve as a theoretical basis for selecting shielding gas composition, predicting deposited-layer geometry, further calibration of the model using experimental data, and developing process control algorithms for WAAM.*

Key words: *Wire Arc Additive Manufacturing (WAAM), shielding gas, deposited layer, bead geometry, thermocapillary convection, weld pool, mathematical modeling, penetration depth.*

Introduction

Wire Arc Additive Manufacturing (WAAM) is considered one of the most promising directions in additive manufacturing of large-scale metallic components due to its high deposition productivity, efficient material utilization, and the possibility of employing conventional arc welding equipment integrated with robotic motion systems [1–4]. Particular interest in WAAM is driven by its suitability for producing complex-shaped parts in mechanical engineering, energy systems, transportation, and aerospace industries, where, in addition to productivity, geometric accuracy, stability of layer-by-layer deposition, and controllability of the thermal state of the process are of decisive importance [1–4].

One of the central scientific and technological challenges of WAAM is the formation of the deposited layer geometry. Bead width, layer height, and penetration depth directly influence the dimensional accuracy of the manufactured component, interlayer repeatability, accumulation of geometric deviations, surface waviness, and the extent of subsequent machining. In a multilayer process, even minor deviations in the geometry of an individual pass may lead to significant deterioration in the overall quality of the component. Therefore, the problem of predicting and controlling layer geometry parameters is among the key issues for the further development of WAAM as an industrial manufacturing technology [2–4].

Among the factors determining the geometry of the deposited layer, the composition of the shielding gas occupies a significant role. The gaseous environment affects not only the protection of molten metal from atmospheric contamination but also the thermal state of the arc, the mode

DOI 10.15588/1607-3274-2026-1-8

of electrode metal transfer, and wetting and flow conditions within the molten pool [5–9]. Variations in the ratio of inert and active components in the gas mixture may alter the spatial distribution of the heat flux, the surface condition of the molten metal, and the intensity of thermocapillary convection. Consequently, these changes influence bead shape, penetration depth, and the stability of layer formation [5–9]. This represents a fundamental feature of WAAM: the composition of the shielding gas acts not merely as a technological condition of the process but also as a factor governing the morphology of the deposited material.

At the same time, the current state of research is characterized by a certain inconsistency. On one hand, numerous experimental studies convincingly demonstrate that variations in shielding gas composition significantly influence bead geometry and the quality of multilayer deposition [5–7]. On the other hand, in most existing WAAM models, the shielding gas is either considered only indirectly through process parameters or treated as an auxiliary experimental condition without being introduced into the analytical description of the process as an independent physically meaningful variable [2–4, 10, 11]. As a result, a discrepancy arises between the experimentally confirmed significance of the gaseous environment and its insufficient integration into theoretical models describing layer geometry formation.

Another gap lies in the fact that many existing approaches consider separately the thermophysical influence of the gas on the arc and the surface phenomena occurring within the molten pool. In reality, however, these mechanisms act simultaneously in the WAAM process and determine the final layer morphology as the result of the coupled interaction of heat transfer, fluid flow, and surface forces [8–11]. For this reason, empirical selection of gas mixtures alone is insufficient for effective control of deposition geometry. Instead, a generalized approach is required that would relate the composition of the shielding gas to effective heat input, the thermocapillary response of the molten pool, and the principal geometric parameters of the deposited layer.

In this context, the present work is aimed at developing a generalized theoretical description of the influence of shielding gas composition on the geometry of the deposited layer in WAAM. Within this framework, the gaseous environment is considered as a physically meaningful process parameter associated with arc thermophysics, the surface activity of the molten metal, and the thermo-hydrodynamic state of the weld pool.

Analysis of research and publications

The initial stage of research development in the field of WAAM was associated with the formation of a general understanding of this technology as a high-productivity type of wire-based additive manufacturing for metallic components. Fundamental review studies demonstrated that WAAM possesses significant advantages for large-scale parts due to high deposition rates, efficient material utilization, and the possibility of integrating standard arc welding power sources with robotic motion systems. At the same time, these studies clearly outlined the main limitations of the process, including insufficient geometric accuracy, surface waviness, instability of bead shape, the influence of thermal history, and the need for additional quality assurance measures [1–5]. Thus, at the initial stage, scientific attention was mainly focused on the general technological capabilities of WAAM and on the challenge of achieving stable product quality.

Further development of the research area was associated with the transition from a general technological description to the analysis of individual factors determining the morphology of the deposited layer. In this context, particular importance was given to studies devoted to the influence of process parameters, heat input, motion trajectory, interlayer temperature, and cooling conditions on bead width, layer height, and penetration depth. At this stage, deposition geometry began to be considered not merely as a geometric outcome of the process but as an integral indicator of heat and mass transfer, solidification kinetics, and the stability of multilayer buildup [2–5, 12, 13]. However, even in these studies, the composition of the shielding gas generally remained either a background condition or a variable recorded experimentally without further inclusion in a physically meaningful analytical description.

A separate and more application-oriented stage of research consists of studies directly addressing the influence of shielding gas in WAAM. For stainless steels, a methodology has been proposed for selecting multicomponent Ar-based gas mixtures taking into account the regularity of metal transfer, geometric characteristics, and metallurgical features of deposited walls [6]. For wire arc additive processes based on Ar-CO_2 mixtures, experimental studies have shown that changes in gas composition affect the thermal regime, the local morphology of the deposit, and the quality of building different geometries [7]. In large-scale additive manufacturing of martensitic 410 steel, it was established that the type of gas mixture influences not only microstructure and mechanical properties but also process stability, which is directly related to deposition morphology [8]. For aluminum thin-walled WAAM structures, the importance of additional shielding has been demonstrated, affecting the regularity of metal transfer, surface cleanliness, and geometric quality [9]. The body of these works indicates that shielding gas in WAAM can no longer be regarded as a secondary factor. However, most of these studies are predominantly experimental and are focused on specific materials, mixtures, and operating regimes.

The physical foundations of such influence were established earlier in classical studies of arc welding. The work of Pires, Quintino, and Miranda demonstrated that the composition of gas mixtures significantly affects arc stability, metal transfer modes, and the process characteristics of Gas Metal Arc Welding (GMAW) [10]. In the study by

DOI 10.15588/1607-3274-2026-1-8

Lu, Fujii, and Nogi, it was shown that even small additions of O_2 or CO_2 to argon alter the oxygen content in the molten metal and may lead to a change in the character of Marangoni convection, thereby affecting weld pool shape and penetration depth [11]. A comprehensive analysis of the influence of various shielding gases on metal welding processes was presented in the work of Kah and Martikainen [14]. For WAAM applications, these studies are of fundamental importance, as they explain the mechanism of the gas environment not only through arc energetics but also through changes in the surface state of the molten metal and the restructuring of flow patterns within the weld pool. This marks the origin of the scientific direction linking gas composition with macroscopic layer geometry through the thermohydrodynamics of the molten pool.

The next important stage in the development of research is associated with numerical and analytical modeling of WAAM. In particular, Bai et al. developed a three-dimensional model of heat transfer and molten pool flow for multilayer PAW-based WAAM, demonstrating the decisive role of interlayer thermal history, melt pool hydrodynamics, and cooling conditions in the formation of the geometry of subsequent layers [12]. Oliveira, Santos, and Miranda summarized the fundamental welding concepts relevant to fusion-based additive manufacturing, including rapid thermal cycles, solidification, defect formation, and residual stress development [13]. However, even in advanced numerical approaches, the shielding gas is typically considered indirectly through the heat source model, process parameters, or experimentally specified conditions rather than being introduced into the model as an independent physically meaningful variable. Consequently, current models describe the thermal and hydrodynamic states of the process relatively well but still do not provide a generalized analytical relationship linking gas composition, arc conditions, surface phenomena, and layer geometry.

It is also important to highlight studies specifically evaluating the influence of shielding gas on the geometric quality of WAAM. The work of Gurčík, Kovanda, and Rohan directly focused on the effect of shielding gas on the geometrical quality of WAAM technology [15]. Together with the aforementioned WAAM studies, this confirms the relevance of the problem from the standpoint of layer geometry control rather than solely from the perspectives of metallurgy or mechanical properties. At the same time, comparison of these results shows that existing solutions are predominantly either purely experimental or technological-empirical in nature and do not provide a reduced physically interpretable model suitable for parametric prediction and further optimization of gas mixture composition.

Thus, a critical analysis of previous and contemporary publications allows several key stages to be identified:
- first, the establishment of WAAM as a high-productivity technology characterized by challenges related to geometric accuracy and stability [1–5];
- second, the accumulation of experimental data on the influence of specific gas mixtures on deposition morphology and material properties [6–9, 15];
- third, the development of fundamental concepts concerning the role of shielding gas through metal transfer modes, surface tension effects, and Marangoni convection [10, 11, 14];
- fourth, the development of thermohydrodynamic models of WAAM, in which the gas environment has not yet become a full-fledged parameter of a generalized description [12, 13]. This last circumstance defines the unresolved part of the overall problem.

The unresolved aspect of the problem is the absence of a generalized analytical approach in which the composition of the shielding gas would be incorporated into the process description as a parameter simultaneously characterizing its thermophysical influence on the thermal state of the arc and its chemical-surface influence on the thermocapillary response of the molten pool. This limitation prevents the transition from empirical selection of gas mixtures to physically grounded prediction of bead width, layer height, and penetration depth under WAAM conditions. Therefore, the role of the present work in addressing this problem lies in the development of a reduced theoretical approach in which the gaseous environment is parameterized through integral indices and linked to the geometry of the deposited layer through the thermohydrodynamic state of the molten pool. Such a research direction is both relevant and justified, as it combines a fundamental mechanical interpretation with the prospect of further experimental optimization and engineering application of the model.

Research objective

The objective of this study is to develop a generalized theoretical approach for describing the influence of shielding gas composition on the geometry of the deposited layer in the WAAM process. To achieve this objective, the following tasks were formulated: to establish a cause-and-effect framework describing the influence of the gaseous environment on the thermal state of the arc and the thermocapillary response of the molten pool; to introduce integral indices characterizing the thermophysical and chemical-surface properties of the gas mixture; and to construct the structure of a semi-empirical model for describing bead width, layer height, and penetration depth.

The criteria for evaluating the quality of the obtained results include the physical validity of the approach, the internal consistency of the model, and its suitability for further parametric identification. The limitations of the study are determined by its theoretical nature, the use of a reduced analytical description, and its focus on arc-based WAAM processes operating in shielding gas environments.

Materials and research methodology

The material of the study consists of scientific publications devoted to WAAM technology, the influence of

DOI 10.15588/1607-3274-2026-1-8

shielding gas composition on arc processes, thermocapillary phenomena in the weld pool, and thermohydrodynamic modeling of molten pools [1–15]. The analysis includes review studies on WAAM [1–5], investigations of the influence of shielding gas in WAAM [6–9, 15], works on classical welding processes addressing the effects of gas mixtures on arc behavior, metal transfer, and weld pool morphology [10, 11, 14], as well as studies on numerical modeling of heat transfer and molten metal flow [12, 13].

The research methodology is based on a sequential transition from the analysis of known physical mechanisms to the development of a reduced analytical model. At the first stage, literature data were systematized concerning the influence of shielding gas composition on bead geometry, arc stability, metal transfer, and flow behavior in the molten pool. At the second stage, these patterns were physically generalized with the identification of two principal channels through which the gaseous environment influences the process: the thermophysical channel and the chemical–surface channel. At the third stage, a cause-and-effect framework of the process was established, and integral indices were introduced to parameterize the identified mechanisms of influence. At the final stage, the structure of a semi-empirical model was constructed to describe bead width, layer height, and penetration depth.

The study employed the method of scientific literature analysis, physical modeling of the process based on the principles of continuum mechanics, and a semi-empirical mathematical description. The analytical method was used to identify stable and physically justified relationships describing the influence of He, CO_2, and O_2 on the thermal state of the arc, the surface activity of the molten metal, and the geometry of deposition [6–11, 14, 15]. Physical modeling was applied to determine the principal mechanisms governing the formation of layer geometry, which are reduced to variations in effective heat input, the thermocapillary response of the molten pool, and the mass balance of deposited metal [11–13]. The semi-empirical approach was used to formalize the relationship between gas mixture composition and the main geometric characteristics of the deposited layer.

To describe the influence of the gaseous environment, two integral indices were introduced. The gas thermophysical index (GTI) characterizes the generalized influence of the gas mixture on the thermal state of the arc, whereas the gas activity index (GAI) reflects its influence on the surface state of the molten metal and on the conditions governing thermocapillary convection. Within the proposed model, effective heat input is considered as a function of process parameters and GTI, while the thermocapillary response of the molten pool is described as a function of GAI. Bead width and penetration depth are represented as functions of the thermal state and flow behavior in the molten pool, whereas layer height is determined through the mass balance of deposited material and the geometry of the cross-section.

The reliability and validity of the obtained results are ensured by the physical interpretability of all model parameters, the consistency of the model with the conservation laws of mass, energy, and momentum, and its agreement with established trends reported in the literature for inert, helium-containing, and active gas mixtures [6–12, 14, 15]. The proposed approach has a theoretical character and is intended to describe the macrogeometry of the deposited layer at the level of integral characteristics. It does not replace full three-dimensional numerical modeling but provides a conceptual foundation for further calibration and application in predictive and optimization tasks for the WAAM process.

Research results

In this study, the results were obtained through the construction and analytical investigation of a semi-empirical model describing the formation of the geometry of a single deposited bead in WAAM. Within the proposed formulation, the composition of the shielding gas is taken into account through two integral parameters, namely the gas thermophysical index $\boldsymbol{GTI}$ and the gas activity index $\boldsymbol{GAI}$, which represent, respectively, the thermophysical and chemical–surface channels through which the gaseous environment influences the deposition process. This approach makes it possible to establish a functional relationship between the properties of the gas environment, the thermal state of the arc, the thermocapillary response of the molten pool, and the principal geometric characteristics of the formed layer.

In what follows, the geometry of the current bead is described by four principal cross-sectional parameters: bead width $\boldsymbol{w}$, layer height $\boldsymbol{h}$, penetration depth $\boldsymbol{p}$ and wetting angle $\boldsymbol{\theta}$. The width $\boldsymbol{w}$ is defined at the level of the surface of the previous layer, the height $\boldsymbol{h}$ - as the distance from this surface to the apex of the current bead, and the penetration depth $\boldsymbol{p}$ - as the distance from the same reference surface to the lowest point of the fusion zone. The wetting angle $\boldsymbol{\theta}$ characterizes the geometry of contact between the current layer and the previous one and reflects the spreading conditions of the liquid metal over the deposition surface. In the model, this parameter is of fundamental importance, since it is through $\boldsymbol{\theta}$ that the geometry of the bead cross-section is made consistent with the mass balance of the deposited metal.

The construction of the model is based on the assumption that the influence of shielding gas on deposition geometry is realized through variations in two governing components of the process. The first is associated with changes in the thermal state of the arc and the effective heat input to the deposition zone, while the second is associated with changes in the surface state of the molten pool and the character of thermocapillary flow. Accordingly, the model separately describes the energetic mechanism and the surface-hydrodynamic mechanism of bead geometry formation.

The basic energetic characteristic of the process is taken to be the linear heat input

DOI 10.15588/1607-3274-2026-1-8

$$Q_l = \eta_0 \frac{UI}{v_t}, \tag{1}$$

where Q_l is the linear heat input, J/m; η_0 is the thermal efficiency coefficient of the process; U is the arc voltage, V; I is the welding current, A; and v_t is the torch travel speed, m/s.

Taking into account the influence of the gaseous environment, the effective linear heat input is written as

$$Q_{eff} = Q_l\left[1 + c_g(GTI - 1)\right], \tag{2}$$

where Q_{eff} is the effective linear heat input, J/m; c_g is the sensitivity coefficient of heat input to changes in the thermophysical properties of the gas mixture.

The chemical-surface influence of the shielding gas is taken into account through the thermocapillary response function

$$\Psi_M = tanh[\chi(GAI - GAI_{cr}], \tag{3}$$

where Ψ_M is the dimensionless thermocapillary response function; GAI_{cr} is the critical value of the gas activity index; and χ is a parameter determining the steepness of the transition between flow regimes in the molten pool.

To account for the energy required for metal melting, a characteristic linear scale is introduced:

$$L_m = \sqrt{\frac{Q_{eff}}{\rho H_m}}, \tag{4}$$

where L_m is the characteristic melting scale, m; ρ is the metal density, kg/m^3; and H_m is the effective specific enthalpy of melting, J/kg.

Then the bead width is described by the relation

$$w = K_w L_m(1 - d_w \Psi_M), \tag{5}$$

and the penetration depth by

$$p = K_p L_m(1 + d_p \Psi_M), \tag{6}$$

where K_w, K_p, d_w, d_p are dimensionless model parameters. Equation (5) reflects that an increase in the melting scale broadens the bead, whereas an increase in Ψ_M, that is, a transition toward inward flow, limits its lateral spreading. Equation (6), in contrast, shows that the same transition promotes deeper penetration due to the concentration of heat and mass transfer in the axial zone.

The cross-sectional area of the bead is determined from the mass balance:

$$A_b = \frac{\dot{m}}{\rho v_t}, \tag{7}$$

where A_b – is the cross-sectional area, m^2; and $\dot{m}$ is the deposition mass rate, kg/s.

To establish the relationship between A_b, w, h and θ the bead cross-section is approximated by a symmetric circular segment. In this case, the cross-sectional area is

$$A_b = \frac{w^2}{4\,sin^2\theta}(\theta - sin\theta cos\theta), \tag{8}$$

where θ is expressed in radians, and the bead height is determined by

$$h = \frac{w}{2}\tan\frac{\theta}{2}, \tag{9}$$

Thus, the wetting angle θ enters the model as a geometric parameter through which the mass balance and the cross-sectional shape are closed. This makes it possible to determine the layer height not as an independent quantity, but as a consequence of the simultaneous action of mass input, bead width, and wetting conditions.

To evaluate morphological repeatability, the standard deviation of width was used:

$$\sigma_w = \sqrt{\frac{1}{N}\sum_{i=1}^{N}(w_i - \bar{w})^2}, \tag{10}$$

where w_i are the local width values, $\bar{w}$ is the mean width, and N is the number of considered cross-sections. Within the developed model, σ_w is used as an integral indicator of formation stability, sensitive to changes in the molten pool flow regime.

The resulting system of relations

$$\{x_i\} \to GTI,\, GAI \to Q_{eff},\, \Psi_M \to w,\, p \to \theta \to\ h \to \sigma_w \tag{11}$$

defines the complete structure of the model and provides a basis for the analytical investigation of the influence of shielding gas on the morphology of a single bead.

From Eq. (2), it directly follows that

$$\frac{\partial Q_{eff}}{\partial GTI} = Q_l\, c_g > 0. \tag{12}$$

Therefore, for positive c_g an increase in GTI leads to an increase in the effective linear heat input. Then, from Eq. (4),

$$\frac{\partial L_m}{\partial GTI} > 0, \tag{13}$$

and from Eq. (5),

$$\frac{\partial w}{\partial GTI} > 0. \tag{14}$$

This means that an increase in the gas thermophysical index, corresponding to a stronger thermophysical effect of the gas mixture on the arc, leads to bead widening.

From Eq. (6), it simultaneously follows that

$$\frac{\partial p}{\partial GTI} > 0, \tag{15}$$

DOI 10.15588/1607-3274-2026-1-8

that is, penetration depth also increases with increasing GTI. However, within the framework of the model, this effect is determined primarily by the increase in the melting scale L_m, rather than by a restructuring of surface flows.

For constant $\dot{m}$, ρ and v_t the cross-sectional area A_b remains constant according to Eq. (7). Therefore, an increase in w at constant A_b is possible from Eq. (8) only due to a decrease in the wetting angle:

$$\frac{\partial\theta}{\partial GTI} < 0. \quad (16)$$

Further, from Eq. (9),

$$\frac{\partial h}{\partial GTI} < 0. \quad (17)$$

Hence, an increase in GTI within the model leads to the formation of a wider, lower, and less convex bead with a smaller wetting angle.

For the thermocapillary response function, Eq. (3) yields

$$\frac{\partial \Psi_M}{\partial \mathrm{GAI}} = \chi\,\mathrm{sech}^2[\chi(GAI - GAI_{cr})] > 0. \quad (18)$$

This means that, with increasing GAI the system monotonically transitions from a regime of predominantly outward flow to a regime of inward flow.

From Eq. (5), one obtains

$$\frac{\partial \mathrm{w}}{\partial \mathrm{GAI}} < 0, \quad (19)$$

and from Eq. (6),

$$\frac{\partial \mathrm{p}}{\partial \mathrm{GAI}} > 0. \quad (20)$$

Thus, an increase in gas activity leads to a narrowing of the bead and an increase in penetration depth. This is a direct consequence of the fact that inward flow reduces lateral spreading of the metal and promotes axial concentration of the heat flux.

Since, at constant A_b bead narrowing must be compensated by an increase in the convexity of the cross-section, Eq. (8) implies

$$\frac{\partial \theta}{\partial \mathrm{GAI}} > 0. \quad (21)$$

Then, from Eq. (9),

$$\frac{\partial \mathrm{h}}{\partial \mathrm{GAI}} > 0. \quad (22)$$

Thus, within the framework of the model, an increase in GAI leads to the formation of a narrower, higher, and more convex bead with a larger wetting angle and greater penetration.

Expression (18) reaches its maximum under the condition

$$GAI = GAI_{cr}. \quad (23)$$

This means that precisely in the vicinity of $GAI = GAI_{cr}$ the geometric parameters of a single bead are most sensitive to variations in gas composition. Hence, the model predicts a nonlinear, threshold-type character of the influence of active gas components on layer morphology. Outside this region, the sensitivity decreases, since the $tanh$ function approaches saturation.

A combined analysis of Eqs. (5)–(9) shows that the geometry of a single bead is determined by the competition between two mechanisms. The first mechanism is associated with an increase in GTI, which raises the effective heat input, the melting scale, and the bead width. The second mechanism is associated with an increase in GAI, which, through Ψ_M alters the character of surface flows, narrows the bead, increases its convexity, and deepens penetration.

An important result follows from this: the same bead width may be obtained for different combinations of GTI and GAI, but with different values of$p$, θ and h. Therefore, the morphology of the deposited layer cannot be correctly described by the single parameter w alone; instead, it is necessary to consider the interrelated system

$$\{w,\ h,\ p,\ \theta\}. \quad (24)$$

The developed model further implies that the greatest instability in geometric formation should manifest itself in the vicinity of the critical region GAI_{cr}, where the sensitivity of width and wetting angle to gas composition is maximal. It is precisely in this region that local fluctuations in the thermocapillary response will exert the strongest influence on σ_w, i.e., on waviness and geometric repeatability from layer to layer.

Thus, the analytical investigation of the developed model has shown that

$$GTI \uparrow \Rightarrow Q_{eff} \uparrow, w \uparrow, p \uparrow, \theta \downarrow, h \downarrow \quad (25)$$

$$GAI \uparrow \Rightarrow \Psi_M \uparrow, w \downarrow, p \uparrow, \theta \uparrow, h \uparrow, \quad (26)$$

$GAI \approx GAI_{cr}$ $\Rightarrow$ maximum sensitivity w, h, p, θ to gas composition. (27)

Therefore, the principal result of the study is the development and analytical treatment of a dimensional model for the formation of the geometry of a single deposited bead in WAAM, in which bead width, layer height, penetration depth, and wetting angle are linked into a unified system through mass balance, effective heat input, and the thermocapillary response of the molten pool. The obtained relationships define the nature of the influence of shielding gas composition on bead morphology and provide a basis

DOI 10.15588/1607-3274-2026-1-8

for further experimental calibration of the model and physical interpretation of the results.

In the present study, the proposed model was formulated for Fe-based WAAM, primarily for steel systems, in which the influence of shielding gas composition on bead width, penetration depth, wetting angle, and layer height can be generalized within the framework of a thermophysical–surface formulation.

For the practical interpretation of the obtained dependencies, Table 1 presents the generalized character of the influence of typical shielding gas environments on the geometry of a single deposited bead in Fe-based WAAM. The table reflects the expected morphological trends within the framework of the developed model.

Discussion

The obtained results indicate that the influence of shielding gas composition on the geometry of the deposited layer in WAAM should be considered as the result of the combined action of two physically distinct mechanisms. The first mechanism is associated with changes in the thermal state of the arc and the effective linear heat input, while the second is related to variations in the surface state of the molten pool and the character of thermocapillary flow. Such a separation makes it possible to move beyond a purely technological interpretation of the gaseous environment and to consider it instead as a control factor that directly affects the morphology of an individual bead.

It should be emphasized that the applied interpretation of the model presented here primarily concerns Fe-based WAAM, for which the influence of shielding gas on the geometry of a single bead can be generalized through thermophysical and chemical–surface mechanisms.

From the standpoint of process physics, the obtained relationships for $\boldsymbol{Q_{eff}}$, $\boldsymbol{w}$ and $\boldsymbol{p}$ are consistent with the fact that the thermophysical properties of the gas mixture determine not only the overall level of supplied energy but also the character of its spatial distribution in the arc region. Within the framework of the model, an increase in the thermophysical index $\boldsymbol{GTI}$ leads to an increase in the effective linear heat input and, consequently, in the characteristic melting scale $\boldsymbol{L_m}$. This can be interpreted as an expansion of the thermal influence zone and an increase in bead width. Such a result is physically plausible for gas mixtures with higher thermophysical potential, particularly those containing helium, where the plasma column and heat flux become more distributed, resulting in a wider and less convex bead.

At the same time, the model shows that an increase in $\boldsymbol{GAI}$ affects not the energetic component of the process, but primarily its surface-hydrodynamic component. Through the function $\boldsymbol{\Psi_M}$ this reflects a transition from a regime of predominantly outward flow to a regime of inward redistribution of the molten metal. Within this formulation, an increase in $\boldsymbol{GAI}$ naturally leads to a decrease in bead width and an increase in penetration depth. The physical meaning of this result lies in the fact that active components of the gaseous environment, by altering the surface state of the melt, affect the sign and magnitude of the thermocapillary gradient and, consequently, the direction of surface flows in the molten pool. As a result, heat and liquid metal become concentrated in the axial zone, which promotes the formation of a narrower but more deeply penetrated bead.

In the developed model, the wetting angle $\boldsymbol{\theta}$ does not serve as a secondary or merely illustrative parameter. On the contrary, it is precisely through this parameter that the geometry of the bead cross-section is made consistent with the mass balance of the deposited metal. This means that a change in width $\boldsymbol{w}$ at constant mass input cannot be considered in isolation from a change in cross-sectional shape. If $\boldsymbol{GTI}$ increases and the bead widens, then, at constant $\boldsymbol{A_b}$ this must be accompanied by a decrease in $\boldsymbol{\theta}$, that is, by the formation of a flatter profile. If, by contrast, $\boldsymbol{GAI}$ increases and the bead narrows, this should lead to an increase in $\boldsymbol{\theta}$ and to more pronounced convexity. For this reason, inclusion of the wetting angle in the model is necessary for a mechanically consistent description of the layer height $\boldsymbol{h}$.

The obtained equation for $\boldsymbol{h}$ has important methodological significance. Unlike many empirical approaches in which layer height is specified by a separate regression relationship, in the present work it is determined through the cross-sectional area, bead width, and wetting angle. This makes the description physically consistent: layer height is not an independent variable but rather a consequence of the combined action of heat input, surface phenomena, and mass transfer. From this standpoint, the developed model better corresponds to the real nature of WAAM, where the geometry of a single layer cannot be adequately described by a single parameter without taking into account the shape of the cross-section. The presence of the parameter $\boldsymbol{GAI_{cr}}$ in the model means that the influence of active components of the gas mixture on bead geometry has a threshold character. The maximum sensitivity of geometry to gas composition is realized precisely in the vicinity of $\boldsymbol{GAI_{cr}}$, where the derivative $\boldsymbol{\partial\Psi_M/\partial GAI}$ reaches its maximum. In physical terms, this corresponds to the region in which a change in the surface state of the melt produces the most intensive restructuring of flow in the molten pool. For WAAM, this is particularly important because, in a multilayer process, even a moderate variation in the geometry of a single pass accumulates and affects the dimensional accuracy of subsequent layers.

The developed model also leads to another important implication: the same value of bead width may be achieved by different combinations of $\boldsymbol{GTI}$ and $\boldsymbol{GAI}$, but with different values of $\boldsymbol{p}$, $\boldsymbol{h}$ and $\boldsymbol{\theta}$. This means that focusing on only one morphological parameter, for example bead width, is insufficient for evaluating the quality of the gaseous environment. A gas mixture that provides an acceptable value of $\boldsymbol{w}$, does not necessarily ensure optimal penetration, wetting angle, or formation stability. That is why, in the present work, the morphology of a single bead is considered as a system of interrelated parameters $\{\boldsymbol{w}, \boldsymbol{h}, \boldsymbol{p}, \boldsymbol{\theta}\}$, rather than as a set of independent quantities.

DOI 10.15588/1607-3274-2026-1-8

Table 1 – Applied interpretation of the model for typical shielding gas environments in Fe-based WAAM

Typical shielding gas environment	Expected GTI level	Expected GAI level	Dominant mechanism within the model	Expected geometry of a single bead	Applied interpretation for Fe-based WAAM
Pure argon (Ar = 99.9–100%)	reference	very low	Baseline thermal state of the arc under minimal chemical–surface influence	w – medium; h – medium; p – moderate; θ – medium	Can be treated as the baseline inert atmosphere for comparison with He-containing and active-gas mixtures
Ar-He, He-enhanced inert environment (Ar + 10–25% He)	elevated	low	Strengthening of the thermophysical channel: increase in Q_{eff} and L_m	w ↑; h ↓; p ↑; θ ↓	A wider, lower, and less convex bead is expected. Such mixtures are suitable when enhanced spreading of molten metal and a flatter layer profile are required
Ar + low O_2 addition (Ar + 1–2% O_2)	close to reference or slightly increased	moderate	Strengthening of the chemical–surface channel and modification of the thermocapillary gradient	w ↓; h ↑; p ↑; θ ↑	Can be interpreted as a controlled means of narrowing the bead and increasing penetration without moving to a strongly active atmosphere.
Ar + low moderate CO_2 addition (Ar + 2–5% CO_2)	close to reference or slightly increased	moderate / moderately elevated	Chemical–surface influence of the active component with enhanced inward thermocapillary flow	w ↓; h ↑; p ↑; θ ↑	This is a practically important range for Fe-based WAAM: the bead becomes narrower, higher, and more deeply penetrated; in many cases, this range provides a useful compromise between geometry and stability
Ar + elevated CO_2 content (Ar + 8–12% CO_2)	moderate	high	Dominance of the chemical–surface mechanism and strong restructuring of molten-pool flow	w ↓↓; h ↑↑; p ↑↑; θ ↑↑	A narrow, more convex, and deeply penetrated bead is expected. This range is associated with higher morphological sensitivity to disturbances and reduced repeatability
Combined Ar-He–active gas environment (Ar + 10–20% He + 0.5–2% CO_2 or Ar + 10–20% He + 0.5–1% O_2)	elevated	moderate	Competition of two mechanisms: (GTI) tends to widen the bead, whereas (GAI) tends to narrow it and increase penetration	w – moderate/controllable; h – moderate; p ↑; θ – close to medium or moderately increased	This is the most flexible category for bead-shape control, since it allows sufficient heat input to be combined with a controlled surface-driven effect

The parameter $\boldsymbol{\sigma_w}$, which characterizes formation repeatability, is not directly included in the main system of analytical equations in this study; however, the model makes it possible to interpret its behavior. Since, in the vicinity of $\boldsymbol{GAI_{cr}}$ bead geometry is most sensitive to small changes in the gaseous environment, it is precisely in this region that increased nonuniformity of formation and a rise in $\boldsymbol{\sigma_w}$ can be expected. Thus, the model not only describes the average geometric parameters of a single bead, but also provides a physical explanation of why the stability of the multilayer process may deteriorate under conditions close to critical thermocapillary restructuring.

At the same time, the results should be interpreted with due regard for the limits of applicability of the proposed formulation. The model is reduced in nature and does not fully account for arc unsteadiness, the discrete nature of droplet transfer, the temperature dependence of all metal and gas properties, or the specific features of particular alloys, which may influence the critical value $\boldsymbol{GAI_{cr}}$. It also does not replace a full three-dimensional CFD description of the process. Nevertheless, precisely as an analytical generalized framework, it has a significant advantage: it makes it possible to consider shielding gas composition as a model parameter rather than merely as a background experimental condition.

Therefore, the modeling results show that the formation of the geometry of a single deposited bead in WAAM is governed by the competition between two mechanisms: the expansion of the melting scale under the influence of the thermophysical properties of the gas, and the restructuring of thermocapillary flow under the influence of its chemical activity. It is this competition that determines whether a wider and flatter bead is formed, or a narrower, higher, and more deeply penetrated layer. This

DOI 10.15588/1607-3274-2026-1-8

constitutes the principal physical significance of the developed model and underlies its suitability as a basis for further experimental calibration.

Conclusions

A semi-empirical model describing the formation of the geometry of a single deposited bead in WAAM has been developed, in which the composition of the shielding gas is incorporated through two integral parameters: the gas thermophysical index $\boldsymbol{GTI}$ and the gas activity index $\boldsymbol{GAI}$. The proposed approach makes it possible to relate the properties of the gaseous environment to the effective heat input, the thermocapillary response of the molten pool, and the geometry of the bead.

It has been shown that the geometry of a single bead should be considered as an interconnected system of parameters $\boldsymbol{w}$, $\boldsymbol{h}$, $\boldsymbol{p}$ and $\boldsymbol{\theta}$, where bead width $\boldsymbol{w}$, layer height $\boldsymbol{h}$, penetration depth $\boldsymbol{p}$ and wetting angle $\boldsymbol{\theta}$ are determined by the combined action of thermal, surface, and mass transfer processes. The inclusion of the wetting angle in the model ensures consistency between the cross-sectional geometry and the mass balance of the deposited metal.

Analysis of the model has demonstrated that an increase in $\boldsymbol{GTI}$ leads to an increase in effective linear heat input, bead widening, and a reduction in bead convexity, whereas an increase in $\boldsymbol{GAI}$ results in bead narrowing, greater penetration depth, increased layer height, and a larger wetting angle. It has been established that the highest sensitivity of the geometric parameters to shielding gas composition occurs in the vicinity of the critical value $\boldsymbol{GAI_{cr}}$.

The practical significance of the obtained results lies in providing a theoretical foundation for further calibration of the model, for the rational selection of shielding gas composition, and for the development of approaches to controlling the geometry of the deposited layer in WAAM. Further research should focus on experimental validation of the model and on the identification of its parameters for specific material–process–gas environment systems.

References

1. Ding, D., Pan, Z., Cuiuri, D., & Li, H. (2015). Wire-feed additive manufacturing of metal components: Technologies, developments and future interests. The International Journal of Advanced Manufacturing Technology, 81, 465–481. https://doi.org/10.1007/s00170-015-7077-3

2. Jafari, D., Vaneker, T. H. J., & Gibson, I. (2021). Wire and arc additive manufacturing: Opportunities and challenges to control the quality and accuracy of manufactured parts. Materials & Design, 202, 109471. https://doi.org/10.1016/j.matdes.2021.109471

3. Pattanayak, S., & Sahoo, S. K. (2021). Gas metal arc welding based additive manufacturing: A review. CIRP Journal of Manufacturing Science and Technology, 33, 398–442. https://doi.org/10.1016/j.cirpj.2021.04.010

4. Cunningham, C. R., Flynn, J. M., Shokrani, A., Dhokia, V., & Newman, S. T. (2018). Invited review article: Strategies and processes for high quality wire arc additive manufacturing. Additive Manufacturing, 22, 672–686. https://doi.org/10.1016/j.addma.2018.06.020

5. Pan, Z., Ding, D., Wu, B., Cuiuri, D., Li, H., & Norrish, J. (2018). Arc welding processes for additive manufacturing: A review. In Transactions on intelligent welding manufacturing (pp. 3–24). Springer. https://doi.org/10.1007/978-981-10-5355-9_1

6. Teixeira, F. R., Jorge, V. L., Scotti, F. M., Siewert, E., & Scotti, A. (2024). A methodology for shielding-gas selection in wire arc additive manufacturing with stainless steel. Materials, 17(13), 3328. https://doi.org/10.3390/ma17133328

7. Silwal, B., Nycz, A., Masuo, C. J., Noakes, M. W., Marsh, D., & Vaughan, D. (2020). An experimental investigation of the effectiveness of Ar-CO₂ shielding gas mixture for the wire arc additive process. The International Journal of Advanced Manufacturing Technology, 108, 1285–1296. https://doi.org/10.1007/s00170-020-05395-7

8. Roy, S., Silwal, B., Nycz, A., Noakes, M., Cakmak, E., Nandwana, P., & Yamamoto, Y. (2021). Investigating the effect of different shielding gas mixtures on microstructure and mechanical properties of 410 stainless steel fabricated via large scale additive manufacturing. Additive Manufacturing, 38, 101821. https://doi.org/10.1016/j.addma.2020.101821

9. Jorge, V. L., Teixeira, F. R., Scotti, A., Scotti, F. M., & Siewert, E. (2023). The significance of supplementary shielding in WAAM of aluminium thin walls. Journal of Manufacturing Processes, 106, 520–536. https://doi.org/10.1016/j.jmapro.2023.09.063

10. Pires, I., Quintino, L., & Miranda, R. M. (2007). Analysis of the influence of shielding gas mixtures on the gas metal arc welding metal transfer modes and fume formation rate. Materials & Design, 28(5), 1623–1631. https://doi.org/10.1016/j.matdes.2006.02.012

11. Lu, S., Fujii, H., & Nogi, K. (2004). Marangoni convection and weld shape variations in Ar-O₂ and Ar-CO₂ shielded GTA welding. Materials Science and Engineering: A, 380(1–2), 290–297. https://doi.org/10.1016/j.msea.2004.05.057

12. Bai, X., Colegrove, P., Ding, J., Zhou, X., Diao, C., Bridgeman, P., Hönnige, J., Zhang, H., & Williams, S. (2018). Numerical analysis of heat transfer and fluid flow in multilayer deposition of PAW-based wire and arc additive manufacturing. International Journal of Heat and Mass Transfer, 124, 504–516. https://doi.org/10.1016/j.ijheatmasstransfer.2018.03.085

13. Oliveira, J. P., Santos, T. G., & Miranda, R. M. (2020). Revisiting fundamental welding concepts to improve additive manufacturing: From theory to practice. Progress in Materials Science, 107, 100590. https://doi.org/10.1016/j.pmatsci.2019.100590

14. Kah, P., & Martikainen, J. (2013). Influence of shielding gases in the welding of metals. The International

DOI 10.15588/1607-3274-2026-1-8

Journal of Advanced Manufacturing Technology, 64, 1411–1421. https://doi.org/10.1007/s00170-012-4111-6

15. Gurčík, T., Kovanda, K., & Rohan, P. (2019). Influence of shielding gas on geometrical quality of WAAM technology. In METAL 2019: 28th International Conference on Metallurgy and Materials, Conference Proceedings, 715–721. https://doi.org/10.37904/metal.2019.871

Received 27.02.2026
Accepted 17.03.2026
Published 31.03.2026

МОДЕЛЮВАННЯ ВПЛИВУ СКЛАДУ ЗАХИСНОГО ГАЗУ НА ГЕОМЕТРІЮ НАПЛАВЛЕНОГО ШАРУ ПРИ ТЕХНОЛОГІЇ ДУГОВОГО АДИТИВНОГО ВИРОБНИЦТВА З ВИКОРИСТАННЯМ ДРОТУ (WAAM)

Руслан Куликовський	канд. техн. наук, доцент, проректор з науково-педагогічної роботи та питань перспектив розвитку університету Національного університету «Запорізька політехніка», м. Запоріжжя, Україна, *e-mail: kulikovski@zp.edu.ua*, ORCID: 0000-0001-8781-2113
Кирил Красносельський	аспірант кафедри інтегрованих технологій зварювання та моделювання конструкцій Національного університету «Запорізька політехніка», м. Запоріжжя, Україна, *e-mail: kvkras@gmail.com*, ORCID: 0009-0006-5251-9076

Мета роботи. *Розроблення узагальненого теоретичного підходу до опису впливу складу захисного газу на геометрію наплавленого шару при технології WAAM з урахуванням теплофізики дуги, поверхневих явищ та термогідродинаміки зварювальної ванни.*

Методи дослідження. *Використано методи аналізу й узагальнення наукових публікацій, положення теорії теплопереносу та механіки рідини з вільною поверхнею, фізичне моделювання термокапілярної конвекції, а також метод напівемпіричного математичного опису із введенням інтегральних індексів газового середовища.*

Отримані результати. *Сформовано причинно-наслідкову схему впливу складу захисного газу на ефективне тепловкладення, поверхневу активність розплаву та геометричні параметри наплавленого шару. Запропоновано термофізичний індекс газу GTI, що характеризує вплив газової суміші на тепловий стан дуги, та індекс газової активності GAI, який відображає вплив активних компонентів на термокапілярну відповідь ванни розплаву. Побудовано структуру напівемпіричної моделі, яка пов'язує склад газу з шириною валика, висотою шару та глибиною проплавлення.*

Наукова новизна. *Запропоновано інтегрований підхід до опису впливу захисного газу на формування геометрії наплавленого шару при WAAM, у якому газове середовище розглядається як фізично змістовний параметр процесу. Уперше в межах даної постановки введено систему інтегральних індексів GTI та GAI для формалізованого врахування хімічно-поверхневого та термофізичного каналів впливу газової суміші.*

Практична цінність. *Отримані результати можуть бути використані як теоретична основа для вибору складу захисного газу, прогнозування геометрії наплавленого шару, подальшої калібровки моделі за експериментальними даними та розроблення алгоритмів керування процесом WAAM.*

Ключові слова: *технологія дугового адитивного виробництва з використанням дроту* (*WAAM*)*, захисний газ, наплавлений шар, геометрія валика, термокапілярна конвекція, зварювальна ванна, математичне моделювання, проплавлення.*

Список літератури

1. Wire-feed additive manufacturing of metal components: technologies, developments and future interests / Ding D., Pan Z., Cuiuri D., Li H. // The International Journal of Advanced Manufacturing Technology. – 2015. – Vol. 81. – P. 465–481. DOI: https://doi.org/10.1016/j.cirpj.2021.04.010

2. Jafari D. Wire and arc additive manufacturing: Opportunities and challenges to control the quality and accuracy of manufactured parts / Jafari D., Vaneker T. H. J., Gibson I. // Materials & Design. – 2021. – Vol. 202. Article 109471. DOI: https://doi.org/10.1016/j.matdes.2021.109471

3. Pattanayak S. Gas metal arc welding based additive manufacturing: a review / Pattanayak S., Sahoo S. K. // CIRP Journal of Manufacturing Science and Technology. 2021. Vol. 33. P. 398–442. DOI: https://doi.org/10.1016/j.cirpj.2021.04.010

4. Invited Review Article: Strategies and Processes for High Quality Wire Arc Additive Manufacturing / Cunningham C. R., Flynn J. M., Shokrani A. et al. // Additive Manufacturing. – 2018. – Vol. 22. – P. 672–686. DOI: https://doi.org/10.1016/j.addma.2018.06.020

5. Pan Z., Ding D., Wu B., Cuiuri D., Li H., Norrish J. Arc Welding Processes for Additive Manufacturing: A Review // Transactions on Intelligent Welding Manufacturing. Springer. – 2018. – P. 3–24. DOI: https://doi.org/10.1007/978-981-10-5355-9_1

6. A Methodology for Shielding-Gas Selection in

DOI 10.15588/1607-3274-2026-1-8

Wire Arc Additive Manufacturing with Stainless Steel / Teixeira F. R., Jorge V. L., Scotti F. M. et al. // Materials. – 2024. – Vol. 17. – No. 13. Article 3328. DOI: https://doi.org/10.3390/ma17133328

7. An experimental investigation of the effectiveness of Ar-CO_2 shielding gas mixture for the wire arc additive process / Silwal B., Nycz A., Masuo C. J. et al. // The International Journal of Advanced Manufacturing Technology. – 2020. – Vol. 108. – P. 1285–1296. DOI: https://doi.org/10.1007/s00170-020-05395-7

8. Investigating the effect of different shielding gas mixtures on microstructure and mechanical properties of 410 stainless steel fabricated via large scale additive manufacturing / Roy S., Silwal B., Nycz A. et al. // Additive Manufacturing. – 2021. – Vol. 38. Article 101821. DOI: https://doi.org/10.1016/j.addma.2020.101821

9. The significance of supplementary shielding in WAAM of aluminium thin walls / Jorge V. L., Teixeira F. R., Scotti A. et al. // Journal of Manufacturing Processes. – 2023. – Vol. 106. – P. 520–536. DOI: https://doi.org/10.1016/j.jmapro.2023.09.063

10. Pires I. Analysis of the influence of shielding gas mixtures on the gas metal arc welding metal transfer modes and fume formation rate / Pires I., Quintino L., Miranda R. M. // Materials & Design. 2007. Vol. 28, No. 5. P. 1623–1631. DOI: https://doi.org/10.1016/j.matdes.2006.02.012

11. Lu S. Marangoni convection and weld shape variations in Ar-O^2 and Ar-CO_2 shielded GTA welding / Lu S., Fujii H., Nogi K. // Materials Science and Engineering: A. – 2004. – Vol. 380. – No. 1–2. – P. 290–297. DOI: https://doi.org/10.1016/j.msea.2004.05.057

12. Numerical analysis of heat transfer and fluid flow in multilayer deposition of PAW-based wire and arc additive manufacturing / Bai X., Colegrove P., Ding J. et al. // International Journal of Heat and Mass Transfer. – 2018. – Vol. 124. – P. 504–516. DOI: https://doi.org/10.1016/j.ijheatmasstransfer.2018.03.085

13. Oliveira J. P. Revisiting fundamental welding concepts to improve additive manufacturing: From theory to practice / Oliveira J. P., Santos T. G., Miranda R. M. // Progress in Materials Science. – 2020. – Vol. 107. Article 100590. DOI: https://doi.org/10.1016/j.pmatsci.2019.100590

14. Kah P. Influence of shielding gases in the welding of metals / Kah P., Martikainen J. // The International Journal of Advanced Manufacturing Technology. – 2013. – Vol. 64. – P. 1411–1421. DOI: https://doi.org/10.1007/s00170-012-4111-6

15. Gurčík T. Influence of shielding gas on geometrical quality of WAAM technology / Gurčík T., Kovanda K., Rohan P. // METAL 2019–28th International Conference on Metallurgy and Materials, Conference Proceedings. – 2019. – P. 715–721. DOI: https://doi.org/10.37904/metal.2019.871

DOI 10.15588/1607-3274-2026-1-8

p-ISSN 1607-6885 Нові матеріали і технології в металургії та машинобудуванні. 2026/1
e-ISSN 2786-7358 New materials and technologies in metallurgy and mechanical engineering. 2026/1

МЕХАНІЗАЦІЯ, АВТОМАТИЗАЦІЯ ТА РОБОТИЗАЦІЯ

MECHANIZATION, AUTOMATION AND ROBOTICS

UDC 621.979

Vasyl Obdul — Candidate of Technical Science, Associate Professor, Department of Metal Forming, National University Zaporizhzhia Polytechnic, Zaporizhzhia, Ukraine, *e-mail: obdul@zp.edu.ua*, ORCID: 0000-0001-6490-888

Oleksandr Yepishkin — Assistant, Department of Metal Forming, National University Zaporizhzhia Polytechnic, Zaporizhzhia, Ukraine, *e-mail: yepishkin@zp.edu.ua*, ORCID: 0000-0003-1447-9473

Anna Ben — Senior Lecturer, Department of Metal Forming, National University Zaporizhzhia Polytechnic, Zaporizhzhia, Ukraine, *e-mail: benanna1985@gmail.com*, ORCID: 0000-0002-9765-8030

Valentyn Zhdan — Senior Lecturer, Department of Metal Forming, National University Zaporizhzhia Polytechnic, Zaporizhzhia, Ukraine, *e-mail: zhdan.valentyn@gmail.com*, ORCID: 0000-0001-8781-3642

Viktoriia Shtankevych — Senior Lecturer, Department of Metal Cutting Machines and Tools, National University Zaporizhzhia Polytechnic, Zaporizhzhia, Ukraine, *e-mail: vitavs2007@gmail.com*, ORCID: 0000-0002-9958-4063

IMPROVED DESIGN OF THE SCREW PRESS COUPLING

Purpose. *The aim of the work is to increase the energy efficiency and operational reliability of heavy screw presses by creating a new drive design that ensures stabilization of the load on the power grid and eliminates thermal overloads of the electric motor.*

Research methods. *The study employs a critical analysis of modern technical solutions from leading manufacturers (Weingarten, Hasenclever), specifically the RZS series with direct drive. The research utilizes the general theory of electric drives to analyze energy efficiency in transient modes. Kinematic analysis and analytical calculations of the moment of inertia were performed to substantiate the method of separating the driving mass (kinetic energy accumulator) into multiple components to reduce inertial loads.*

Results. *The operational limitations of direct-drive presses, such as high peak currents and thermal overloads, were identified. A new screw press design was proposed featuring a kinetic energy accumulator consisting of a central driving flywheel and lateral driving masses mounted on the motor shafts. This accumulator is connected via a clutch to the working driven flywheel of the press. Separating the driving accumulator into segments allows for a 25-fold reduction in the mass of the driving elements while maintaining the same kinetic energy. To optimize the reverse stroke, the working flywheel itself is also divided into two parts: an inner flywheel (rigidly mounted on the spindle) and an outer flywheel (which is disengaged during the upward stroke of the slide). Recommendations for an autonomous reverse stroke system were provided.*

Scientific novelty. *A method for separating rotating masses into a continuously operating kinetic energy accumulator (driving flywheel system) and a cyclically connected working element is proposed. Unlike traditional rigid-connection drives, the new kinematic scheme utilizes an intermediate driving mass and a friction clutch, allowing the motor to operate continuously without frequent high-current starts.*

Practical value. *The design is applicable for presses with a nominal force from 2 MN and energy up to 5 MJ, suitable for precision forging of turbine blades and gears without stamping inclinations. The use of standard induction motors and the reduction of the drive's metal consumption decrease manufacturing and modernization costs while improving power grid stability.*

Key words: *engagement clutch, screw press, precision stamping, moment of inertia, slider, screw spindle, flywheel.*

Introduction

The modern stage of development of forging and stamping equipment is characterized by increased requirements for the precision of forgings and the energy efficiency of the equipment. In this segment, screw presses with direct electric drive have taken a leading position, becoming an effective alternative to hammers and crank

DOI 10.15588/1607-3274-2026-1-9

presses in the manufacturing of critical parts (turbine blades, gears, etc.).

Analysis of research and publications

Recognized leaders in the field, such as Weingarten and Hasenclever, utilize press designs (type RZS) where a single working flywheel is rigidly connected to the screw spindle and simultaneously serves as the rotor of an asynchronous motor [1]. While this scheme ensures precision, it forces the drive to operate in a mode of frequent starts and braking.

As illustrated in Fig. 1, this mode is characterized by peak starting currents exceeding 1000 A and significant thermal losses. According to the general theory of electric drives [2], theoretical efficiency in such modes is limited to approximately 50%. Attempts to solve this using frequency converters [3, 4] increase costs and reduce reliability due to shock loads, while hydraulic alternatives [5] suffer from lower operating speeds. Thus, developing a reliable mechanical drive that eliminates motor operation in transient modes remains a relevant problem.

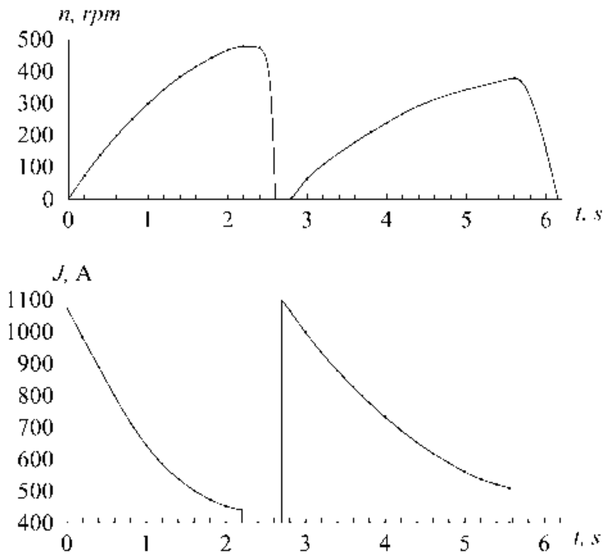

Figure 1. Typical diagram of startup modes of the arc-stator drive of RZS series presses (N = 250 kW, n_{synch} = 600 rpm)

Research material and methodology

A method of separating rotating masses into a continuously operating kinetic energy accumulator and a cyclically connected working element is proposed.

The essence of the proposed solution lies in the development of a press kinematic scheme with an alternative drive, in which the electric motor is kinematically decoupled from the screw during the working stroke. Instead of a rigid connection (as in the RZS scheme), an intermediate link is introduced – a kinetic energy accumulator (driving flywheel system), which is accelerated by the electric motor to the nominal speed and maintains rotation in a steady-state mode with high efficiency.

Energy transfer to the screw is carried out through a controlled friction clutch. Such a design allows the electric motor to operate without frequent starts and reversals, using the flywheel inertia to cover peak deformation loads.

Dissipating this heat from the stator windings poses a significant problem, despite the use of an electric fan, which complicates the operating conditions and maintenance of the press.

To mitigate these drawbacks, it is proposed to utilize kinetic energy previously accumulated by the driving flywheel system. In this case, the mechanism is implemented via an engagement clutch, where the working driven flywheel serves as the driven part, and the driving part acts as the central driving flywheel of the accumulator.

Research results

Fig. 2 presents an operation diagram illustrating the process of engagement and acceleration of the working flywheel to the nominal rotational speed. Up to point 2, a decrease in the angular velocity of the central flywheel and the acceleration of the working flywheel occur.

At point 2, full engagement of the central driving and working flywheels takes place; subsequent motion continues as the movement of a single mass up to point 3. At point 3, the clutch disengages, and the motion of the working flywheel continues by inertia.

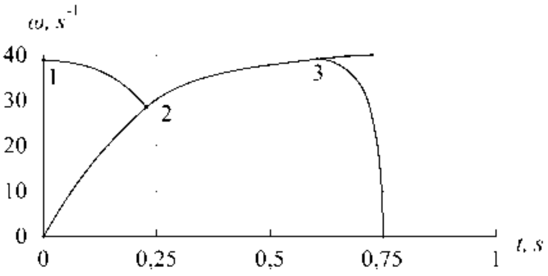

Figure 2. Changes in angular velocity of the central driving flywheel and the working driven flywheel during clutch engagement (qualitative representation)

Fig. 3 presents the kinematic scheme of the press. A slide 2, kinematically connected to the screw spindle 3, is installed in the press frame 1. The working flywheel 4 is mounted at the end of the spindle, above which the central flywheel (the main component of the accumulator) 5 is installed. Lateral driving masses 6 and 7 are positioned diametrically and mounted, for example, on the shafts of drive motors 8 and 9. The return movement of the slide is performed by the return drive 10.

As is known [6–7], the moment of inertia of the driving flywheel system is determined by the ratio (formula placeholder), and its practical value lies within the range of 2.5 ÷ 10. This allows for easy calculation of the moment of inertia of the accumulator.

In order to reduce the mass of the driving flywheel system, it can be divided into several components. Specifically, one part serves directly as the central flywheel (the driving member of the engagement clutch), while the other parts are made as separate discs with a gear rim, through

DOI 10.15588/1607-3274-2026-1-9

which they are kinematically connected to the central flywheel, which also features gear teeth [8-9]. These lateral masses can be directly mounted on the shafts of drive motors with a synchronous rotational speed of, for example, 1500 rpm or 3000 rpm.

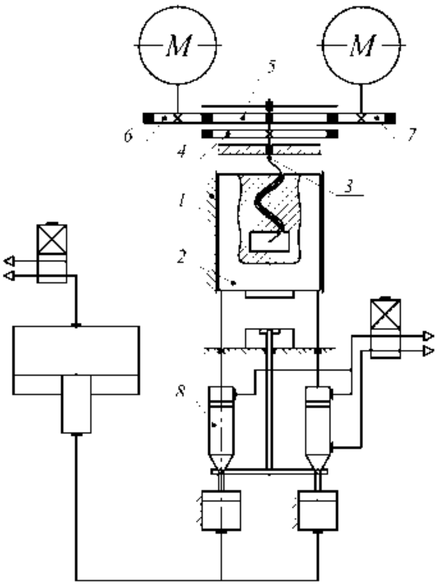

Figure 3. Kinematic scheme of the screw press:
1 – frame; 2 – slide; 3 – screw spindle;
4 – working driven flywheel; 5 – central driving flywheel;
6, 7 – lateral driving masses; 8 – slide return drive

This allows reducing the moment of inertia of these lateral masses by a factor of i^2; for instance, with a clutch engagement speed of 300 rpm ($i = 5$) and a motor speed n_{mot} = 1500 rpm, $i^2 = 25$. That is, the elements of the accumulator can have a weight 25 times lower while maintaining the same kinetic energy. Standard serial induction motors are used as drive motors, the maintenance of which presents no difficulties [10–11].

The return stroke drive can be pneumatic, hydraulic, or pneumohydraulic [11–12]. In order to reduce the level of kinetic energy accumulated in the working flywheel during the return stroke, which must be dissipated, it is proposed to divide the working flywheel into two parts [13–15].

The inner flywheel part is rigidly mounted on the screw spindle (Fig. 4), while the outer flywheel is able to rotate freely. The kinematic connection of both parts during the downward stroke is ensured by rotary keys. During the return stroke, the outer flywheel is braked; simultaneously, the keys rotate, the parts of the working flywheel lose kinematic contact, and during the slide ascent, only the screw spindle and the inner flywheel rotate.

The number of lateral masses can be two, four, or six, which allows reducing the moment of inertia and, consequently, the weight of the upper part of the press, which, in turn, positively affects the stability of the press.

Thus, this will allow, with reduced metal consumption of the screw press drive, to maintain its basic energy and power parameters, which ultimately makes it possible to reduce the cost of manufacturing new equipment and modernize existing equipment.

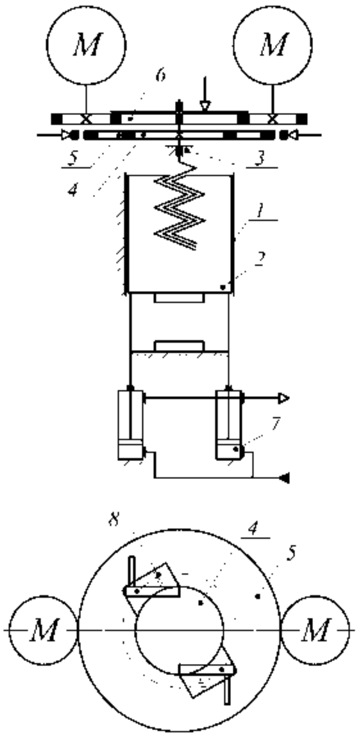

Figure 4. Kinematic scheme of the screw press:
1 – frame; 2 – slide; 3 – screw spindle; 4 – inner flywheel;
5 – outer flywheel; 6 – central driving flywheel;
7 – return drive; 8 – springs

Conclusions

An analysis of the operation of an electric screw press was carried out and a defect was identified, caused by the transient mode of operation of the drive, which is undesirable for the optimal operation of the device.

A screw press is proposed in which the reverse drive is autonomous, and the working stroke is performed by means of a drive with a clutch, in which the working flywheel is the driven part, and the driving part is the accumulator necessary for accelerating the working flywheel.

The proposed kinematic scheme with separation of flywheel masses allows significantly reduce the metal content of the drive and reduce inertial loads on the system during transient processes. The elements of the accumulator, specifically the lateral masses, can be 25 times lighter while maintaining the same kinetic energy. This increases the overall efficiency of the press by minimizing energy losses during acceleration and deceleration of massive parts (such as the outer flywheel) during the reverse stroke, and also ensures high maintainability of the equipment through the use of standard industrial components.

DOI 10.15588/1607-3274-2026-1-9

References

1. SMS Hasenclever Maschinenfabrik GmbH. (1986). U.S. Patent No. 4,563,889. U.S. Patent and Trademark Office. https://patents.justia.com/patent/4563889

2. Popovych, M. H., Lozynskyi, O. Yu., & Klepikov, V. B. (2005). Elektromekhanichni systemy avtomatychnoho keruvannia ta elektropryvody [Electromechanical systems of automatic control and electric drives]. Lybid.

3. Fang, X., Chen, J., Zhang, W., & Li, W. (2022). Research on servo and drive system of hot stamping mechanical servo press. Advances in Engineering Research, 230, 452–456. https://doi.org/10.2991/978-94-6463-114-2_58

4. Hojda, S., & Groche, P. (2023). A simulation study on the closed-loop control of screw press forgings using the impact energy as control input. Production Engineering, 17(1), 123–134. https://doi.org/10.7494/cmms.2018.3.0618

5. Altan, T., Ngaile, G., & Shen, G. (2005). Cold and hot forging: Fundamentals and applications. ASM International.

6. Song, H., Durand, C., Baudouin, C., & Bigot, R. (2024). Dynamic modelling and efficiency prediction for forging operations under a screw press. The International Journal of Advanced Manufacturing Technology, 134, 645–656. https://doi.org/10.1007/s00170-024-14114-5

7. Dziubinska, A. (2023). Connectors from zk60 magnesium alloy preforms. Materials, 16(9), 3467. https://doi.org/10.3390/ma16093467

8. Malashchenko, V. O., & Strilets, V. M. (2019). Detali mashyn [Machine elements]. Novyi Svit-2000.

9. Zahirniak, M. V., & Nevzlin, B. I. (2009). Elektrychni mashyny [Electric machines] (2nd ed.). Znannia.

10. Gontarz, A., Drozdowski, K., Dziubinska, A., Winiarski, G., & Surdacki, P. (2020). Forging of Mg-Al-Zn magnesium alloys on screw press and forging hammer. Materials, 14(1), 32. https://doi.org/10.3390/ma14010032

11. Obdul, V., Matiukhin, A., Shyrokobokov, V., & Matiukhina, T. (2022). Hvyntovyi pres [Screw press] (Patent No. 127676). Ukrainian Intellectual Property Institute.

12. Obdul, V., Matiukhin, A., Kovalek, A., Riabenko, A., Yepishkin, O., & Fedosieieva, V. (2024). Enerhoefektyvni konstruktsii hvyntovykh presiv [Energy-efficient designs of screw presses]. Novi materialy i tekhnolohii v metalurhii ta mashynobuduvanni, (4), 67–71. https://doi.org/10.15588/1607-6885-2024-4-7

13. Obdul, V. D., Matiukhin, A. Yu., Shyrokobokov, V. V., Ben, A. M., Lenok, A. A., & Yepishkin, O. V. (2024). Sposoby rehuliuvannia enerhii udariv na hvyntovykh presakh [Methods of regulating impact energy on screw presses]. Obrobka materialiv tyskom, 1(53), 152–158. https://doi.org/10.37142/2076-2151/2024-1(53)100

14. Mirandola, I., Berti, G. A., Caracciolo, R., Lee, S., Kim, N., & Quagliato, L. (2021). Machine learning-based models for the estimation of the energy consumption in metal forming processes. Metals, 11(5), 833. https://doi.org/10.3390/met11050833

15. Gao, M., He, K., Li, L., Wang, Q., & Liu, C. (2019). A review on energy consumption, energy efficiency and energy saving of metal forming processes from different hierarchies. Processes, 7(6), 357. https://doi.org/10.3390/pr7060357

Received 15.01.2026
Accepted 10.02.2026
Published 31.03.2026

УДОСКОНАЛЕНА КОНСТРУКЦІЯ МУФТИ ГВИНТОВОГО ПРЕСУ

Василь Обдул — канд. техн. наук, доцент кафедри обробки металів тиском Національного університету «Запорізька політехніка», м. Запоріжжя, Україна, *e-mail: obdul@zp.edu.ua*, ORCID: 0000-0001-6490-888

Олександр Єпішкін — асистент кафедри обробки металів тиском Національного університету «Запорізька політехніка», м. Запоріжжя, Україна, *e-mail: yepishkin@zp.edu.ua*, ORCID:0000-0003-1447-9473

Анна Бень — ст. викладач кафедри обробки металів тиском Національного університету «Запорізька політехніка», м. Запоріжжя, Україна, *e-mail: benanna1985@gmail.com*, ORCID: 0000-0002-9765-8030

Валентин Ждан — ст. викладач кафедри обробки металів тиском Національного університету «Запорізька політехніка», м. Запоріжжя, Україна, *e-mail: zhdan.valentyn@gmail.com*, ORCID: 0000-0001-8781-3642

Вікторія Штанкевич — ст. викладач кафедри металорізальних верстатів та інструментів Національного університету «Запорізька політехніка», м. Запоріжжя, Україна, *e-mail: vitavs2007@gmail.com*, ORCID: 0000-0002-9958-4063

DOI 10.15588/1607-3274-2026-1-9

Мета роботи. *Підвищення енергоефективності та експлуатаційної надійності важких гвинтових пресів шляхом створення нової конструкції приводу, яка забезпечує стабілізацію навантаження на електромережу та усуває теплові перевантаження електродвигуна.*

Методи дослідження. *Критичний аналіз сучасних технічних рішень від провідних виробників (Weingarten, Hasenclever), зокрема серії RZS із прямим приводом. Для аналізу енергоефективності в перехідних режимах використано загальну теорію електроприводів. Було проведено кінематичний аналіз та аналітичні розрахунки моменту інерції для обґрунтування методу розділення приводної маси (накопичувача енергії) на декілька компонентів з метою зниження інерційних навантажень.*

Отримані результати. *Визначено експлуатаційні обмеження пресів із прямим приводом, такі як високі пікові струми та теплові перевантаження. Запропоновано нову конструкцію гвинтового преса, яка оснащена накопичувачем кінетичної енергії що складається з центрального ведучого маховика ті бічних приводних мас на валах двигуна. Цей накопичувач з'єднується через муфту з робочим (веденим) маховиком преса. Розділення приводного накопичувача на сегменти дозволяє зменшити масу приводних елементів у 25 разів при збереженні тієї ж кінетичної енергії. Для оптимізації зворотного ходу сам робочий маховик також розділено на дві частини: внутрішній маховик (жорстко закріплений на шпинделі) та зовнішній маховик (що відключається під час підйому повзуна). Надано рекомендації щодо автономної системи зворотного ходу.*

Наукова новизна. *Запропоновано метод розділення приводної маси на накопичувач енергії, що працює безперервно, та робочий елемент, що підключається циклічно. На відміну від традиційних приводів із жорстким зв'язком, нова кінематична схема використовує проміжну масу маховика та фрикційну муфту, що дозволяє двигуну працювати безперервно без частих пусків із високими струмами.*

Практична цінність. *Конструкція придатна для пресів з номінальним зусиллям від 2 МН і енергією до 5 МДж, які підходять для точного кування турбінних лопаток і шестерень без штампувальних ухилів. Використання стандартних асинхронних двигунів і зниження металоємності приводу зменшують витрати на виготовлення та модернізацію, водночас покращуючи стабільність електромережі.*

Ключові слова: *муфта зчеплення, гвинтовий прес, точне штампування, момент інерції, повзун, гвинтовий шпиндель, маховик.*

Список літератури

1. Screw Press : U.S. Patent 4,563,889 / SMS Hasenclever Maschinenfabrik GmbH. – Publ. 1986. – Available at: https://patents.justia.com/patent/4563889

2. Попович М. Г. Електромеханічні системи автоматичного керування та електроприводи / Попович М. Г., Лозинський О. Ю., Клепіков В. Б. – К. : Либідь, 2005.

3. Research on Servo and Drive System of Hot Stamping Mechanical Servo Press / Fang X., Chen J., Zhang W., Li W. // Advances in Engineering Research. – Paris : Atlantis Press, 2022. – Vol. 230. – P. 452–456. DOI: https://doi.org/10.2991/978-94-6463-114-2_58

4. Hojda S. Simulation study on the closed-loop control of screw press forgings using the impact energy as control input / Hojda S., Groche P. A. // Production Engineering. – 2023. – Vol. 17, No. 1. – P. 123–134. DOI: https://doi.org/10.7494/cmms.2018.3.0618

5. Altan T. Cold and Hot Forging: Fundamentals and Applications / Altan T., Ngaile G., Shen G. – Materials Park : ASM International, 2005.

6. Dynamic modelling and efficiency prediction for forging operations under a screw press / Song H., Durand C., Baudouin C., Bigot R. // The International Journal of Advanced Manufacturing Technology. – 2024. – Vol. 134. – P. 645–656. DOI: https://doi.org/10.1007/s00170-024-14114-5

7. Dziubinska A. Connectors from zk60 magnesium alloy preforms / Dziubinska A. // Materials. – 2023. – Vol. 16, No. 9. – 3467 p. DOI: https://doi.org/10.3390/ma16093467

8. Малащенко В. О. Деталі машин / Малащенко В. О., Стрілець В. М. – Львів : Новий Світ-2000, 2019.

9. Загірняк М. В., Невзлін Б. І. Електричні машини. – 2-ге вид. – К. : Знання, 2009.

10. Forging of Mg-Al-Zn magnesium alloys on screw press and forging hammer / Gontarz A., Drozdowski K., Dziubinska A. et al. // Materials. – 2020. – Vol. 14. – No. 1. – 32 p. DOI: https://doi.org/10.3390/ma14010032

11. Гвинтовий прес / Обдул В., Матюхін А., Широкобоков В., Матюхіна Т. : Патент 127676 Україна. – Опубл. 2022.

12. Енергоефективні конструкції гвинтових пресів / Обдул В., Матюхін А., Ковалек А. та ін. // Нові матеріали і технології в металургії та машинобудуванні. – 2024. – № 4. – С. 67–71. DOI: https://doi.org/10.15588/1607-6885-2024-7-7

13. Способи регулювання енергії ударів на гвинтових пресах / Обдул В. Д., Матюхін А. Ю., Широкобоков В. В. та ін. // Обробка матеріалів тиском. – 2024. – № 1 (53). – С. 152–158. DOI: https://doi.org/10.37142/2076-2151/2024-1(53)152

14. Machine Learning-Based Models for the Estimation of the Energy Consumption in Metal Forming Processes / Mirandola I., Berti G. A., Caracciolo R. et al. // Metals. – 2021. – Vol. 11, No. 5. – P. 833. DOI: https://doi.org/10.3390/met11050833

15. A Review on Energy Consumption, Energy Efficiency and Energy Saving of Metal Forming Processes from Different Hierarchies / Gao M., He K., Li L. et al. // Processes. – 2019. – Vol. 7, No. 6. – 357 p. DOI: https://doi.org/10.3390/pr7060357

DOI 10.15588/1607-3274-2026-1-9

Наукове видання

Нові матеріали і технології в металургії та машинобудуванні № 1/2026

Науковий журнал

Головний редактор:	д-р техн. наук, професор Сергій Бєліков
Заступники гол. редактора:	д-р техн. наук, професор Валерій Наумик
	канд. техн. наук, доцент Антон Матюхін

Оригінал-макет підготовлено у редакційно-видавничому відділі НУ «Запорізька політехніка»

Комп’ютерний дизайн та верстання: Наталія Савчук

Реєстрація суб’єкта у сфері друкованих медіа:
Рішення Національної ради України з питань телебачення і радіомовлення
№ 3040 від 07.11.2024 року
Ідентифікатор медіа: R30-05583

Підписано до друку 19.03.2026. Формат 60×84/8
Папір офс. ризогр. Ум. др. арк. 10
Тираж 300 прим. Зам. № 153

69063, м. Запоріжжя, НУ «Запорізька політехніка», друкарня, вул. Жуковського, 64

Свідоцтво суб’єкта видавничої справи
ДК № 6952 від 22.10.2019